GIANT RESONANCE STUDY BY ^{6}Li SCATTERING

A Dissertation

by

XINFENG CHEN

Submitted to the Office of Graduate Studies of
Texas A&M University
in partial fulfillment of the requirements for the degree of

DOCTOR OF PHILOSOPHY

May 2008

Major Subject: Physics

GIANT RESONANCE STUDY BY ^{6}Li SCATTERING

A Dissertation

by

XINFENG CHEN

Submitted to the Office of Graduate Studies of
Texas A&M University
in partial fulfillment of the requirements for the degree of

DOCTOR OF PHILOSOPHY

Approved by:

Chair of Committee,	Dave H. Youngblood
Committee Members,	Robert E. Tribble
	Joseph B. Natowitz
	Shalom Shlomo
Head of Department,	Edward S. Fry

May 2008

Major Subject: Physics

ABSTRACT

Giant Resonance Study by ^{6}Li Scattering.

(May 2008)

Xinfeng Chen, B.S., Tianjin University; M.S., Institute of Modern Physics, Chinese Academy of Science

Chair of Advisory Committee: Dr. Dave H. Youngblood

Nuclear incompressibility K_{nm} is an important parameter in the nuclear matter equation of state (EOS). The locations of the isocalar giant monopole resonance (ISGMR) and giant dipole resonance (ISGDR) of nuclei are directly related to K_{nm} and thus can give the most effective constraint on the value of the K_{nm}. In order to determine K_{nm} accurately, a systematic study of the ISGMR and ISGDR over a wide range of nuclei is necessary. Alpha inelastic scattering at small angles has been successfully used to study the ISGMR of heavy and medium nuclei where the monopole resonance is concentrated in a broad peak. For light nuclei (A<40), however, ISGMR strengths are more elusive because the resonance is fragmented and extends to excitation energies above 35 MeV. Other processes give a large physical background at high excitation energy in α inelastic scattering, which makes it difficult to extract strength distributions in this range. As an isoscalar projectile (N=Z), ^{6}Li scattering could be an alternate way to study giant resonances. A better ratio between the resonance peak and the continuum is expected in ^{6}Li scattering due to the low particle emitting threshold. Another important motivation for ^{6}Li scattering study is to explore the possibility of expanding current research from stable nuclei to radioactive nuclei with inverse reactions using ^{6}Li as a target.

Data for elastic scattering of 240 MeV ^{6}Li ions and inelastic scattering to low-lying states and giant resonances was taken for ^{24}Mg, ^{28}Si and ^{116}Sn. A data analysis procedure was developed for double folding calculations. The optical potential parameters for ^{6}Li +

^{24}Mg, ^{6}Li + ^{28}Si and ^{6}Li + ^{116}Sn scattering systems were obtained by fitting elastic scattering data. Multipole analyses were carried out for inelastic scattering to high lying isoscalar giant resonances with multipolarities L=0 - 3. The results for the ISGMR and ISGQR are in agreement with those obtained with 240 MeV α scattering, however the agreement for the ISGDR and HEOR is not so good, indicating the uncertainty in extracting these strengths. This work has shown that 240 MeV ^{6}Li scattering is a viable way to study the ISGMR and ISGQR and can be particularly useful in rare isotope studies where ^{6}Li can be used as the target.

DEDICATION

To my wife, Yongmei, my lovely daughters, Yan and Lucy, and my parents

ACKNOWLEDGEMENTS

I would like to express my special thanks to Dr. Dave Youngblood who has been a very generous advisor, for his guidance and encouragement during my Ph.D research program. He taught me very valuable knowledge that an experimental physicist should have. Whenever I had a problem in my research, talking with him was always an effective way to understand and solve it. I would like to sincerely thank Dr. Yiu-Wing Lui who taught me how to do experiments efficiently and accurately. As a mentor and friend of mine, he gave me valuable suggestions for my research and my life. I would like to extend my special thanks to Dr. Henry Clark who taught me first hand the detection techniques used in experiments, and to Dr. Yoshiaki Tokimoto who was a very nice and quiet colleague and also a friend of mine. We cooperated very well during many experiments.

Special thanks are extended to Dr. Dao Tien Khoa, Dr. Livius Trache, Dr. Flourin Carstoiu and Mr. Hoang Sy Than for their help in folding calculation used for data analysis.

I would like to thank Dr. Shalom Shlomo, Dr. Robbert E. Tribble and Dr. Joseph B. Natowitz for serving as my advisory committee members and for their valuable advice and suggestions.

I would like to acknowledge the K500 Cyclotron operating staff, people in the machine shop and the electronic shop; because of their support, my Ph.D research went smoothly and successfully.

A sincere thanks also goes to my friends in the Cyclotron Institute, Mr. Lijun Qin, Dr. Changbo Fu, Dr. Yongjun Zhai, Dr. Wei Liu, Dr. Xiaodong Tang, Dr. Yong Peng, Dr. Tariq Al-Abdulla, Dr. Au Kim Vuong and Dr. Gabriel Tabacaru.

I also want to extend my gratitude to the Robert A. Welch foundation for the financial support during my Ph.D research program.

Finally, thanks to my mother and father for their encouragement and to my wife for her patience and love. Without them I could not have made it.

TABLE OF CONTENTS

LIST OF FIGURES

Page

Page

Page

Page

Page

Page

Page

LIST OF TABLES

Page

Page

1. INTRODUCTION

1.1 Nuclear Matter and Nuclear Compressibility

Nuclear matter is a theoretically constructed infinite system of nucleons with a fixed ratio of neutron to proton numbers and no Coulomb interaction. Study of nuclear matter is of interest in nuclear physics to test many-body theory as well as in astrophysics to study supernova collapse and neutron stars. To accurately determine the nuclear matter (NM) equation of state (EOS), E=E(ρ), is the main goal of the study of the nuclear matter. However, it is not an easy task to get information about its properties since nuclear matter does not exist in the laboratory. There are three important parameters which characterize nuclear matter: the saturation density, the binding energy, and the compressibility. The saturation density $\rho_0 = 0.17$ fm^{-3} has been obtained from electron scattering and the binding energy $E(\rho_0) = -16$ MeV was obtained by extrapolating the masses of finite nuclei and are known with "good accuracy" [1]. The nuclear matter compressibility, K_{nm} is directly related to the curvature of the nuclear matter equation of state [2] at the saturation point. K_{nm} is defined by:

$$K_{nm} = k_f^2 \frac{d^2(E/A)}{dk_f^2}\Big|_{k_{f0}} = 9\rho_0^2 \frac{d^2(E/A)}{d\rho^2}\Big|\rho_0 \,, \tag{1.1}$$

where E/A is the binding energy per nucleon of the nuclear matter, and k_{f0} is the Fermi momentum and ρ_0 is the nuclear matter density at the saturation point.

There were quite a few attempts to constrain the nuclear compressibility K_{nm} with data from nuclear physics, such as nuclear masses, nuclear radii and high energy nuclear collisions, and from astrophysics such as supernova collapse and neutron stars masses [3]. However, all these attempts could not give an effective constraint on nuclear compressibility until the isoscalar giant monopole resonance (ISGMR) in nuclei was discovered [4] and used to determine K_{nm}. The most recent value determined from comparison with calculations using the Gogny interaction is 231±5 MeV [5], however

This dissertation follows the style of Physical Review C.

there are both theoretical and experimental issues remaining, some of which are the subject of this dissertation.

1.2 Nuclear Giant Resonances

Giant resonances are small amplitude, high frequency, collective modes of excitation of a nucleus. In 1947, Baldwin and Klaiber [6] observed a strong resonance behavior in photon-induced reactions. This resonance turned out to be the electric isovector giant dipole resonance (IVGDR). Very soon it was found that these giant resonances were a general feature of all nuclei. The centroid energy can be described in medium and heavy nuclei by the relation [7]

$$E_c = 31.2A^{-1/3} + 20.6A^{-1/6}\ MeV \tag{1.2}$$

where A is the nuclear mass for a certain nucleus. Goldhaber and Teller explained this as a collective vibration of protons against neutrons. In 1972, the isovector giant quadrupole resonance (IVGQR) was first reported by inelastic electron scattering in ^{90}Zr [8] and a resonance thought to be the isoscalar giant quadrupole resonance (ISGQR) was observed in electron scattering [9] and in proton inelastic scattering [10] from spherical nuclei. Alpha inelastic scattering was later used to definitively identify this as the ISGQR and to systematically investigate the ISGQR from heavy to light nuclei [11-15]. The shape and width of ISGQR change smoothly from heavy to medium nuclei and the centroid energy in heavy nuclei can be described by the relation:

$$E_c \approx 63A^{-1/3}\ MeV\ . \tag{1.3}$$

In 1977, D.H. Youngblood *et al.* [4] reported the discovery of the ISGMR in ^{144}Sm and ^{208}Pb with α inelastic scattering. A systematic study of the properties of ISGMR [16] in many nuclei was reported later with a centroid energy in heavier nuclei of

$$E_C \approx 76A^{-1/3}\ MeV\ . \tag{1.4}$$

The discovery of ISGMR provided an effective way to determine the nuclear compressibility and K_{nm} obtained varied from 180 MeV to 230 MeV depending on the nucleus used. In 1980, the isoscalar giant dipole resonance (ISGDR) was observed with 172 MeV α inelastic scattering from ^{208}Pb [17]. The ISGDR centroid can also be related to the nuclear compressibility.

In the macroscopic liquid drop model, protons and neutrons are treated as independent fluids. Giant resonances therefore can be described as shape or density oscillations of nuclei. Giant resonances can be classified into two groups by spin, namely electric oscillations ($\Delta S=0$) and magnetic oscillations ($\Delta S=1$) [18]. They also can be classified into two groups by isospin, namely isoscalar mode ($\Delta T=0$) and isovector mode($\Delta T=1$). In isoscalar oscillations, protons and neutrons move in phase, while in isovector oscillations, protons and neutrons move out of phase. The possible giant oscillation modes of a nucleus with multipoles $L \leq 2$ are illustrated in Fig. 1.1.

From the microscopic point of view, giant resonances can be described as a coherent superposition of particle-hole excitations resulting from the action of an electromagnetic operator on the ground state of the nucleus, and for isoscalar transition with $L \geq 2$

$$O_{LM} = \sum_i r_i^L Y_{LM}(\Omega) \qquad L \geq 2 . \tag{1.5}$$

The qualitative features of giant resonance can be understood by considering the nuclear shell model [7, 18]. According to the shell model, the parity of the single particle wave function in subsequent shells N, N+1, N+2 is alternating, and the energy difference between subsequent shells $\Delta E = \hbar\omega = 41A^{-1/3}$ MeV. Parity conservation requires that odd L resonance transitions can only happen when $\Delta N=1,3,\ldots$ and even L resonance transitions can only happen when $\Delta N=0, 2, 4,\ldots$ (see Fig. 1.2). So the resonance energy

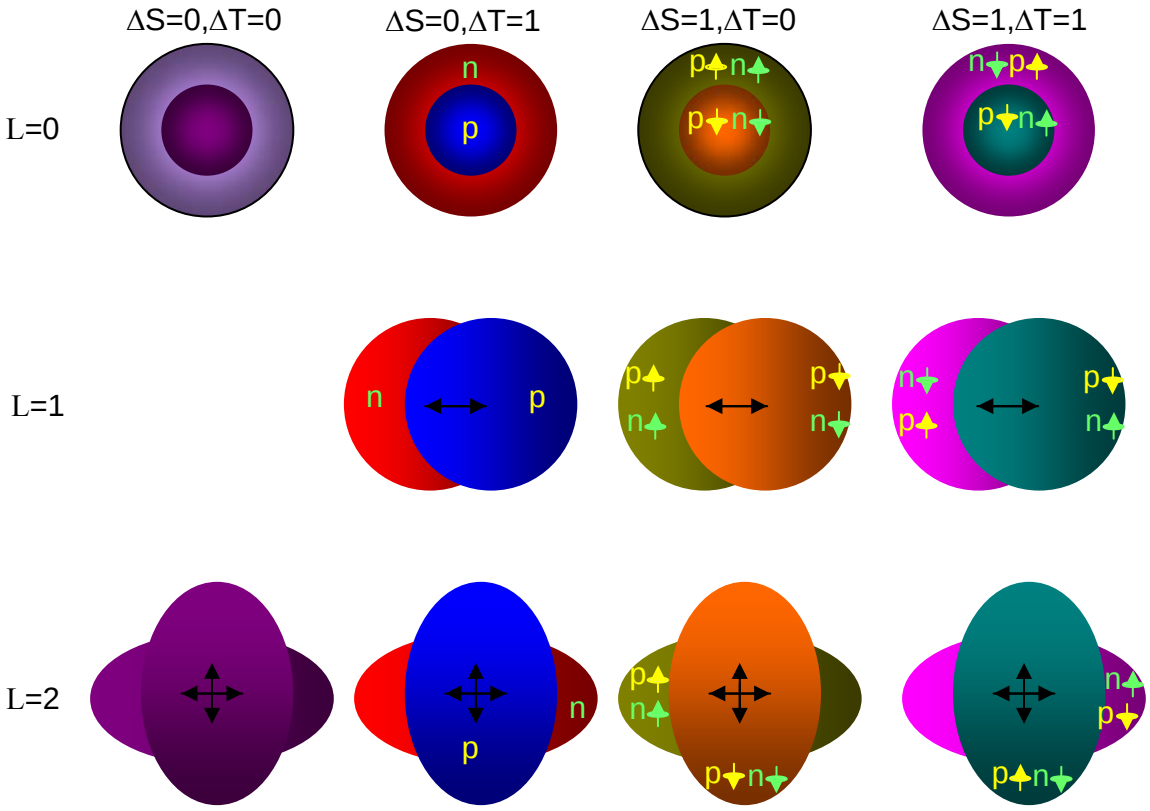

FIG. 1.1 Qualitative picture of giant resonance modes of the nucleus (originally from [18]).

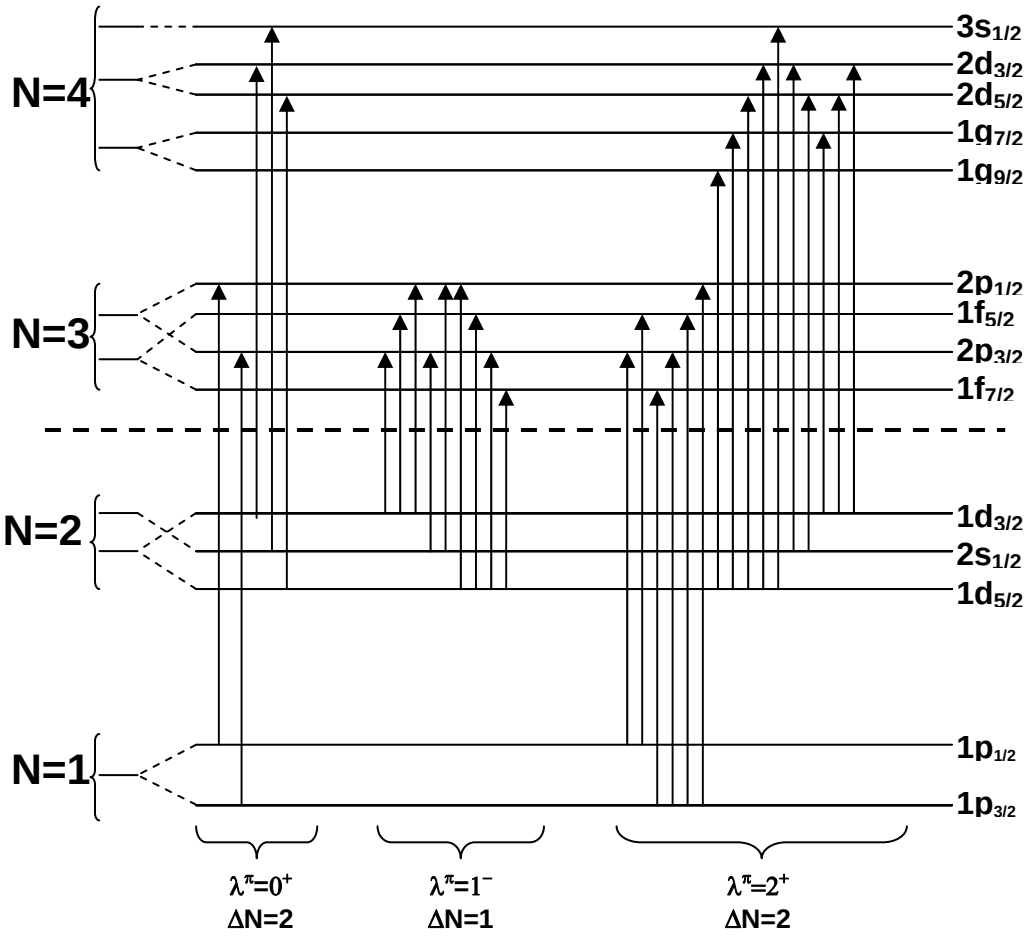

FIG. 1.2 Schematic representation of E0, E1, E2 transitions between shell model states[19].

Table 1.1 Qualitative estimation of energy of giant resonance in nuclear shell model.

	Multipolarity	ΔE		Multipolarity	ΔE
ISGMR	0	$2\hbar\omega$	ISGQR	2	$(0\hbar\omega), 2\hbar\omega$
ISGDR	1	$(1\hbar\omega), 3\hbar\omega$	ISGOR	3	$1\hbar\omega, 3\hbar\omega$
IVGDR	1	$1\hbar\omega$			

can be estimated as $\Delta E=\Delta N\times\hbar\omega$ (as shown in Table 1.1). In a schematic model the residual particle-hole interaction gives rise to the formation of one strong collective state which is a coherent superposition of all possible particle-hole interactions of a given multipolarity and parity. Since the residual p-h interaction is attractive for isoscalar and

repulsive for isovector excitations, the isoscalar resonances will be located below and the isovector resonances above the unperturbed energy $\Delta N \times \hbar\omega = \Delta N \times 41 A^{-1/3}$ MeV. Because of this, the ISGMR and IVGDR are located at approximately the same excitation energy (see Fig. 1.3).

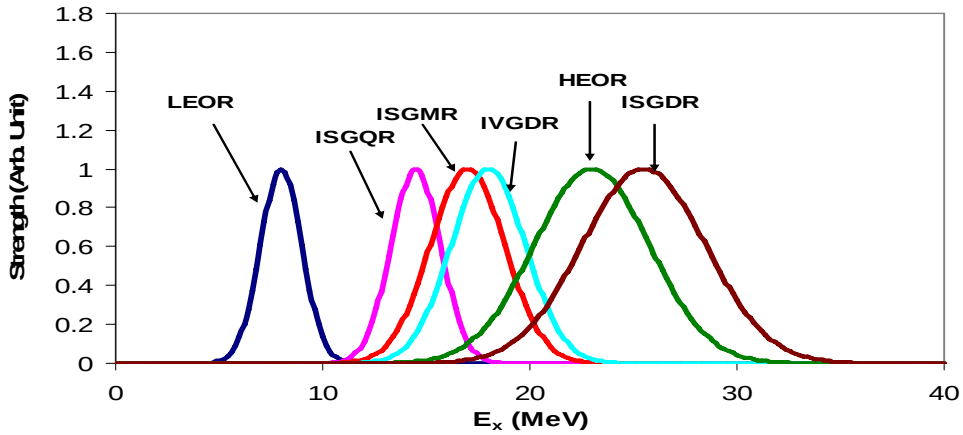

FIG. 1.3 Hypothetical centroid energies and strength distributions for different electric giant resonance modes for a nucleus with mass A~100. The peak strength for each mode is arbitrary.

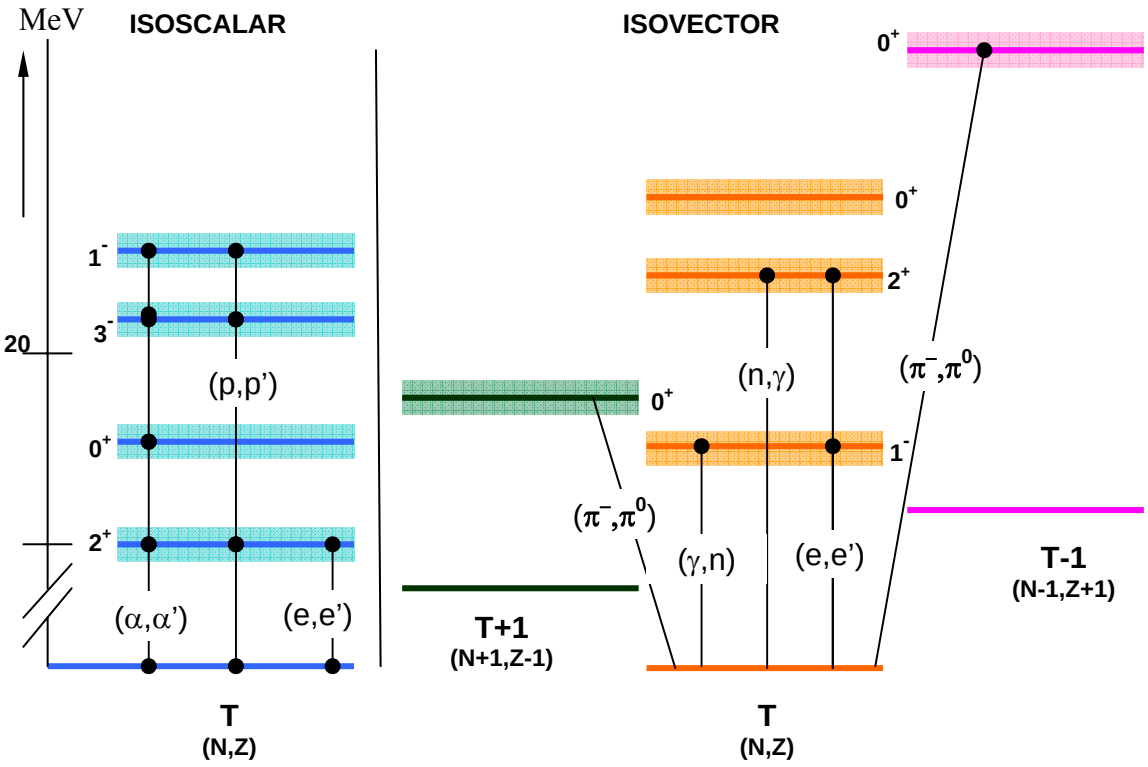

FIG. 1.4 The main experimental tools used to study giant resonances (see Ref. [20]).

The experimental tools used to study different giant resonances are shown in Fig. 1.4 (see [20]). Inelastic scattering of α particles is a strong isoscalar (N = Z) selective probe which has been the main tool used to study isoscalar giant resonances. Inelastic scattering of proton [21], deuteron [22] and ^{3}He [23] have also been used to study isoscalar giant resonances. Electron inelastic scattering has some advantages in giant resonance studies, since the form factor can be calculated accurately and the angular distribution are often characteristic of the multipolarity, and the physical continuum background from multi-step excitation is small due to the weak electromagnetic interaction. However, electron scattering has a large contribution from the radiative tail which increases background substantially and it excites strongly both isoscalar and isovector excitations, which particularly affect the study of the ISGMR where the IVGDR lies at nearly the same energy. To study isovector resonances one needs a probe

which can distinguish between protons and neutrons. Electron scattering and γ-absorption are useful tools for studying the IVGDR, while pion charge exchange reactions provide an opportunity to study the IVGMR.

1.3 The Compressional Mode Giant Resonance and Nuclear Compressibility

According to the liquid drop model [2], in addition to the surface oscillations, a liquid drop possesses normal modes of vibration involving compression of the density (sound wave), which are called compression modes. Among all the nuclear properties which are potentially affected by the compressibility K_{nm}, the compression mode of giant resonances is certainly the most sensitive one. The energy of the compression mode can be simply related to the compressibility by the following [2]

$$E_{comp} \propto \sqrt{\frac{\hbar^2 K_{nm}}{9R_0^2 m}} \tag{1.6}$$

where m is the nucleon mass and $R_0 = 1.2A^{1/3}$. In compression modes, ISGMR can be simply viewed as a volume oscillation of the nucleus, while ISGDR may be physically visualized as a compression wave moving back and forth-akin to a sound wave-in a nucleus with the volume of the nucleus remaining constant [24]. The ISGDR has been referred as the "squeezing mode", in tune with the term "breathing mode" for the GMR.

From a microscopic point of view, both the ISGMR and ISGDR are second-order effects, which means that the transition operator is related to r^2Y_{00} for ISGMR or r^3Y_{10} for ISGDR (to first order, the transition operator for ISGMR is a constant which cannot induce any transitions from the ground state to excited states, and that for ISGDR corresponds to the spurious center-of-mass motion).

What one measures in experiments studying the ISGMR and ISGDR are strength distributions as a function of excitation energy. The energies of the ISGMR and ISGDR can be expressed as ratios of different moments of the strength distributions, in which the k_{th} moment of the strength distribution is:

$$m_k = \sum_n (E_{n0})^k \left|\langle n|F|0\rangle\right|^2 \tag{1.7}$$

where E_{n0} is the excitation energy of the state $|n\rangle$ and F is the excitation operator for ISGMR and ISGDR. F may be expressed as [1]

$$F = \sum_{i=1}^{A} r_i^2 Y_{00} \tag{1.8a}$$

for ISGMR and [1]

$$F = \sum_{i=1}^{A} f_\eta(\vec{r}) = \sum_{i=1}^{A} (r_i^3 Y_{10} - \eta r_i Y_{10}) \tag{1.8b}$$

for ISGDR, where the value of η is obtained from the coherent spurious state transition density[25]. In the scaling model, the mean energy $\overline{E}$ is defined as[26]:

$$\overline{E} = \sqrt{\frac{m_3}{m_1}} = \frac{\sum_n (E_{n0})^3 \left|\langle n|F|0\rangle\right|^2}{\sum_n E_{n0} \left|\langle n|F|0\rangle\right|^2}. \tag{1.9}$$

Then the energies can be expressed in term of an effective compression modulus K_A for the nucleus of mass A by the formula [26]

$$\overline{E}_0 = \sqrt{\frac{\hbar^2 A K_A}{m\langle r^2\rangle_0}} \tag{1.10}$$

for ISGMR, and

$$\overline{E}_1 = \sqrt{\frac{7}{3}\frac{\hbar^2 (K_A + \frac{27}{25}\varepsilon_F)}{m\langle r^2\rangle_0}} \tag{1.11}$$

for ISGDR, where m is the nucleon mass, $\langle r^2\rangle_0$ is the average r^2 over the ground state. All the information about the nuclear matter compression modulus which can be extracted from the data is contained in K_A.

There are two approaches to relate K_A to K_{nm}. In the semi-empirical (macroscopic) approach, which is similar to the semi-empirical mass formula, K_A is expressed as an expansion with contributions from volume, surface, symmetry and coulomb terms:

$$K_A = K_{vol} + K_{surf} A^{-1/3} + K_{sym}\left(\frac{N-Z}{A}\right)^2 + K_{Coul}\frac{Z^2}{A^{4/3}} + \cdots. \tag{1.12}$$

The determination of the various parameters K_i ($K_i = K_{vol}, K_{surf}, K_{sym}, K_{Coul}\ldots$) is done by fitting ISGMR data from many nuclei. K_{nm} is identified with the volume term K_{vol}. However, this approach suffers from several ambiguities [27-29]. The first one is related to the interpretation of the volume term. The assumption

$$K_{nm} = \lim_{A\to\infty} K_A = K_{vol} \tag{1.13}$$

holds only if the ISGMR is well described by scaling model. The scaling model may give a reasonable approximation in some heavy nuclei, but it is not such a good approximation in light nuclei, which make the interpretation of K_{vol} somewhat uncertain. Also the assumption that the breathing mode is a small amplitude vibration, which is the basis to derive the K_A expression (1.12) and E_0 expression (1.10), is only true for heavy nuclei. In lighter nuclei, the breathing mode is anharmonic[28]. This further complicates the interpretation of the various terms in Eq. (1.12). Another ambiguity [27, 29] relates to the possibly poor convergence of the expansion (1.12), and the fact that it is not clear whether the variation of K_A over the range of nuclei considered can be well accounted for by the smooth behavior implied by Eq.(1.10).

In the microscopic approach, the self-consistent Hartree-Fock (HF) random-phase-approximation (RPA) [2, 30, 31] is used to calculate strength distributions for ISGMR and ISGDR, with various effective nucleon-nucleon interactions which differ in their value for K_{nm}. The value of K_{nm} thus can be constrained by comparing the experimentally extracted strength distributions of ISGMR and ISGDR with those from HF-RPA calculations. An essential feature of this approach is that the same level of

approximation is implemented in both finite and infinite systems, and the same parameterization of the effective interaction is used in both cases.

In the HF approach, the ground state wave function of a nucleus with A nucleons is a Slater determinant obtained from the single-particle wave function with the assumption that each nucleon moves in a mean field created by all the nucleons. Thus the ground state of the nucleus can be approximately expressed in terms of independent single nucleon motions in the average field. The basic properties of nuclei have been described successfully with HF theory. The collective motions have been well described within the RPA theory in terms of coherent particle-hole (p-h) excitations. In the self-consistent HF-RPA calculation [30], one starts by adopting a specific effective NN interaction V_{12}, such as a Skyme interaction, with parameters obtained by fitting the experimental data of the bulk properties of finite nuclei within HF approximation. Then one solves the RPA equations, using the p-h interaction V_{ph} which corresponds to V_{12}, and calculates the strength distribution S(E) and the centroid energy associated with a certain scattering operator F as shown in (1.8a) and (1.8b) for ISGMR and ISGDR.

The analysis of ISGMR with HF-RPA calculations, with Skyme interaction [32], currently gives a value of compressibility K_{nm}=210-220 MeV, while the analysis of ISGDR predicts a value of K_{nm}=160-180 MeV. The discrepancy of 20% between the value of K_{nm} obtained from ISGMR and that obtained from ISGDR, was a long standing problem which puzzled people for almost one decade. Shlomo *et al*. [1, 33, 34] pointed out that several aspects accounted for the discrepancy: i) the HF-RPA calculations used to extract strength distributions for giant resonances were not fully self-consistent, which introduces spurious state mixing (SSM) in the ISGDR and thus brings considerable uncertainty in determining the strength distribution; ii) The maximum cross-section for the ISGDR decreases strongly at high energy and may drop below the experimental sensitivity for excitation energies above 30 MeV, so the missing experimental strength in high excitation region leads to a reduction of more than 3 MeV in the ISGDR centroid energy which can significantly affect the comparison between theory and experiment;

iii) Current experimental methods adopted to extract the strength distribution, using the collective model shapes for transition density, tend to overestimate the ISGDR EWSR by up to 20%, which may shift the centroid energies a few percent.

In addition to HF-RPA approach mentioned above, which is usually denoted as non-relativistic, a fully consistent relativistic random phase approximation (RRPA)[35], based on effective mean field Lagrangians with nonlinear meson self-interaction terms, has been used to calculate ISGMR and ISGDR distributions. A comparison between experimental and calculated energies of ISGMR points to a value of 250-270 MeV for K_{nm}, which is 20% higher than the value for K_{nm} obtained in the non-relativistic HF-RPA calculation. Piekarewicz [36] and Shlomo *et al*. [34, 37, 38] have shown that the difference in the values of K_{nm} obtained in the relativistic and non-relativistic models is mainly due to the differences in the values of the symmetry energy coefficient J and its slope L associated with these models.

According to Shlomo *et al.* [34], correction of non-fully consistency in non-relativistic HF-RPA calculations for ISGMR may change the K_{nm} value obtained with the Skyrme interaction from 210-220 MeV to 230-240MeV, in agreement with that obtained with the Gogny interaction. It is also possible to build *bona fide* Skyrme forces where K_{nm} is close to the relativistic value, 250-270MeV. Therefore K_{nm}=240±20MeV can be obtained with non-relativistic fully self-consistant HF-RPA calculation. The uncertainty of about 20 MeV is mainly due to the uncertainty in the value of the overall shape of the nuclear matter symmetry energy curve, as a function of density. In order to determine the K_{sym} accuratelly, the systematic study of ISGMR over a wide range of (N-Z)/A is necessary and more information on ISGDR will be also very helpful to check the obtain K_{nm}.

1.4 Motivations

Alpha inelastic scattering at small angles, including 0^0, has been successfully used to study the ISGMR of heavy and medium nuclei [5] (as shown in Table 1.2) where the

monopole resonance is concentrated in a broad peak. For light nuclei (A<40), however, ISGMR strengths are more elusive [39-41] because the resonance is fragmented and extends to excitation energies above 35 MeV. Unfortunately, other processes, such as multi-step reactions, give a large physical background at high excitation energy in α inelastic scattering, which makes it difficult to extract strengths in this range.

Table 1.2 Fractional energy weight sum rule (EWSR) exhausted in the given excitation energy range for nuclei from light to heavy obtained with α scattering, with m_k being k_{th} moment of the strength distribution (k = -1, 0, 1, 3).

	E_x Energy range (MeV)	m_1/m_0	$\sqrt{m_1/m_{-1}}$	$\sqrt{m_3/m_1}$	EWSR (%)	Ref.
^{12}C	13.0~45.0	21.9±0.3			~27±5	[41]
^{16}O	11.0~40.0	21.39±0.49	19.63±0.38	24.89±0.59	~48±10	[42]
^{24}Mg	10.0~40.0	$21.93^{+0.33}_{-0.25}$ [a]	$20.83^{0.28}_{-0.22}$ [a]	$24.65^{+0.53}_{-0.31}$ [a]	~82±9[a]	[39]
^{28}Si	8.0~37.0	21.25±0.38	20.13±0.38	23.7±0.7	~81±10	[40]
^{40}Ca	8.0~35.0	$18.39^{+0.49}_{-0.35}$	17.58±0.40	$20.42^{+0.89}_{-0.36}$	~100±11	[43]
^{46}Ti	9.0~39.0	$18.66^{+0.65}_{-0.25}$	$18.1^{+0.5}_{-0.2}$	$20.47^{+1.41}_{-0.49}$	$\sim 71^{+15}_{-12}$	[44]
^{48}Ti	9.0~39.0	$18.80^{+0.45}_{-0.18}$	$18.33^{+0.36}_{-0.15}$	$20.25^{+0.99}_{-0.28}$	$\sim 96^{+14}_{-12}$	[44]
^{56}Fe	10.0~40.0	$18.35^{+0.33}_{-0.19}$	$17.92^{+0.26}_{-0.15}$	$19.57^{+0.73}_{-0.16}$	$\sim 98^{+14}_{-10}$	[45]
^{58}Ni	10.0~40.0	$19.20^{+0.44}_{-0.19}$	$18.70^{+0.34}_{-0.17}$	$20.81^{+0.90}_{-0.28}$	$\sim 85^{+13}_{-10}$	[45]
^{60}Ni	10.0~40.0	$18.04^{+0.35}_{-0.23}$	$17.55^{+0.27}_{-0.17}$	$19.54^{+0.78}_{-0.23}$	$\sim 82^{+13}_{-11}$	[45]
^{90}Zr	10.0~35.0	$17.81^{+0.32}_{-0.20}$	$17.55^{+0.25}_{-0.18}$	$18.69^{+0.65}_{-0.30}$	~100±12	[46]
^{110}Cd	10.0~35.0	$15.12^{+0.21}_{-0.11}$	$14.96^{+0.13}_{-0.12}$	$15.58^{+0.40}_{-0.09}$	$\sim 88^{+0.21}_{-0.13}$	[47]
^{112}Cd	10.0~35.0	$14.50^{+0.32}_{-0.16}$	$14.31^{+0.20}_{-0.,17}$	$15.02^{+0.37}_{-0.12}$	$\sim 104^{+0.23}_{-0.13}$	[47]
^{112}Sn	10.0~35.0	$15.43^{+0.11}_{-0.10}$	15.23±0.10	$16.05^{+0.26}_{-0.14}$	$\sim 116^{+13}_{-18}$	[48]
^{116}Sn	10.0~35.0	15.62±0.20[b]	15.45±0.20[b]	16.13±0.20[b]	~112±15	[49]
^{124}Sn	10.0~35.0	14.50±0.14	$14.33^{+0.17}_{-0.14}$	$14.96^{+0.11}_{-0.10}$	~104±11	[48]
^{144}Sm	10.0~35.0	14.67±0.30[b]	14.60±0.30[b]	15.12±0.30[b]	~92±12	[49]
^{208}Pb	10.0~35.0	13.77±0.20[b]	13.69±0.20[b]	14.00±0.20[b]	~99±15	[49]

a: Ref. [50], b: Ref. [51]

^{6}Li scattering could be an alternate way to study giant resonances. As an isoscalar projectile (N = Z), ^{6}Li scattering preferentially excites isoscalar resonances as does α scattering. The low particle emitting threshold for ^{6}Li will give a large breakup probability into dominant channel ^{6}Li→ α + d. Therefore the contribution of multi-step processes to the ^{6}Li outgoing channel is low, especially at higher excitation energy, and a better ratio between the resonance peak and the continuum is expected. ISGMR studies in ^{12}C and ^{24}Mg with 156 MeV ^{6}Li inelastic scattering have been reported respectively by W. Eyrich *et al*. [52] and H. Dennert *et al*. [53]. However, the low bombarding energy limited the useful excitation energy range to $E_x \leq 30$ MeV. We expect 240 MeV ^{6}Li scattering can give us a better opportunity to study giant resonances at higher energy in light nuclei.

Another important motivation for ^{6}Li scattering study is to explore the possibility of expanding current research from stable nuclei to radioactive nuclei with inverse reactions. Inverse reactions have to be used because it is impossible to make targets of these unstable nuclei, so they will be used as projectiles. It is difficult to make a helium target, but a ^{6}Li target is relatively easy to make.

1.5 Dissertation Outline

The dissertation consists of five sections. Section 1 presents an introduction of nuclear matter compressibility K_{nm}, giant resonances, the relation between K_{nm} and compression modes resonances, and current status of K_{nm} determination via ISGMR and ISGDR studies. The motivations to study ^{6}Li scattering are also given in this section. The Energy Weighted Sum Rule (EWSR) and scattering theory are introduced in section 2. Since the energy weighted sum rule is used as a measurement of the strength of giant resonances, EWSR and transition density for ISGMR, ISGDR and isoscalar modes with $L \geq 2$ are introduced in this section. Then general scattering theory with DWBA calculations is presented to give a clear picture about how the cross-section of the scattering system can be obtained by solving the Schödinger equation. The optical potential in terms of

empirical Woods-Saxon (W-S) parameterization, which has been widely used to analyze nuclear elastic scattering, is introduced briefly. Folding model with M3Y nucleon-nucleon (NN) effective interaction, which is another way to construct the optical potential in the frame of Feshbach's reaction theory, is introduced as well as the folding model with JLM NN effective interaction. The transition potentials for inelastic scattering are also given in this section. In the end of section 2, different computer codes**,** **CHEN2**, **DFPD4**, **ECIS**, **OPTJLM1**, used for folding calculations and DWBA calculation, are introduced and calculations with **DFPD4** and **ECIS** for a known scattering system are compared to those obtained with **DOLFIN** and **PTOLEMY**. In section 3, the experimental setup of the multipole-dipole-multipole (MDM) spectrometer, the operation of focal plane detector and electronics are introduced. Detector calibrations, and the procedure to extract the differential cross-sections data points from raw data, are also included in this section. Section 4 gives a detailed description and discussion of the data analysis, which includes: procedure of data analysis; data analysis of ^{6}Li+^{116}Sn scattering; data analysis of ^{6}Li scattering on ^{28}Si and ^{24}Mg. Section 5 contains the summary and conclusions.

2. COLLECTIVE MOTION AND SCATTERING THEORY

The fact that inelastic scattering is appropriate to study giant resonances is based on the following: a) giant resonances are a collective motion of nuclear excitation; b) inelastic scattering is very sensitive to coherent, collective motions of the target nucleons and, many of the characteristic features of the scattering are embodied most simply in calculations based on the collective model form factor. The collective model will be introduced in SECTION 2.1, which emphasizes the derivations of transition density and energy weighted sum rule (EWSR) for giant resonances with different multipolarities. A general scattering theory is introduced in SECTION 2.2 to provide a framework within which different physical models can be embedded. The formal solution of the scattering problem and the distorted wave Born approximation (DWBA) are given in this SECTION. In SECTION 2.3, the optical potential model used to analyze elastic scattering in term of W-S potential parameters is introduced briefly. The optical potential obtained from the folding model calculation with M3Y nucleon-nucleon effective interaction is described and discussed as well as that obtained with JLM interaction. Transition potentials for analysis of inelastic scattering are introduced in SECTION 2.4. Several computer codes used to carry out double folding calculations and DWBA calculations are introduced in SECTION 2.5.

2.1 Collective Model

The collective model describes nuclear excitations induced by static or dynamic deformations of the nucleus. The details of the collective model were described by Bohr and Mottelson [2]. The density and shape vibrations of the nuclei are among the most easily recognized collective motions, which may occur both as discrete, low-lying states and as high-lying giant resonance. Isoscalar giant resonances with low multipolarites such as L = 0 - 3 can be excited simultaneously by inelastic scattering of isoscalar nuclear probe. The main concern here is to construct the transition density for nuclear excited states and obtain the EWSR for each multipolarity.

2.1.1 Deformation and Transition Density for L≥2

The basic idea to obtain the transition density is to take a spherically symmetric density distribution ρ(r) and introduce certain multipole deformation parameters $\alpha_{\lambda\mu}$ to describe deformed nucleus. These parameters are dynamic variables of the collective model. A standard method to introduce the deformation of a nucleus is given below [54]. Assuming an incompressible nucleus with a density distribution ρ(r) = constant in the interior and a sharp edge at r = R_0, the deformation is then introduced by making the edge position angular dependent:

$$R_0 \to R(\theta,\varphi) = R_0\left[1+\sum_{\lambda\mu}\alpha_{\lambda\mu}Y_\lambda^\mu(\theta,\varphi)\right] = R_0 + \delta R(\theta,\varphi) \tag{2.1}$$

where L ≥ 2. This above prescription can be easily transferred to a nuclear density distribution with the Fermi density shape:

$$\rho(r,R_0) = \frac{\rho_0}{1+e^{\frac{r-R_0}{a}}} \tag{2.2}$$

where R_0 represents the half-density radius and a is diffusion parameter. A Taylor series may be used to obtain the deformed density distribution which is

$$\rho(r,\theta,\varphi) = \rho(r,R(\theta,\varphi)) \approx \rho(r,R_0) + \sum_{n=1}^{\infty}\frac{(\delta R)^n}{n!}\left[\frac{d^n\rho(r,R)}{dR^n}\Big|_{R=R_0}\right] \tag{2.3a}$$

where

$$\delta R = R_0\sum_{\lambda\mu}\alpha_{\lambda\mu}Y_\lambda^\mu(\theta,\varphi)\,. \tag{2.3b}$$

On the other hand, the deformed density can always be decomposed in a multipole expansion

$$\rho(r,\theta,\varphi) = \sum_{lm}\rho_{lm}(r)Y_l^m(\theta,\varphi)^* \tag{2.4a}$$

where

$$\rho_{lm}(r) = \int \rho(r,\theta,\varphi) Y_l^m(\theta,\varphi) d\hat{\vec{r}}\,, \tag{2.4b}$$

which actually represents the transition density for inelastic transitions. We know that, if the density is only a function of (r - R_0) as shown in eq.(2.2), then we have

$$\frac{d^n\rho}{dR_0^n} = (-1)^n \frac{d^n\rho}{dr^n}\,. \tag{2.5}$$

With the first order approximation of (2.3a) and considering Eq.(2.4) and Eq.(2.5), the transition density can be expressed as

$$\rho_{lm}(r) = f_l(r)\alpha_{lm}, \quad where\ f_l(r) = -R_0\left[\frac{d\rho(r,R_0)}{dr}\right]. \tag{2.6}$$

2.1.2 Transition Density for Monopole Breathing Mode

Besides nuclear shape vibrations, it is possible that the central density of the nuclear matter oscillates about its equilibrium value with high frequency, which is referred as monopole breathing mode. With the simple radial scaling [55]

$$r \to r' = r(1-\alpha_0)\,, \tag{2.7}$$

the transition density can be related to the equilibrium density ρ(r) by the following expression

$$\rho(r) \to N\rho(r') = \rho(r) + \delta\rho(r) \tag{2.8}$$

where N is the renormalization factor to satisfy the particle number conservation law, which requires

$$\int \delta\rho(r) r^2 dr = 0\,. \tag{2.9}$$

From Eq.(2.7), we have:

$$N\rho(r') = N\rho(r - r\alpha_0) \approx N\rho(r) - Nr\alpha_0 \frac{d\rho(r)}{dr} = \rho(r) + \delta\rho(r), \tag{2.10}$$

so the transition density can be expressed as:

$$\delta\rho(r) = (N-1)\rho(r) - Nr\alpha_0 \frac{d\rho(r)}{dr}. \tag{2.11}$$

With the constraint of Eq. (2.9), one can obtain

$$N = \frac{1}{1+3\alpha_0} \approx 1 - 3\alpha_0 \tag{2.12}$$

where $3\alpha_0 << 1$, and the transition density is

$$\delta\rho(r) \approx -\alpha_0 \left[3\rho(r) + r\frac{d\rho(r)}{dr} \right]. \tag{2.13}$$

2.1.3 Energy Weighted Sum Rule (EWSR) and Sum Rule Limit Deformation

It is often useful to apply general relations in the form of sum rules obtained from algebraic relations between operators to study complex systems like one described by collective model. For example, the EWSR is often used as a measurement of the strength of giant resonances. It is defined as a sum of the transition possibilities from ground state to excited states for certain multipolarity, multiplied respectively by the excitation energy [2]

$$\boldsymbol{S(Q) \equiv \sum_n (E_n - E_0) \left| \langle n|Q|0\rangle \right|^2 = \frac{1}{2} \langle 0|[Q,[H,Q]]|0\rangle} \tag{2.14}$$

where n labels the complete set of excited states that can be reached by operating with Q on the ground state $|0\rangle$. Assuming Q is a one-particle moment depending only on the spatial coordinates

$$Q = \sum_i Q(\vec{r}_i) \tag{2.15}$$

and the interactions do not explicitly depend on the velocity of the particles, The EWSR can be expressed as

$$S(Q) = \left\langle 0 \left| \sum_i \frac{\hbar^2}{2m} (\nabla_i Q(\vec{r}_i))^2 \right| 0 \right\rangle \tag{2.16}$$

where m is the mass of the particle. For a multipole field operator

$$Q = \sum_i f(r_i) Y_L^M(\Omega_i), \tag{2.17}$$

the EWSR can be evaluated by means of the gradient formula [2] and is obtained as

$$S(Q) = \frac{2L+1}{4\pi} \frac{\hbar^2}{2m} A \left\langle (\frac{df}{dr})^2 + L(L+1)(\frac{f}{r})^2 \right\rangle \tag{2.18}$$

where A is the particle number of the system. With the isoscalar mass operator Q_{0LM} ($L \geq 2$) [56, 57]

$$Q_{0LM} = \sum_{i=1}^{A} r_i^L Y_L^M(\Omega_i), \tag{2.19}$$

the corresponding EWSR is obtained

$$S(Q_{0LM}) = \frac{\hbar^2 A}{8\pi m} L(2L+1)^2 \left\langle r^{2L-2} \right\rangle, \tag{2.20}$$

which is approximately independent of assumptions about nuclear structure.

In the macroscopic liquid drop model, assuming the excited nucleus has a continuous density distribution $\rho(r, R(\theta,\varphi))$ as discussed in part A, the isoscalar mass operator can be transformed as

$$Q_{0LM} = \int r^L Y_L^M(\theta,\varphi) \rho(r,\theta,\varphi) d\vec{r} = \int \rho_{LM}(r) r^{L+2} dr. \tag{2.21}$$

Substituting Eq. (2.6), we can obtain

$$Q_{0LM} = -\int R_0 \frac{d\rho}{dr} r^{L+2} \alpha_{LM} dr = \frac{(L+2)}{4\pi} A R_0 \left\langle r^{L-1} \right\rangle \alpha_{LM} . \tag{2.22}$$

In the vibrational model treating the small oscillations in shape about a spherical mean, the α_{LM} are now quantal operators that will create or annihilate one quantum or phonon. The transition probability for the mass multipole operator can then be expressed as

$$B(0 \to L) = \left| \left\langle L, M \left| Q_{0LM} \right| 0 \right\rangle \right|^2 = \frac{(L+2)^2}{(4\pi)^2} A^2 R_0^2 \left\langle r^{L-1} \right\rangle^2 \beta_L^2 \tag{2.23}$$

where $\beta_L^2 = \left| \left\langle LM \left| \alpha_{LM} \right| 0 \right\rangle \right|^2$ is the amplitude of the oscillation. Assuming the single state exhausts the total sum rule (see Eq. (2.20)), we get sum rule limits on the deformation parameters for $L \geq 2$

$$\delta_L^2 = \beta_L^2 R_0^2 = \frac{2\pi\hbar^2}{m A E_x} \frac{L(2L+1)^2}{(L+2)^2} \frac{\left\langle r^{2L-2} \right\rangle}{\left\langle r^{L-1} \right\rangle^2} \tag{2.24}$$

which are useful in inelastic scattering data analysis.

For a L= 0 (monopole) transition, the mass operator is given by

$$Q_{000} = \sum_{i=1}^{A} r_i^2 Y_{00} \tag{2.25}$$

and the corresponding EWSR is obtained by inserting the above expression into Eq.(2.17) and Eq. (2.18)

$$S_{EW}^{00} = \frac{A\hbar^2}{2\pi m} \left\langle r^2 \right\rangle \tag{2.26}$$

where m is nucleon mass and $\langle r^2 \rangle$ is average over ground state density. If the excitation of a single state with excitation energy E_x exhausts EWSR, the sum rule limit dimensionless amplitude α_0 is obtained by inserting eq.(2.13) into Eq.(2.21) and following the same procedure as $L \geq 2$

$$\alpha_0^2 = \frac{2\pi\hbar^2}{mAE_x\langle r^2\rangle}. \tag{2.27}$$

2.1.4 Transition Density and EWSR for Isoscalar Dipole Mode

The collective formalism to describe isoscalar dipole excitations in electron scattering was first proposed by Deal *et al.* [58], and later extended to those excited with hadron scattering by Harakeh and Dieperink [59]. However, the transition density obtained by Harakeh and Dieperink is for only one magnetic substate. The total transition density should be multiplied by a factor of 3. One can see Ref. [59] for the detail about how to get the EWSR for ISGDR and corresponding sum rule limit transition density. The results are summarized below.

For isoscalar dipole excitation, the first order approximation, i.e., $Q_{010} = \sum_{i=1}^{A} r_i Y_{10}$, can only result in a translation of the center of mass. The second order approximation gives the ISGDR operator

$$Q_{010} = \sum_{i=1}^{A} r_i^3 Y_{10}, \tag{2.28}$$

and the corresponding EWSR is

$$S_{sw}^{01} = \frac{\hbar^2 A}{32m\pi}\left(11\langle r^4\rangle - \frac{25}{3}\langle r^2\rangle^2 - 10\varepsilon\langle r^2\rangle\right) \tag{2.29a}$$

where

$$\varepsilon = \frac{\hbar^2}{3mA}\left(\frac{4}{E_2} + \frac{5}{E_0}\right) \tag{2.29b}$$

where E_0 is the excitation energy of the ISGMR and E_2 is the excitation energy of the isoscalar quadruple resonance. If the isoscalar dipole EWSR is exhausted by one state, the transition density of this state is

$$g_1(r) = -\frac{\beta_1}{c}\left[3r^2\frac{d}{dr} + 10r - \frac{5}{3}\left\langle r^2\right\rangle\frac{d}{dr} + \varepsilon\left(r\frac{d^2}{dr^2} + 4\frac{d}{dr}\right)\right]\rho(r) \qquad (2.30a)$$

where

$$\beta_1^2 = \frac{6\pi\hbar^2}{mAE_x}\frac{c^2}{11\left\langle r^4\right\rangle - \frac{25}{3}\left\langle r^2\right\rangle^2 - 10\varepsilon\left\langle r^2\right\rangle} \qquad (2.30b)$$

and β_1 is the collective coupling parameter and c is the half density radius of the Fermi mass distribution. In all the above equations, ε is very small compared to $\left\langle r^2\right\rangle$, and for practical purpose the terms depending on ε could be ignored for A ≥ 20.

2.2 Scattering Theory

It was suggested long ago that inelastic scattering from nuclei would preferentially excite collective states [60, 61] which include discrete, low-lying states and high-lying giant resonance states. To extract the strength distribution for a giant resonance, it is necessary to calculate the differential cross section for inelastic scattering with the DWBA approximation. The details about how to solve the Schödinger equation with DWBA to get the differential cross section have been thoroughly discussed by Satchler in Ref. [54]. A general solution and some important assumptions are given in this section.

2.2.1 THE GENERAL SOLUTION OF THE SCATTERING PROBLEM

Let us consider a 2-body scattering system with a direct nuclear reaction $a + A \rightarrow b + B$. Following the notation in Ref. [54], a pair of nuclei **a** and **A** is called a partition and denoted as **α**, while another pair of nuclei **b** and **B** is denoted as partition **β**. The primed **α'** is used to denote different states of the same partition as **α**. The total Hamiltonian of the system for one partition can be expressed as

$$H = H_\alpha + K_\alpha + V_\alpha \tag{2-31}$$

where H_α is the internal Hamiltonian for the nuclei a and A, K_α is the kinetic energy of their relative motion, V_α is the mutual interaction potential. The total wavefunction can be obtained by solving the Schrödinger equation:

$$(E - H)\Psi = 0 \tag{2-32}$$

where Ψ may be expanded in terms of a complete set of internal states ψ_α, which is

$$\Psi = \sum_\alpha \xi_\alpha(\vec{r}_\alpha)\psi_\alpha(x_\alpha) \tag{2-33}$$

where the sum runs over all the internal states of partition α. Since the incident beam is in the α channel, the wavefunction Ψ contains incoming spherical waves only in the ground-state α channel but will have outgoing spherical waves in this and all other channels which are open at the incident energy. It is denoted as $\Psi_\alpha^{(+)}(\vec{k}_\alpha)$ in which (+) means that we choose outgoing wave and α means it arises from an incident wave in the α channel. It may also be expanded in terms of the states of partition **β**:

$$\Psi_\alpha^{(+)} = \sum_\beta \xi_\beta(\vec{r}_\beta)\psi_\beta(x_\beta) \tag{2-34}$$

where $\psi_\beta(x_\beta)$ is wavefunction of internal states in channel **β**, the function $\xi_\beta(\vec{r}_\beta)$ describes the relative motion in the channel β and is expressed as

$$\xi_\beta(\vec{r}_\beta) = (\psi_\beta \left| \Psi_\alpha^{(+)} \right.) \equiv \int \psi_\beta^*(x_\beta)\Psi_\alpha^{(+)} dx_\beta \,. \tag{2-35}$$

To satisfy boundary conditions, it must have the asymptotic expression

$$\xi_\beta(\vec{r}_\beta) \to e^{i\vec{k}_\alpha \cdot \vec{r}_\alpha}\delta_{\alpha\beta} + f_{\beta\alpha}(\hat{\vec{r}}_\beta, \vec{k}_\alpha)\frac{1}{\vec{r}_\beta}e^{ik_\beta r_\beta} \,. \tag{2-36}$$

Asymptotically, the relative momentum $\vec{k}_\beta$ has the same direction as $\vec{r}_\beta$, so

$$f_{\beta\alpha}(\hat{\vec{r}}_\beta, \vec{k}_\alpha) \to f_{\beta\alpha}(\hat{\vec{k}}_\beta, \vec{k}_\alpha)\,.$$

The differential cross section for the transition from channel α to channel β is defined as the ratio of $\left|J_o^\beta\right| r_\beta^2 d\Omega$ (the outgoing flux per unit time going into the small area subtending a small solid angle dΩ in channel β) over $\left|J_i^\alpha\right|$ (incident flux per unit time and unit area in channel α)

$$\frac{d\sigma_{\beta\alpha}}{d\Omega} d\Omega = \frac{\left|J_o^\beta\right| r_\beta^2 d\Omega}{\left|j_i^\alpha\right|}\ . \tag{2.37}$$

The probability flux is expressed as

$$\vec{J} = \frac{\hbar}{2mi}\int (\Phi^* \nabla_{\vec{r}} \Phi - \Phi \nabla_{\vec{r}} \Phi^*) dx \tag{2.38}$$

where Φ is the wavefunction of a certain channel. For an incident α channel, the wavefunction Φ can be expressed as

$$\Phi_i^\alpha = \psi_\alpha(x_a) e^{i\vec{k}_\alpha \cdot \vec{r}_\alpha}\,, \tag{2.39}$$

so

$$\left|\vec{J}_i^\alpha\right| = \frac{\hbar k_\alpha}{\mu_\alpha}, \quad where\ \mu_\alpha = \frac{m_a M_A}{m_a + M_A}. \tag{2.40}$$

For an outgoing β channel, the wavefunction can be expressed as

$$\Phi_o^\beta = \psi_\beta(x_\beta)\, f_{\beta\alpha}(\vec{k}_\beta, \vec{k}_\beta) \frac{e^{i\vec{k}_\beta \cdot \vec{r}_\beta}}{r_\beta}\,, \tag{2.41}$$

so

$$J_o^\beta = \frac{\hbar k_\beta}{\mu_\beta} \frac{\left| f_{\beta\alpha}(\vec{k}_\beta, \vec{k}_\alpha)\right|^2}{r_\beta^2},\ where\ \mu_\beta = \frac{m_b M_B}{m_b + M_B}. \tag{2.42}$$

From (2.37), (2.40) and (2.42), the differential cross section thus is obtained as

$$\frac{d\sigma_{\beta\alpha}}{d\Omega} = \frac{\mu_\alpha k_\beta}{\mu_\beta k_\alpha}\left| f_{\beta\alpha}(\vec{k}_\beta, \vec{k}_\alpha)\right|^2 . \tag{2.43}$$

We may obtain an exact expression for the scattering amplitude $f_{\beta\alpha}$ from Eq.(2.32) with an appropriate form of the Hamiltonian

$$(H - E)\Psi_\alpha^+ = (H_\beta + K_\beta + V_\beta - E)\Psi_\alpha^+ = 0 . \tag{2.44}$$

Multiplying Eq. (2.44) by $\psi_\beta^*(x_\beta)$ from left on both side of equation and integrating over x_β, we get

$$(E - \varepsilon_\beta - K_\beta)\xi_\beta(r_\beta) = (\psi_\beta \left| V_\beta \right| \Psi_\alpha^+) . \tag{2.45}$$

Using standard Green function techniques [62, 63] and considering the boundary condition, the relative wavefunction $\xi_\beta(\vec{r}_\beta)$ can be expressed as

$$\xi_\beta(\vec{r}_\beta) = e^{i\vec{k}_\alpha \cdot \vec{r}_\alpha}\delta_{\beta\alpha} - \left(\frac{\mu}{2\pi\hbar^2}\right)\int \frac{e^{ik_\beta\left|\vec{r}_\beta - \vec{r}_\beta^{'}\right|}}{\left|\vec{r}_\beta - \vec{r}_\beta^{'}\right|}\left(\psi_\beta \left| V_\beta \right| \Psi_\alpha^+\right) d\vec{r}_\beta^{'} . \tag{2.46}$$

When $r_\beta >> r_\beta^{'}$, we may have

$$\left|\vec{r}_\beta - \vec{r}_\beta^{'}\right| \approx r_\beta - \hat{\vec{r}}_\beta \cdot \vec{r}_\beta^{'} = r_\beta - \hat{\vec{k}}_\beta \cdot \vec{r}_\beta^{'} , \tag{2.47}$$

Comparing with the asymptotic expression (2.36), we then have

$$\begin{aligned} f_{\beta\alpha}(\vec{k}_\beta, \vec{k}_\alpha) &= -\left(\frac{\mu_\beta}{2\pi\hbar^2}\right)\left\langle e^{i\vec{k}_\beta \cdot \vec{r}_\beta^{'}}\psi_\beta \left| V_\beta \right| \Psi_\alpha^+ \right\rangle = -\left(\frac{\mu_\beta}{2\pi\hbar^2}\right) T_{\beta\alpha}\left(k_\beta, k_\alpha\right) \\ &= -\left(\frac{\mu_\beta}{2\pi\hbar^2}\right)\iint e^{-i\vec{k}_\beta \cdot \vec{r}_\beta^{'}}\psi_\beta^*(x_\beta) V_\beta(x_\beta, \vec{r}_\beta^{'})\Psi_\alpha^+ dx_\beta dr_\beta^{'} \end{aligned} . \tag{2.48}$$

2.2.2 Distorted Wave Born Approximation (DWBA)

Eq. (2.48) gives a formal expression of the transition amplitude, but it is still hard to evaluate $f_{\beta\alpha}(\vec{k}_\beta,\vec{k}_\alpha)$ since the details of the interaction and wavefunction are unknown. It is possible to introduce an auxiliary potential $U_\beta(r_\beta)$ which may be complex and is only dependent on r_β. Then (2.45) becomes

$$\left[E-\varepsilon_\beta-K_\beta-U_\beta(r_\beta)\right]\xi_\beta(\vec{r}_\beta)=\left(\psi_\beta\middle|W\middle|\Psi_\alpha^+\right) \tag{2.49}$$

where

$$W_\beta=V_\beta(\vec{r}_\beta,x_\beta)-U_\beta(x_\beta) \tag{2.50}$$

is called the residual interaction. The auxiliary potential can be chosen to include the main part of the average effects of V_β and the effects of the inhomogeneous term on the right side of (2.49) may be quite small and treated as a perturbation. With the expansion of Ψ_α^+ in (2-34), we have

$$\left(\psi_\beta\middle|W_\beta\middle|\Psi_\alpha^+\right)=\left(\psi_\beta\middle|W_\beta\middle|\psi_\beta\right)\xi_\beta(\vec{r}_\beta)+\sum_{\beta'\neq\beta}\left(\psi_\beta\middle|W_\beta\middle|\psi_{\beta'}\right)\xi_{\beta'}(\vec{r}_\beta), \tag{2.51}$$

in which the diagonal matrix element might be thought as the most important term, since it does not involve any internal rearrangement of the scattering system. The diagonal term can vanish if U_β is chosen as the average of V_β over the internal states ψ_β. To solve the equation (2.45), we need first neglect the inhomogeneous term on the right side of (2.45) and solve the equation

$$\left[E_\beta-K_\beta-U_\beta(r_\beta)\right]\chi_\beta^+(\vec{k}_\beta,\vec{r}_\beta)=0 \tag{2.52}$$

where χ_β^+ is known as the distorted wave and describes the elastic scattering of b on B due to potential U_β. Considering the boundary condition that χ_β^+ asymptotically has the form of incident plane wave plus outgoing spherical wave

$$\chi_\beta^+(\vec{k}_\beta,\vec{r}_\beta) \to e^{i\vec{k}_\beta\cdot\vec{r}_\beta} + f_\beta^{(0)}(\theta)\frac{1}{r_\beta}e^{ik_\beta r_\beta}\ , \tag{2.53}$$

we obtain the solution for the homogeneous equation (2.52) which is well-known from scattering theory

$$\chi_\beta^+(\vec{k}_\beta,\vec{r}_\beta) = \frac{4\pi}{k_\beta r_\beta}\sum_{\ell,m} i^\ell e^{i2\delta_\ell} f_\ell(k_\beta,r_\beta) Y_\ell^{m^*}(\hat{\vec{k}}_\beta) Y_\ell^m(\hat{\vec{r}}_\beta)\,, \tag{2.54}$$

where $f_l(k_\beta,r_\beta)$ is regular solution of the radial equation for (2.52) and δ_ℓ is a phase shift dependent on the specific form of potential U_β. A formal solution of (2.49) will be obtained with the application of Green function techniques, which asymptotically can be expressed as

$$\xi_\beta(\vec{r}_\beta) \to \left(e^{i\vec{k}_\alpha\cdot\vec{r}_\alpha} + f_\alpha^{(0)}(\theta)\frac{e^{ik_\alpha r_\alpha}}{r_\alpha}\right)\delta_{\alpha\beta} - \frac{\mu_\beta}{2\pi\hbar^2}\frac{e^{ik_\beta r_\beta}}{r_\beta}\int \chi_\beta^{-^*}(\vec{k}_\beta,\vec{r}_\beta')\left(\psi_\beta\middle|W\middle|\Psi_\alpha^+\right)d\vec{r}_\beta' \tag{2.55}$$

where $\chi_\beta^-(\vec{k}_\beta,\vec{r}_\beta)$ is the time-reverse of $\chi_\beta^+(\vec{k}_\beta,\vec{r}_\beta)$. The scattering amplitude $f_{\alpha\beta}(\vec{k}_\beta,\vec{k}_\alpha)$ then can be expressed as

$$f_{\beta\alpha}(\vec{k}_\beta,\vec{k}_\alpha) = f_\alpha^0(\theta)\delta_{\alpha\beta} - \frac{\mu_\beta}{2\pi\hbar^2}\int \chi_\beta^{-^*}(\vec{k}_\beta,\vec{r}_\beta')\left(\psi_\beta\middle|W\middle|\Psi_\alpha^+\right)d\vec{r}_\beta'\,. \tag{2.56}$$

Ψ_α^+ in the above equation can be estimated by the following procedures. Like the expansion in β partition, Ψ_α^+ can also be expanded in terms of internal states of α partition, as shown in (2.33). Assuming that the most important part of the total wave function is the elastic wave in the entrance channel, we have

$$\Psi_\alpha^+ \approx \xi_\alpha^+(\vec{k}_\alpha,\vec{r}_\alpha)\psi_\alpha\,. \tag{2.57}$$

By introducing a similar auxiliary potential U_α as mentioned above for β partition, the large part of the average effect of interaction V_α is included in U_α and the residual interaction $W_\alpha = V_\alpha - U_\alpha$ is treated as a perturbation. We can measure the elastic

scattering cross section experimentally and fit it to get the proper U_α. The U_α we get represents the average of V_α over the internal ground state of a channel, thus we have

$$(\psi_\alpha|W|\psi_\alpha) \approx 0, \quad \xi_\alpha(\vec{r}_\alpha) \approx \chi_\alpha^+(\vec{k}_\alpha, \vec{r}_\alpha)\,. \tag{2.58}$$

The above procedure to estimate Ψ_α^+ is called the distorted wave Born approximation (DWBA) and (2.56) can be transformed as

$$f_{\beta\alpha}^{DWBA}(\vec{k}_\beta, \vec{k}_\alpha) = f_\alpha^0(\theta)\delta_{\alpha\beta} - \frac{\mu_\beta}{2\pi\hbar^2}\int \chi_\beta^{-*}(\vec{k}_\beta, \vec{r}_\beta')\left(\psi_\beta|W|\psi_\alpha\chi_\alpha^+(\vec{k}_\alpha, \vec{r}_\alpha)\right)d\vec{r}_\beta'\,. \tag{2.59a}$$

For inelastic scattering, $a + A \to a + A^*$, α' is denoted as inelastic channel. Replacing β by α', we obtain the inelastic scattering amplitude

$$f_{\alpha'\alpha}^{DWBA}(\vec{k}_{\alpha'}, \vec{k}_\alpha) = -\frac{\mu_\alpha}{2\pi\hbar^2}\int \chi_{\alpha'}^{-*}(\vec{k}_{\alpha'}, \vec{r}')\left(\psi_{\alpha'}|W|\psi_\alpha\chi_\alpha^+(\vec{k}_\alpha, \vec{r})\right)d\vec{r}' \tag{2.59b}$$

and the differential cross section

$$\frac{d\sigma}{d\Omega}\Big|_{DWBA} = \frac{k_{\alpha'}}{k_\alpha}\left(\frac{\mu}{2\pi\hbar^2}\right)^2\left|\left\langle\chi_{\alpha'}^-\psi_{\alpha'}|V|\chi_\alpha^+\psi_\alpha\right\rangle\right|^2 = \frac{k_{\alpha'}}{k_\alpha}\left(\frac{\mu}{2\pi\hbar^2}\right)^2|T_{\alpha'\alpha}|^2\,. \tag{2.60}$$

2.3 Optical Model and Folding Potential

2.3.1 Optical Model and Woods-Saxon Potential

In the above section, we give a general solution of Schrödinger's equation for a two-nucleus scattering system and obtain an expression for the differential cross section for inelastic scattering with the distorted wave Born approximation. However, in order to compare with the experimental data, a proper effective potential U(**r**), like U_a mentioned in last section, must be constructed to include most of the average effect of the interaction of the system. The potential U(**r**) must be complex as the imaginary part is necessary to describe the loss of flux (absorption) into non-elastic channels. An analogy is light propagation in a semi-transparent medium which has a complex refractive index.

This is called the optical model of nuclear reactions. As indicated in the above section, the optical model is a model of the effective interaction, which is used to replace the complicated many-body problem posed by the interaction of two nuclei with the much simpler problem of two particles interacting through a potential U(**r**) which can be used in a one-body Schrödinger equation such that the asymptotic behavior of its solutions $\chi(\mathbf{r})$ describes their elastic scattering. The optical model plays an important role in the description of nuclear scattering. Not only does it provide an interpretation of elastic scattering in terms of a potential, it also provides the associated wavefunction for the relative motion of the colliding pair, which could be used to study the inelastic scattering.

Usually it is assumed [54], at least for light ion scattering, that the interior of the real potential ReU(r) is flat and attractive (negative) and, because of the short range of the nuclear interaction, rises quickly and monotonically to zero in the surface range. Several analytic forms [64, 65] have been used for ReU(r) to embody this assumption, among which, Woods-Saxon (W-S) form [66] is the most popular one. W-S form is based on a plausible assumption that the shape of the optical potential follows the shape of the target density. Since the Fermi distribution is often used to describe the density of nuclei, the W-S form potential is usually expressed as

$$\mathrm{Re}U(r) = -\frac{V}{1+e^{\frac{r-R_V}{a_V}}} \tag{2.61a}$$

where V, R_V and a_V are depth, half radius and surface diffuseness respectively. Sometimes a low power of Woods-Saxon shape, such as

$$\mathrm{Re}U(r) = -\frac{V}{\left(1+e^{\frac{r-R_V}{a_V}}\right)^2} \tag{2.61b}$$

is used for ReU(r) to get a satisfactory fit of elastic scattering.

The absorptive potential ImU(r), the imaginary part of U(r), is usually assumed to have a "volume" form or a "surface" form. The "volume" form is the same as (2.61a) with different depth, half radius and surface parameters, W, R_I and a_I. The surface absorption is usually taken to be proportional to the derivative of "volume" form, which can be expressed as

$$\mathrm{Im}U(r) = 4W_D \frac{e^{\frac{r-R_D}{a_D}}}{\left(1+e^{\frac{r-R_D}{a_D}}\right)} \tag{2.62}$$

where W_D, R_D,a_D are a set of parameters different with those for volume form. However, if both surface and volume terms are used for the imaginary potential, it is usually assumed $R_D = R_I$ and $a_D = a_I$. The origin of the imaginary potential, and associated relation to the real part, can be seen most transparently within the framework of Feshbach's reaction theory.

2.3.2 Folding Model

According to Feshbach's theory[67, 68], when an effective interaction or optical potential is used in the one-body Schrödinger equation to study elastic scattering, we may write

$$U_E = V_{00} + \Delta U_E = V_{00} + \lim_{\varepsilon\to 0} \sum_{\alpha\alpha'}{}' V_{0\alpha}\left(\frac{1}{E-H+i\varepsilon}\right)_{\alpha\alpha'} V_{\alpha'0} \tag{2.63}$$

where V is the real interaction between the two nuclei, while α means a pair of internal state labels i, j. The prime means the sum over all states α in which at least one nucleus is excited. The first term V_{00} is real and accounts for most of the real part of optical potential. It is simply expressed as folded potential

$$V_{00} = V_F \equiv (\phi_{p0}\phi_{t0}|V|\phi_{p0}\phi_{t0}) \ , \tag{2.64}$$

where 0 denote ground state, p means projectile and t means target, the round brackets mean integration over the internal coordinates of the two nuclei. It is generally assumed that the interaction V is a sum of local two-body potentials

$$V = \sum_{pt} v_{pt} \,. \tag{2.65}$$

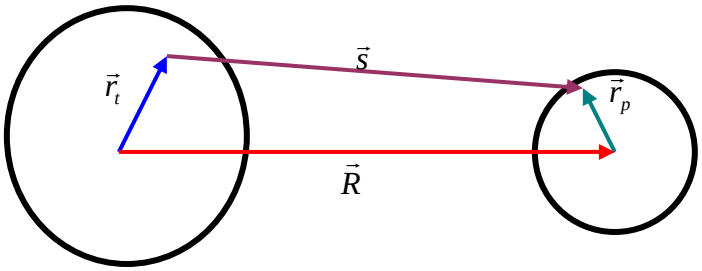

FIG. 2.1 Coordinates relation for folding calculation.

If spin and isospin are ignored for simplicity, the folded potential $V_{00}(R)$ may be written as a six-dimension integral

$$V_{00}(R) = V_F(R) = \int d\vec{r}_p \int d\vec{r}_t \rho_p(\vec{r}_p)\rho(\vec{r}_t) v_{pt}(\vec{s}, \rho_p, \rho_t) \tag{2.66}$$

where **p** represents projectile, **t** represents target and $\vec{s} = \vec{r}_p + \vec{R} - \vec{r}_t$ (see Fig. 2.1). The expression (2.66) involves a six-dimensional integral, which is hard to evaluate in position space. However, if we work in momentum space with Fourier transformation, the integral reduces to a product of several one-dimensional integrals and become quite simple to calculate (see appendix B of Ref. [69]). If v_{pt} is scalar, does not depend on the densities of the scattering pairs and the density distributions are spherically symmetric, the folded potential satisfies some simple relations. Such as, if we define the volume integral of the function f(r)

$$J(f) = 4\pi \int f(r) r^2 dr \,, \tag{2.67}$$

we have

$$J(V_F) = J(v_{pt})J(\rho_p)J(\rho_t) = A_p A_t J(v_{pt}). \tag{2.68}$$

If we define the mean-square radii of function f(r) as

$$\left\langle r^2 \right\rangle_f = \frac{\int f(r) 4\pi r^4 dr}{\int f(r) 4\pi r^2 dr} \tag{2.69}$$

We have

$$\left\langle r^2 \right\rangle_{V_F} = \left\langle r^2 \right\rangle_p + \left\langle r^2 \right\rangle_t + \left\langle r^2 \right\rangle_{v_{pt}}. \tag{2.70}$$

The Pauli principle is not considered when a folded potential is given as in (2.66). Although the individual internal wave functions in (4.16) are taken to be anti-symmetrized, the Pauli principle requires the total wavefunction of the scattering system also to be anti-symmetric under interchange of nucleons between the two nuclei. The interchange, which is called **knock-on exchange**, in practice, corresponds to the exchange of nucleon between target and projectile following their interaction. If this knock-on exchange effect is included, the two-body interaction will be replaced by

$$v_{pt} \to v_{pt}(1 - P_{pt}), \tag{2.71}$$

where P_{pt} is the operator that exchanges all coordinates of these two nucleons. And the folded potential is replaced by

$$V_{00} = V_F(r) = \left(\phi_{p0}\phi_{to} \left| \sum_{pt} v_{pt}\left(1 - P_{pt}\right) \right| \phi_{p0}\phi_{to} \right) = V_D + V_E, \tag{2.72}$$

where V_D is a direct term which is given in (2.66) and V_E is an exchange term .

The second term ΔU_E in (2.63) is complex and often referred to as the **dynamic polarization potential** (DPP). It arises from couplings to the nonelastic channels and represents transitions to open non-elastic channels. The imaginary part of DPP, known as absorptive potential, is the origin of the imaginary part of the optical potential. It is discussed in detail in [67] and references there. Since it is very difficult to calculate

DDP, a phenomenological W-S potential shape is still widely used to obtain the imaginary potential.

The real part of DPP comes from virtual excitation. Energetically closed channels can contribute to the real part of ΔU_E. It depends explicitly upon the energy and is non-local. However, its contribution to the real part of optical potential is usually much smaller than folded potential, the leading order approximation. Since DPP is not explicitly included in the real folded potential, a renormalization (N_R) of the real potential is used to take into account the DPP contribution. The overall success of folding models with N_R~1 indicates that in most cases the DPP contribution is very weak. But there is a very important exception where N_R deviates far from unity. For the scattering of weakly bound nuclei such as ^{6}Li, ^{7}Li and ^{8}Be [69], the elastic data require a large renormalization of the real folded potential with a factor around 0.6. The reason for the anomalous behavior of N_R is that the loosely bound nuclei are very easy to break up. Sakuragi *et al*. have thoroughly investigated the break up effect of the projectile using coupled discretized continuum channels (CDCC) techniques [70]. Their calculations showed that the dynamic polarization potential induced by the coupling with the breakup channels is a repulsive potential which cancels about 40% of the attractive folding potential in the nuclear surface region. The break up effect is the real origin of the renormalization factor N_R in the single channel double folding analysis of the elastic scattering of loosely bound nuclei. The fact that the N_R is almost constant around 0.5~0.6 implies that the break up effect is almost independent of bombarding energy and target nucleus.

2.3.3 The M3Y Effective Nucleon-Nucleon Interaction

There are several nucleon-nucleon effective interactions used in the folding model, (such as JLM interaction, S1Y interaction, M3Y interaction). The M3Y interaction is based on G-matrix elements of the Reid[71] or Paris [72] NN potential, for which we denote

them as M3Y-Reid [73] and M3Y-Paris interaction[74]. The spin- and isospin-independent central term of the M3Y interaction can be expressed as [67, 69]

$$\begin{aligned} M3Y-\mathrm{Re}id: v_{00}(r) &= \left[7999\frac{e^{-4r}}{4r}-2134\frac{e^{-2.5r}}{2.5r}\right]MeV \\ M3Y-Paris: v_{00}(r) &= \left[11062\frac{e^{-4r}}{4r}-2538\frac{e^{-2.5r}}{2.5r}\right]MeV \end{aligned} \tag{2.73}$$

There are two ways to estimate contributions from the knock-on exchange effect. One way is to use the zero-range pseudo-potential approximation, in which the knock-on exchange effect is represented by a δ function and the strength $J_{00}(E)$ [75] is determined empirically by comparing cross sections for protons scattering from various targets, and at various energies up to 80 MeV. With the different versions of the interaction, $J_{00}(E)$ can be expressed respectively as [67, 69]

$$\begin{aligned} M3Y-\mathrm{Re}id: \hat{J}_{00}(E) &\approx -276[1-0.005(E/A)]MeVfm^3 \\ M3Y-Paris: \hat{J}_{00}(E) &\approx -590[1-0.002(E/A)]\,MeVfm^3 \end{aligned} \tag{2.74}$$

where E/A is the bombarding energy per projectile nucleon. Another way is to use the finite range approximation, in which the knock-on exchange effect is expressed as a sum of three Yukawa terms which represent the attractive, long-range one pion exchange, medium range multiple-pion exchange and a short range interaction. The knock-on exchange can be expressed as

$$\begin{aligned} M3Y-\mathrm{Re}id: \hat{v}_{00}(r) &= [4631\frac{e^{-4r}}{4r}-1787\frac{e^{-2.5r}}{2.5r}-7.847\frac{e^{-0.7072r}}{0.7072r}]MeV \\ M3Y-Paris: \hat{v}_{00}(r) &= [-1524\frac{e^{-4r}}{4r}-518.8\frac{e^{-2.5r}}{2.5}-7.847\frac{e^{-0.7072r}}{0.7072r}]MeV \end{aligned} \tag{2.75}$$

Although the M3Y-Paris interaction has a much more attractive exchange term than the M3Y-Reid interaction, the sum of the direct term and exchange term will give similar folded potentials. This emphasizes the importance of including the knock-on exchange effect when calculating the folded potential.

A density dependent M3Y (DDM3Y) effective N-N interaction has been described and discussed in detail by Dao T. Khoa [76-78]. Generally the density dependent N-N interaction is assumed to have the separable form,

$$v_{D(EX)}(\rho, E, s) = g(E)F(\rho)v_{D(EX)}(s) \tag{2.76a}$$

where *g(E)* is a energy dependent factor and F(ρ) is the density dependent function. The *g(E)* is a linear function of the bombarding energy E and, for the M3Y-Paris interaction,

$$g(E) = 1 - 0.003E/a \tag{2.76b}$$

where a is the mass of projectile. The original DDM3Y interaction [79, 80] assumed an exponential dependence on the density

$$F(\rho) = C\left[1 + \alpha \exp(-\beta\rho)\right]. \tag{2.77}$$

A flexible power-law density dependence was also introduced in [76, 81]

$$F(\rho) = C(1 - \alpha\rho^{\beta}) \tag{2.78}$$

and the corresponding interaction is denoted as BDM3Y interaction. The more general formula [77, 78] which is a hybrid of the DDM3Y and BDM3Y forms can be expressed as

$$F(\rho) = C\left[1 + \alpha \exp(-\beta\rho) - \gamma\rho\right] \tag{2.79}$$

and the corresponding density dependent interaction is denoted as CDM3Y interaction.

2.3.4 Folding Procedure

The procedures used to obtain the folded potential and the details of the folding integral are described and discussed in Ref. [78]. They are summarized below.

Assuming the interaction V is independent of spin and isospin, the direct term of the folding potential can be expressed in terms of the one-body spatial densities,

$$V^{(D)}_{a'A',aA}(E,\vec{R}) = \int \rho_{a'a}(\vec{r}_a)\rho_{A'A}(\vec{r}_A)v_D(\rho,E,s)d\vec{r}_a d\vec{r}_A, \tag{2.80}$$

where $\rho_{aa'}(\vec{r}_a), \rho_{AA'}(\vec{r}_A)$ are one body mixed densities for the projectile and target respectively. For elastic scattering, $\rho_{aa'}(\vec{r}_a)$ and $\rho_{AA'}(\vec{r}_A)$ are replaced by ρ_p and ρ_t, ground state densities for projectile and target. The exact expression for the exchange term cannot be expressed simply since it is non-local. However, if one treats the relative motion locally as a plane wave, one can get a local approximation for the exchange term

$$V^{(EX)}_{a'A',aA}(E,\vec{R}) = \int \rho_{a'a}\left(\vec{r}_a,\vec{r}_a+\vec{s}\right)\rho_{A'A}(\vec{r}_A,\vec{r}_A-\vec{s})v_{EX}(\rho,E,s)\times\exp\left(\frac{i\vec{K}(\vec{R})\vec{s}}{M_\alpha}\right)d\vec{r}_a d\vec{r}_A \tag{2.81}$$

where $\vec{K}(\vec{R})$ is the local momentum of relative motion and

$$K^2(\vec{R}) = \frac{2\mu_\alpha}{\hbar^2}\left[E_{c.m.} - V\left(E,\vec{R}\right) - V_C(\vec{R})\right] \tag{2.82}$$

where $\mu_\alpha = mM_\alpha$ is the reduced mass, m is the bare nucleon mass and $M_\alpha = \frac{a\,A}{a+A}$ is the reduced mass number, and $E_{c.m.}$ is the center of mass Energy. $V\left(E,\vec{R}\right) = V_D(E,\vec{R}) + V_{EX}(E,\vec{R})$ and $V_C(\vec{R})$ are the total nuclear and Coulomb potentials respectively. It is obvious that (2.81) has a self-consistancy problem because the relative momentum *K* is dependent on the total nuclear potential. However, by using a realistic approximation for the mixed density matrix [82, 83] and after a transformation [78], one obtains a self-consistent and local exchange potential

$$\begin{aligned} V^{(EX)}_{a'A',aA}(E_\alpha,\vec{R}) = 4\pi g(E_\alpha)\int_0^\infty v_{EX}(s)\,j_0(K(R)s/M_\alpha)s^2 ds \int f_a(\vec{r},s) \\ \times f_A(\vec{r}-\vec{R},s)F\left(\rho_{a'a}(\vec{r}) + \rho_{A'A}(\vec{r}-\vec{R})\right)d\vec{r} \end{aligned} \tag{2.83a}$$

where

$$f_{a(A)}(\vec{r},s) = \rho_{a'a(A'A)}(\vec{r})\,\hat{j}_1(k_{Fa(A)}(r)s) \tag{2.83b}$$

in which $k_{Fa(A)}(r)$ is local Fermi momentum [83] and

$$\hat{j}_1(x) = 3j_1(x)/x = 3(\sin x - x\cos x)/x^2 . \tag{2.83c}$$

With $\rho_{aa'}(\vec{r}_a)$ and $\rho_{AA'}(\vec{r}_A)$ replaced by ρ_p and ρ_t, one can get the exchange term for elastic scattering.

In the calculation of the direct term, the overlapping density ρ in F(ρ) is estimated as the sum of the ground densities of target and projectile

$$\rho = \rho_t(\vec{r}_t) + \rho_p(\vec{r}_p), \tag{2.84}$$

while in evaluating the exchange term of the folded potential, the overlapping density is assumed as the sum of the projectile and target densities at the midpoint between the two nucleons being exchanged

$$\rho = \rho_t(\vec{r}_t + \frac{\vec{s}}{2}) + \rho_p(\vec{r}_p + \frac{\vec{s}}{2}). \tag{2.85}$$

2.3.5 Folding with JLM Effective Interaction

The JLM interaction is a complex, energy and density dependent G-matrix interaction which is obtained from the Reid soft-core NN potential with the Brueckner-Hartree-Fock (BHF) approximation [84]. Unlike the M3Y interaction, the JLM interaction can simultaneously provide both real and imaginary parts of the optical potential. Starting from the potential for a nucleon of energy E traversing nuclear matter of density ρ

$$U_{NM}(\rho, E) = V(\rho, E) + iW(\rho, E) \tag{2.86}$$

where V and W are real and imaginary parts (For the expressions of V and W, see Ref. [85]), the density and energy dependent JLM NN effective interaction for heavy ion scattering can be obtained as

$$v(\rho, E) = \frac{V(\rho, E) + iW(\rho, E)}{\rho}. \tag{2.87}$$

The potential for heavy ion collisions thus is given by the folding integral

$$V(R) = \int \rho_T(r_T)\rho_P(r_P)v(\rho,E)\delta(\vec{s})\,d\vec{r}_T\,d\vec{r}_P \tag{2.88}$$

where $\vec{s} = \vec{r}_T + \vec{R} - \vec{r}_P$, ρ_T is the density of the target and ρ_P is the density of the projectile. The local density ρ is estimated with two different approximations. In the first approximation, the local density is estimated as geometric average of the projectile and target density

$$\rho(\vec{s}) = \left[\rho_T(\vec{r}_T + \frac{\vec{s}}{2})\rho_P(\vec{r}_P - \frac{\vec{s}}{2})\right]^{1/2} \tag{2.89}$$

while in the second approximation, the local density is given as arithmetic average of the two densities

$$\rho(\vec{s}) = \frac{1}{2}\left[\rho_T(\vec{r}_T + \frac{\vec{s}}{2}) + \rho_P(\vec{r}_P - \frac{\vec{s}}{2})\right]. \tag{2.90}$$

When the folded potential obtained with the JLM interaction is used to analyze the elastic scattering data, the quality of the fit can be substantially improved by replacing the δ function in (2.82) by a finite range smearing function [84, 86]

$$g(\vec{s}) = \left(\frac{1}{t\sqrt{\pi}}\right)^3 e^{-s^2/t^2} \tag{2.91}$$

where t is the range parameter. With the smearing function included, the rms radii of the folded potential are increased, but the volume integrals do not change since the smearing functions are normalized to 1. There are substantial renormalization factors required for both real and imaginary parts of these folded potentials when they are used to analyze elastic scattering involving loosely bound nuclei, such as ^{6}Li and ^{7}Li

$$U(r) = N_V V_{fold}(r) + iN_W W_{fold}(r)\,. \tag{2.92}$$

As we described previously, breakup is responsible for these renormalizations.

2.4 Transition Potential

To study giant resonances via inelastic scattering, a transition potential is required to calculate the differential cross-section for inelastic scattering. Transition potentials for the deformed potential model and the double folding model are described in this section.

2.4.1 Deformed Optical Potential Model

The deformed potential model has been used for the analysis of inelastic scattering for many years. The model is based on the simple and plausible assumption that the shape of optical potential for the scattering pairs follows the shape of the density distribution of the target and is either statically deformed or undergoing shape oscillations in the same way [54]. With this assumption, the transition potential can be obtained immediately by analogy with the transition density introduced in section 2.1. For $L \geq 2$, the transition potential is given by [87, 88]

$$G_L(r) = -\delta_L \frac{dU(r)}{dr}, \tag{2.93}$$

where the sum rule limit deformation length is given by (2.24). For $L = 0$, the transition potential is given by[89]

$$G_0(r) = -\alpha_0 \left[3U(r) + r\frac{dU(r)}{dr} \right], \tag{2.94}$$

where the sum rule limit deformation parameter α_0 is given by (2.26). For $L = 1$, the transition potential is given by [59]

$$G_1(r) = -\frac{\beta_1}{R}\left[3r^2\frac{d}{dr} + 10r - \frac{5}{3}\langle r^2 \rangle \frac{d}{dr} + \varepsilon(r\frac{d^2}{dr^2} + 4\frac{d}{dr}) \right] U(r) \tag{2.95}$$

where ε is given by (2.29b) and β_1 is given by (2.30b).

The advantage of the deformed potential model is its simplicity, however, the price paid for this simplicity is that the unambiguous connection between the density deformation and the potential deformation is no longer available [54].

2.4.2 Folded Potential

Following the formalism of the generalized folding model using the realistic density dependent nucleon-nucleon interaction [78] mentioned in above section, the nuclear density for nucleus a in (2.80) and (2.81) can be decomposed into a multipole expansion

$$\rho_{a'a}(r) = \sum_{\lambda_a \mu_a} \left\langle J_a M_a \lambda_a M_a \middle| J_{a'} M_{a'} \right\rangle C_{\lambda_a} \rho_{\lambda_a}^{(aa')}(r) \left[i^{\lambda_a} Y_{\lambda_a \mu_a}(\hat{\vec{r}}) \right]^* \tag{2.96}$$

where $C_0 = \sqrt{4\pi}$ and $C_\lambda = 1$ for $\lambda \neq 0$. A similar expression can be obtained for nucleus A. For a single excitation of the target nucleus A, the corresponding nuclear matrix element can be expressed as

$$\left\langle \alpha'(aA') \middle| V \middle| \alpha(aA) \right\rangle = \sum_{\lambda\mu} C_\lambda \left\langle J_A M_A \lambda\mu \middle| J_{A'} M_{A'} \right\rangle V_\lambda(E_\alpha, R) \left[i^\lambda Y_{\lambda\mu}(\hat{\vec{R}}) \right]^* \tag{2.97}$$

where α means incident scattering channel, α' means inelastic scattering channel, A' means single excitation of the target nucleus and

$$V_\lambda(E_\alpha, R) = V_\lambda^{(D)}(E_a, R) + V_\lambda^{(EX)}(E_\alpha, R), \tag{2.98}$$

where $V_\lambda^{(D)}(E_\alpha, R)$ and $V_\lambda^{(EX)}(E_\alpha, R)$ are direct term and exchange term respectively. To evaluate the transition potential, there are two options of the density dependence considered to include the medium correction when density dependent NN interaction is used[78, 90]: i) static treatment of the density dependence (SDD) in which only the ground state densities are included in the folding procedure, i.e.

$$v_{D(EX)}(\rho, s) = F(\rho_0^a + \rho_0^A) v_{D(EX)}(s); \tag{2.99}$$

ii) more consistent dynamic treatment of the density dependence (CDD) in which the effect of density changing due to the excitation is also included, i.e.

$$\hat{v}_{D(EX)} = \left[F(\rho_0^a + \rho_0^A) + \frac{\partial F(\rho_0^a + \rho_0^A)}{\partial \rho_0^A} \rho_0^A \right] v_{D(EX)}(s) . \qquad (2.100)$$

According to Farid and Satchler[90], the difference between the two options resulted in 20% or less difference in peak cross sections in the case of α scattering to small angles, particularly relevant to giant resonance studies. The transition potential can be obtained with above prescriptions and by replacing $\rho_{aa'}$ with ρ_p and $\rho_{AA'}$ with ρ_t^λ in (2.80) and (2.81). ρ_t^λ is the transition density of the target from ground state to excited state with L = λ. The transition density used for giant resonance study corresponding to 100% EWSR for L = 0 was given by (2.13) with deformation parameter given by (2.27), while that for L = 1 was given by (2.30a) with deformation parameter given by (2.30b) and those for L ≥ 2 were given by (2.6) with deformation length given by (2.24) in section 2.1.

2.5 Computer Codes

There exist several computer codes to carry out the calculations described above. The studies of giant resonances with α particles have used **PTOLEMY** [91] for the DWBA calculations and **DOLFIN** [92] to calculate single folding optical and transition potentials for input to PTOLEMY. For the loosely bound ^{6}Li, single folding is not adequate, and there are several codes available for calculating doubled folded potentials with different NN effective interactions. We have used **DFPD4**[93], **CHEN2**[94] and **OPTJLM1**[95] each of which is described briefly below.

In addition to **PTOLEMY** the code **ECIS**[96, 97] is also commonly used for DWBA calculations. A series of calculations performed with both **DPDF4_ECIS** and with **DOLFIN_PTOLEMY** were carried out to test the codes and our ability to use them.

2.5.1 **DFPD4**----Density Dependent Double Folding Calculation

DFPD4 [78, 93] is an unpublished FORTRAN code written by Dr. Dao Tien Khoa used to calculate potentials with the folding model for both heavy ion (HI) and light ion elastic and inelastic scattering. The nuclear potential was obtained by folding the density dependent M3Y NN effective interaction over the ground density of target and projectile while the transition potential was obtained by folding over the transition density of the target. With knock-on exchange included, the effective NN interaction has two terms and so the corresponding folded potential also has a direct term and an exchange term. A sample input file for DFPD4 is given in Fig. 4.1 to show the parameters used for the folding calculation.

```
1
 LI6+28Si, ELAB=240 MEV,(CDM3Y5 K=241) COSMA dens. for 6Li, Fermi dens. for
28Si
    1    5    1    2    3    1    1    2
240.    3.      6.01512 14.      28.0   0.0     3.154   0.00     1.0
0.05    20.     0.1     20.     0.02    18.     0.0026  0.
0.2728    3.7367    1.8294    -3.0
4.332     11061.625 -1524.25  0.
2.7075    -2537.5   -518.75   0.
0.765913  0.000187  -7.847438
0.1       0.0       0.0       0
         -5 3.      0.0       17.
2.0       1.0       1.43121   1.91136   1.0       0.0
          5 3.      0.0       17.
2.0       1.0       1.43121   1.91136   1.0       0.0
0.1       0.0       0.0       0
          5 3.      0.0       17.
2.0       1.0       1.55      2.07      1.0       0.0
0.1       0.0       0.0       0
          2 27.977  0.0       17.
0.2125    2.9132    0.4829              Satchler
0.1       0.0       0.0       0
          2 27.977  1.38      17.
0.1673    2.9132    0.4829
0.1       0.0       0.0       0
          2 14.     1.38      17.
0.0837    3.155     0.523
```

1 2 3 4 5 6 7 8

FIG. 2.2 A sample input file of **DFPD4**. The number 1-8 on the left side represent different parameters sets explained in the text.

As shown in Fig. 2.2, the parameters for the scattering system, the NN effective interaction, Coulomb potential, target and projectile density profiles are given in different parameter sets labeled from 1-8. **Parameter set 1** includes the header of the

scattering system, output and display control, density dependency choice, J^{π} for excited states of the target nucleus, incident (lab.) energy, charges and masses of projectile and target, charge radii of the projectile and target etc. **Parameter set 2** lists the parameters C, α, β, γ of the density dependent function F(ρ) [see Eq. (2.79)] which are shown in Table 2.1 [77]. The overlap density ρ is defined as the sum of the projectile density ρ_P and target densities ρ_T

$$\rho = \rho_T + \rho_P \,. \tag{2.101}$$

Parameter set 3 gives the parameters for M3Y NN effective interaction. **Parameter set 4** and **5** are the profiles for projectile of mass density and charge density respectively. **Parameter set 6**, **7**, **8** are profiles respectively for mass density, total transition density and proton transition density of the target. A very important parameter is ***delt*** in **set 6, 7, 8** used to give the deformation parameter and control which model is used to get the transition density for giant resonance.

Table 2.1 Parameters of different density dependent functions F(ρ) of the M3Y-Paris interaction. Values of the nuclear incompressibility K were obtained from the Hartree-Fork Calculation of nuclear matter. (originally from the Table I of the Ref. [77].)

ρ dependency type	C	α	β (fm3)	γ (fm3)	K (MeV)
DDM3Y1	0.2963	3.7231	3.7384	0.0	176
CDM3Y1	0.3429	3.0232	3.5512	0.5	188
CDM3Y2	0.3346	3.0357	3.0685	1.0	204
CDM3Y3	0.2985	3.4528	2.6388	1.5	217
CDM3Y4	0.3052	3.2998	2.3180	2.0	228
CDM3Y5	0.2728	3.7367	1.8294	3.0	241
CDM3Y6	0.2658	3.8033	1.4099	4.0	252
BDM3Y1	1.2521	0.0	0.0	1.7452	270

DFPD4 can be used to calculate the transition potential either for inelastic scattering to low-lying states or for giant resonances of the target depending on parameter ***ENX*** value chosen in parameter set 1. With parameter ***ENX*** = 0, **DFPD4** calculate the transition

potential for low-lying state while, with ***ENX*** = excitation energy, **DFPD4** calculates transition potential for giant resonance. For giant resonances with multipolarity $L \geq 2$, if the parameter ***delt*** > 0, the Bohr-Mottelson model is used to calculate transition density, while if ***delt*** < 0, the Tassie Model is used to calculate transition density. For giant resonances with L = 0, the scaling model is used to calculate the transition density if one chooses ***delt*** > 0. For an isoscalar giant resonance with L = 1, Harakeh *et al.* 's expression [59] of transition density is used when one chooses ***delt*** < 0. In all the transition potential calculations for giant resonances, the deformation parameter ***delt*** was set equal to the EWSR limit and was calculated externally.

DFPD4 can also calculate the Coulomb part of the optical and transition potentials. The Coulomb transition potential is calculated the same as transitional nuclear potential by the folding model in which the proton transition density of target is used. According to Khoa *et al*. [78], the Coulomb potential obtained assuming that both the projectile and the target have uniform charge distributions is adequate to estimate the coulomb interaction. So an analytic expression can be used to calculate the Coulomb potential rather than using the folding model. If the uniform charge radii for projectile and target are R_P and R_T, the coulomb potential V_c can be expressed as [98]:

$$V_c = \begin{cases} \dfrac{Z_p Z_T}{2R_T^3}\left[3\left(R_T^2 - R_p^2/5\right) - r^2\right], & r \le R_T - R_P \\ \dfrac{Z_p Z_T e^2}{R_T^3 R_p^3}\left[\begin{array}{l} \dfrac{1}{32}\left(R_T - R_p\right)^4\left(R_T^2 + 4R_T R_p + R_p^2\right)\dfrac{1}{r} - \dfrac{3}{20}\left(R_T + R_P\right)^3\left(R_T^2 - 3R_T R_p + R_p^2\right) + \\ \dfrac{9}{32}\left(R_T^2 - R_P^2\right)^2 - \dfrac{1}{4}\left(R_T^3 + R_P^3\right)r^2 + \dfrac{3}{32}\left(R_T^2 + R_p^2\right)r^3 - \dfrac{1}{162}r^5 \end{array}\right], & R_T - R_p \le r \le R_T + R_p \\ \dfrac{Z_T Z_p e^2}{r}, & R_T + R_p \le r. \end{cases} \tag{2.102}$$

2.5.2 **CHEN2**----Density Independent Double Folding Model Calculation

CHEN2 is an unpublished FORTRAN code [94] which does a density independent double folding calculation. The M3Y-Reid NN effective interaction is used in the code and the exchange term is evaluated with a delta function (see Eq. 2.74). Fermi

distributions obtained from the droplet model were used for the target and projectile density in the folding calculation. The folding integral was evaluated with a method which takes advantage of analytical properties of folding involving a δ-function [99]. Folded transition potentials for $\ell = 2,3,4$ can be evaluated with this code. A sample input file for 240 MeV ^{6}Li scattering on ^{116}Sn is shown in Fig. 2.3.

```
240.0 6.0                    !Incident energy
0.1 301                      !h,nmax for r integration
0.1   30                     !R_min,R_max
0.05 201                !hq,nmaxq for q integration
0.02 100                !hx,mmax  for angle integration
0                       !itaylor (0=exact multiplole expansion)
0. 0. 0. 3. 6.               !bb2,bb3,bb4 zproj,aproj
0.1385 0.180 0. 50. 116.          !bb2,bb3,bb4 ztarg,atarg
1.                      !renorm
3                       !nr_lambda0 number of multipoles
0 0 0
0 2 2
0 3 3
```

FIG. 2.3 A sample input file for **CHEN2** to calculate the folding potential for ^{6}Li elastic scattering on ^{116}Sn and inelastic scattering to low-lying 2^{+} and 3^{-} states of ^{116}Sn.

2.5.3 **OPTJLM1**----Double Folding Calculation With the JLM Interaction

OPTJLM1 is a FORTRAN code that does density dependent double folding calculations with the JLM effective NN interaction, calculates differential cross sections and fits elastic scattering data with the optical model [95]. The folding procedure with the JLM interaction has been described above. The densities of the projectile and target are obtained in a standard spherical Hartree-Fork calculation using the energy density function of Beiner and Lombard [99, 100]. The folding calculation in OPTJLM1 requires that the files describing input densities of the projectile and target should have a

certain format. Each density file gives the proton density, first derivative and second derivative of proton density, then the same for neutron. There are two options for the density dependence in the folding calculation, one can choose the overlap density ρ either as shown in Eq. (2.101), or

$$\rho = \sqrt{\rho_P \rho_T} \ . \tag{2.103}$$

One can read text file README.TXT [95] For the details of calculation.

2.5.4 **ECIS**----Equations Couplées en Itérations Séquentielles

ECIS is a FORTRAN code for DWBA calculations which can do coupled channel calculations with the method called Sequential Iteration for Coupled Equation [96, 97]. There are various versions of **ECIS** and **ECIS97** was used in this work**.** For analysis of ^{6}Li scattering, one can fit elastic scattering data to obtain optical parameters and calculate the differential cross-section for inelastic scattering to different states of the target.

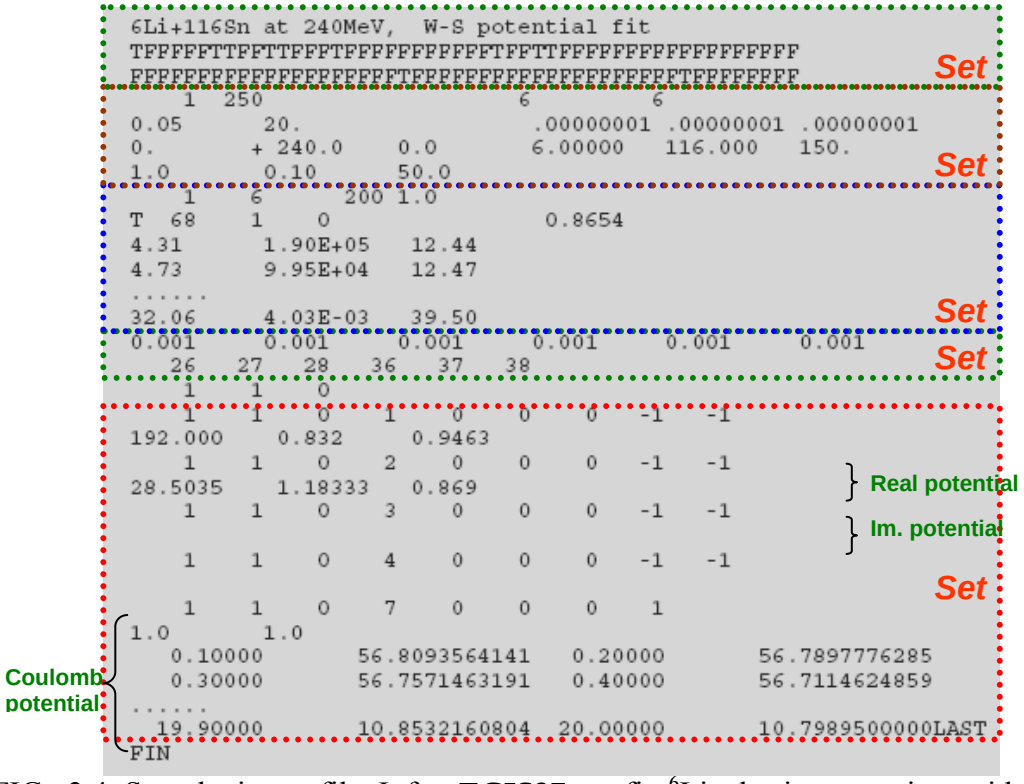

FIG. 2.4 Sample input file I for **ECIS97** to fit ^{6}Li elastic scattering with W-S potential model.

Fig. 2.4 shows a sample input file I for **ECIS97** to fit ^{6}Li elastic scattering with the W-S potential model. In order to understand it better, the input file is divided into several parameter sets, each set fulfilling mainly one function of the calculation. ***Set 1*** includes header describing the scattering system, and 100 logical parameters which are used to specify models used in the calculation, details of the interaction and integration, control parameters searching, displaying and printing. ***Set 2*** includes the incident energy, the masses and product of charges of projectile and target, spin, parities and excitation energies of all the nuclear states considered in the calculation, etc. For the sample input file considered here, only one state is described in ***Set 2***. ***Set 3*** gives the number of the input data sets, number of the fitted parameters, and gives experimental data for each data set. ***Set 4*** gives the fitted parameter ID and searching accuracy. ***Set 5*** specifies the potential parameters for the real part, the imaginary part and the Coulomb potential. For optical potential represented by a W-S shape, both the real part and the imaginary part

have three parameters, i.e. depth $V_{R(I)}$, half radius $r_{r0(I0)}$, and the diffusion parameter $a_{r(I)}$. There are two ways to evaluate the Coulomb potential. In the first way, three parameters are input and the Coulomb potential is calculated by **ECIS97**. The first parameter is the product of Z_T and Z_P, the charges of the target and projectile. The second parameter is the charge radius parameter R_{c0}. With heavy-ion definition of reduced radii, the Coulomb radius can be expressed as:

$$R_c = R_{c0}(A_T^{1/3} + A_P^{1/3}) \tag{2.104}$$

where A_T and A_P are masses of target and projectile respectively. The third parameter is the diffusion parameter a_c for charge distribution. With the assumption of uniform charge distribution, a_c=0 and the Coulomb potential can be expressed as:

$$V_C(r) = \begin{cases} \frac{1}{2} Ze^2(3-(r/R_C)^2)/R_C, & for\ \ r < R_C \\ Ze^2/r, & for\quad r > R_C. \end{cases} \tag{2.105}$$

The Coulomb potential can also be calculated externally by another code, such as **DFPD4**, and then input to **ECIS97** for further calculation as shown in Fig. 2.4 for sample input file I.

A sample input file II of **ECIS97** for the calculation of the differential cross section for ^{6}Li elastic scattering and inelastic scattering to the low-lying 2^+ state with the double folding model is shown in Fig. 2.5. Compared to the input file I shown in Fig. 2.4, logical parameters in ***set 1*** are the same. ***Set 2*** and ***set 3*** are almost the same as in Fig. 2.4 except that parameters for two states, instead of one state, are specified in ***set 2*** and two sets of experiment data are input in ***set 3***. Since no fit is required in this input file, no parameter set for parameter ID and parameter searching is shown in the input file. ***Set 4*** gives the table of form factor ID and multipolarity for each form factor. ***Set 5*** gives the potential parameters for the elastic scattering channel in which the real part and Coulomb potential are obtained from another code, such as **DFPD4**, while the imaginary part of the potential is calculated by ECIS itself with the W-S potential model. ***Set 6***

gives the form factor for inelastic scattering to low-lying 2^+ state. The format of ***set 6*** is almost the same as that of ***set 5***. For example, when the external form factor is input as a subset, such as for real optical and transition potential, the first row of the subset tells the code which part of the potential is specified in the following section, the second row of the subset gives the strength factor for the potential and scaling factor for the radius, and the rest of the subset gives the potential in term of radius and corresponding potential value. The W-S potential shape or deformed W-S potential model is used for imaginary potential. The subset for this part includes two rows in which the first row tells the code which part is specified in the following section and the second row gives three W-S parameters. However there are some differences between ***set 5*** and ***6***. The strength factors in ***set 6*** for both real and Coulomb transition potential obtained from external code should be multiplied with an additional factor $\sqrt{1/4\pi}$. For imaginary transition potential with $L \geq 2$ in ***set 6***, the first of the three W-S parameters is expressed as:

$$U_i^{\ell} = \frac{V_i \delta^{\ell}}{r_{i0} A_T^{1/3}} \tag{2.106}$$

where V_i is the depth of the imaginary optical potential and δ^{ℓ} is the deformation length. The second and third W-S parameters are the same as in ***set 5***.

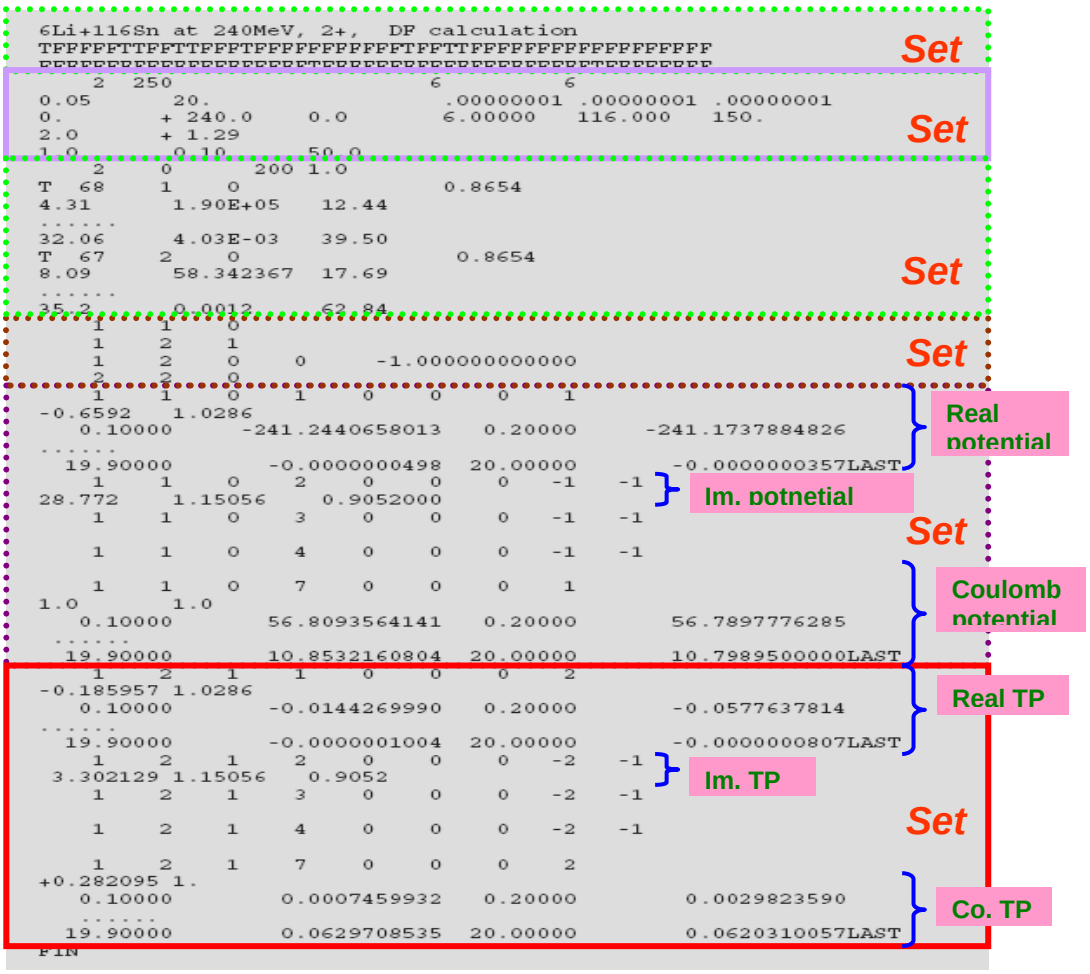

FIG. 2.5 Sample input file II for **ECIS97** to calculate the differential cross section for ^{6}Li elastic scattering and inelastic scattering to the low-lying 2^{+} state of ^{116}Sn with the double folding model. Real TP stands for real transition potential, Im. TP stands for imaginary transition potential. Co. TP stands for Coulomb transition potential.

2.5.5 Testing **DFPD4** and **ECIS** with the 240 MeV α + ^{144}Sm Scattering System

.As a test to verify that our calculations are consistent with a known case, calculations were carried out for the 240 MeV α + ^{144}Sm system (which had been previously studied [49]) using both **DOLFIN** (single folding) and **DFPD4** (double folding) to calculate potentials which were then read into **ECIS** to calculate cross sections. The results are then compared to those obtained with **DOLFIN** and **PTOLEMY**.

In addition to a general check of our application of these codes, the following questions are expected to be answered with the test:

1. Given the same nuclear potential parameters, do **ECIS** and **PTOLEMY** give the same differential cross sections?

2. Since sometime a normalization constant was introduced in folding procedure in L=0 case to compensate for the fact that $Y_0^0 = (4\pi)^{-1/2}$ [54], is the factor of $(4\pi)^{-1/2}$ required to be multiplied to the strength factor of the transition potential obtained from **DFPD4** for ISGMR to do correct calculation?

3. Since **DFPD4** also calculates the Coulomb part of the optical and transition potential, does **it** calculate the coulomb transition potential the same way as **PTOLEMY**? If not, how does it affect the calculation of cross section?

The real optical potential and nuclear transitional potential for ISGMR with the excitation energy E_x=12.5 MeV was calculated with **DOLFIN** and then input to **ECIS** and **PTOLEMY** respectively to calculate the differential cross section (The imaginary potentials were obtained with a deformed potential model calculation as shown in Eq. (2.94)). The calculations show that **PTOLEMY** and **ECIS** give almost the same results (There are 4% difference in maximum differential cross section, see Table 2.2 and Fig. 2.6) if the strength factor for the transition potential is multiplied by $1/(4\pi)^{1/2}$ in the

ECIS input file. The calculation also verified that the input real and imaginary potential should have same polarity in the same range, otherwise the angular distribution will have a phase shift compared to **PTOLEMY** calculation (see purple curve in Fig. 2.6). The same conclusion was obtained for the ISGDR case.

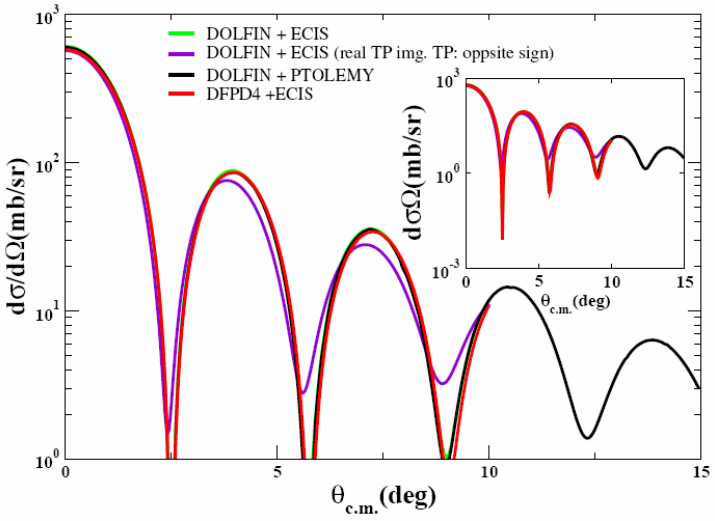

FIG. 2.6 Angular distributions of differential cross sections calculated for α inelastic scattering to the giant monopole resonance having energy E_x=12.5 MeV with different folding calculations (**DOLFIN** and **DFPD4**) and different coupled channel calculations (**PTOLEMY** and **ECIS**).

For GR with L≥2 and excitation energy E_x=12.5 MeV, using a nuclear and transition potential obtained by single folding from **DOLFIN**, **ECIS** calculations always give a higher differential cross section at small angles than **PTOLEMY** calculations (see Fig. 2.7-2.9). However if the Coulomb calculation is turned off, this difference disappears, which indicates that the difference is due to the different treatment of the Coulomb interaction in these two codes. For the **ECIS** calculation, the Coulomb part of the optical and transition potentials are obtained from DFPD4 calculations (see (2.100) and [78]), while for **PTOLEMY** calculation, they are calculated by the code in which the coulomb potential is estimated with equation (2.103) and transition potential is evaluated with the following expression:

$$V_C^{\ell}(r) = \frac{3Z_pZ_Te^2}{2\ell+1}\beta_C R_{CX}^{'}\begin{cases}\dfrac{r^{\ell}}{R_C^{\ell+2}}, & r < R_C \\ \dfrac{R_C^{\ell-1}}{r^{\ell+1}}, & r \geq R_C\end{cases}, \quad where\ R_C = R_P + R_T, R_{CX}^{'} = R_{C0}A_T^{1/3} \quad (2.107)$$

Table 2.2 Difference in maximum cross section for giant resonance with L=0-4 and E_x=12.5 MeV for 240 MeV α + ^{144}Sm due to different folding analysis (single folding and double folding).

	Single folding analysis			Double folding analysis			difference in max. dσ/dΩ
L	Folding	DWBA	Max. dσ/dΩ (mb/sr)	Folding	DWBA	Max. dσ/dΩ (mb/sr)	
0	**DOLFIN**	**PTOLEMY**	601	**DFPD4**	**ECIS**	577	4%
1	**DOLFIN**	**PTOLEMY**	724	**DFPD4**	**ECIS**	767	6%
2	**DOLFIN**	**PTOLEMY**	163	**DFPD4**	**ECIS**	178	8%
3	**DOLFIN**	**PTOLEMY**	249	**DFPD4**	**ECIS**	276	10%
4	**DOLFIN**	**PTOLEMY**	311	**DFPD4**	**ECIS**	345	10%

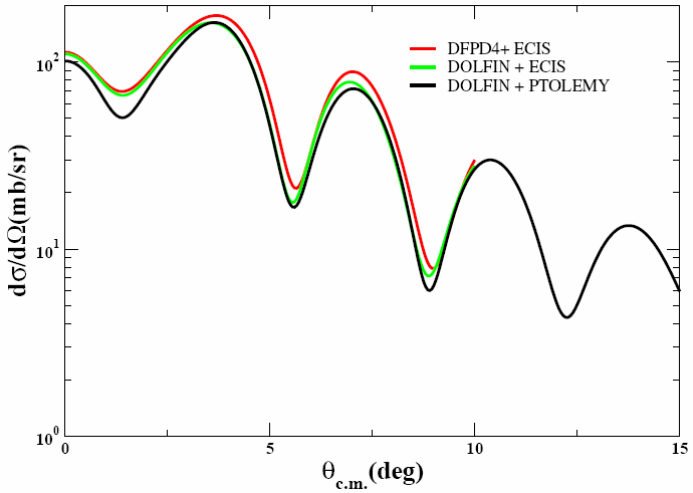

FIG. 2.7 Angular distributions of differential cross section calculated for α inelastic scattering to a giant quadrupole resonance with energy E_x=12.5 MeV with different folding calculations (**DOLFIN** and **DFPD4**) and different coupled channel calculations (**PTOLEMY** and **ECIS**).

The angular distributions of the differential cross sections obtained from **ECIS** and **PTOLEMY** with single folding potentials (calculated by **DOLFIN**) are also compared

to those obtained from **ECIS** with double folding potentials calculated by **DFPD4** for L = 2, 3, 4 with E_x=12.5 MeV (see Fig. 2.7-2.9). There is about 10% difference in amplitude between the single and double folding calculations (see Table 2.2). Compared to **DOLFIN**, **DFPD4** has some new features[101], such as, the interaction is scaled by a kinematic factor to take into account the kinematical transformation of the interaction from the NN frame to the nucleus-nucleus frame, some improvement in the numerical interpolation subroutine is incorporated. **ECIS** also has some difference compared to **PTOLEMY**, such as, relativistic kinematics is used in **ECIS** while non-relativistic kinematics is used in **PTOLEMY**, etc., however when ECIS and PTOLEMY are compared for single folding calculations, the differences are small except at small angles where the different Coulomb treatment is important.

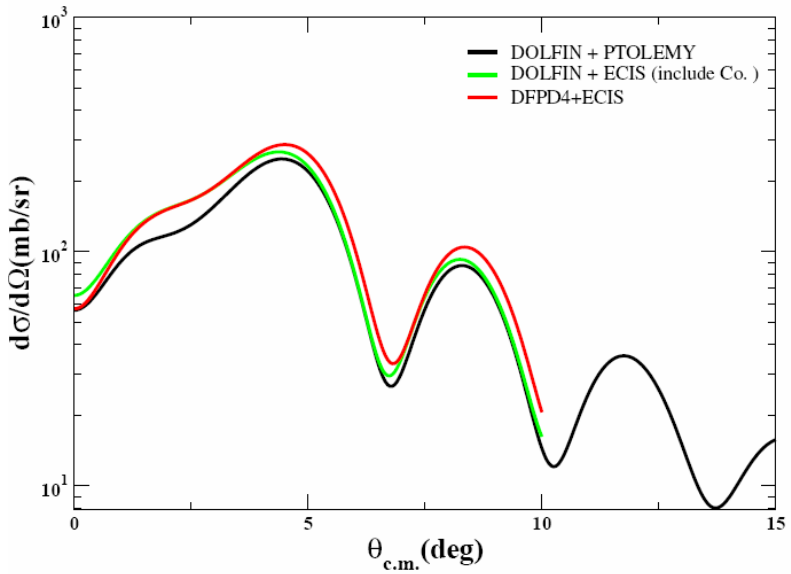

FIG. 2.8 Angular distributions of the differential cross section calculated for α inelastic scattering to the HEOR resonance at energy E_x=12.5 MeV with different folding calculations (**DOLFIN** and **DFPD4**) and different coupled channel calculations (**PTOLEMY** and **ECIS**).

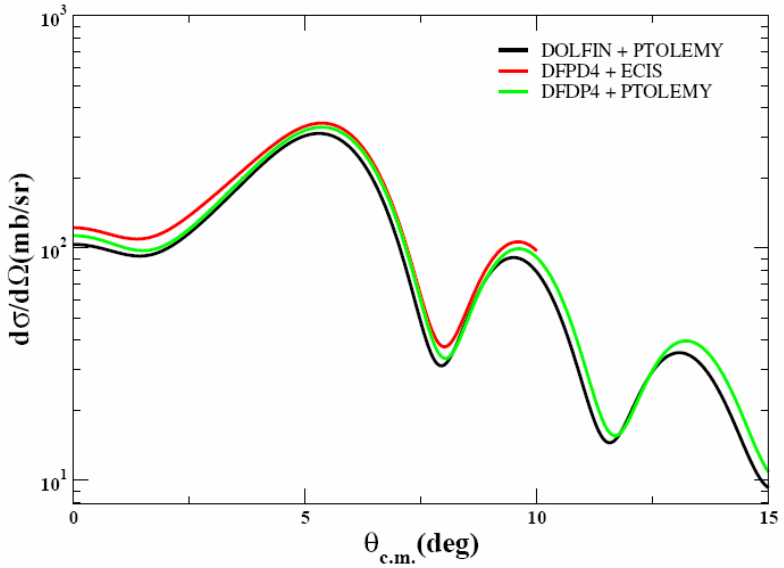

FIG. 2.9 Angular distributions of the differential cross section for L=4 excitation calculated for α inelastic scattering to giant resonance energy E_x=12.5 MeV with different folding calculations (**DOLFIN** and **DFPD4**) and different coupled channel calculations (**PTOLEMY** and **ECIS**).

3. EXPERIMENT SETUP AND CALIBRATION

3.1 Experiment Setup

Ions of $^{6}Li^{2+}$ from the ECR source were injected into the K500 superconducting cyclotron for acceleration to 240 MeV and stripped up to 3^{+} charge state in the beam line. The ^{6}Li ions passed through the beam analysis system and bombarded self-supporting target foils located in the target chamber of the multipole-dipole-multipole (MDM) spectrometer (see Fig. 3.1). The outgoing particles were detected with the focal plane detector of the MDM spectrometer. The position, energy and timing information, after shaping by electronics, were recorded on line with the data acquisition system. The functions of each part and experimental details are discussed below.

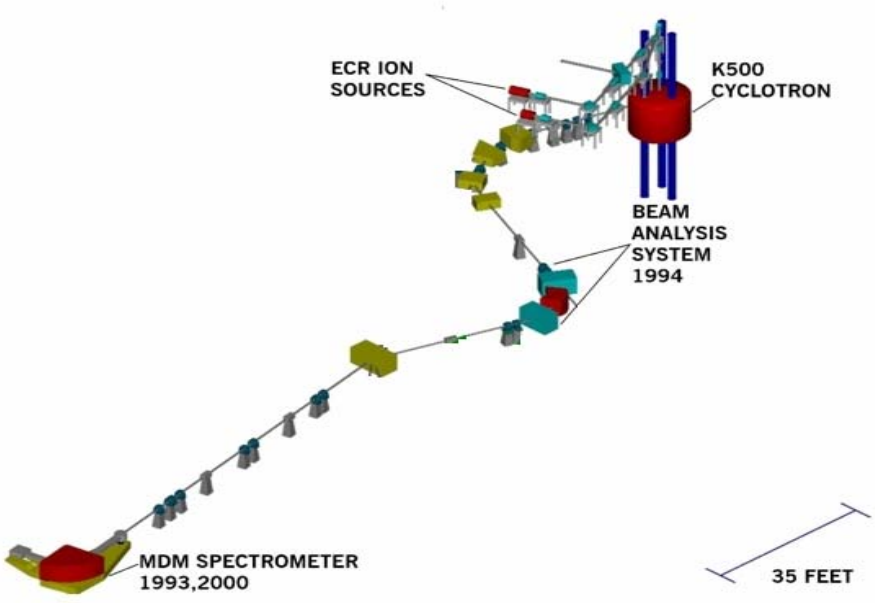

FIG. 3.1 The experimental setup of ^{6}Li scattering.

3.1.1 Beam Analysis System

The positive ion beam from the K500 cyclotron has an aberration limited resolution ΔE/E of approximately 1/700, while the giant resonance studies require a beam with moderate resolution (ΔE/E<1/2000) and free from slit scattering and halo. A beam analysis system disperses the beam with a magnetic bend, then selects a part of the beam with slits whose width determines the resolution of the beam that is passed to the target. The beam analysis system [102]for the Texas A&M K500 cyclotron uses distributed n = 0 dipoles with external quadrupole focusing elements. It provides a dispersion of 19.3 cm per % ΔP/P with an ultimate aberration limited resolution of ΔE/E up to 1/2500 for the full emittance of the beam from the K500 cyclotron. A total of 175° of bend, in opposite direction 88° and 87° segments, is used with an intermediate focus between the segments. The first half is used to disperse and limit the beam with the second half serving to remove slit scattered particles so that a very clean beam can be transported to the MDM spectrometer for zero degree inelastic scattering measurements.

3.1.2 Multipole-dipole-multipole (MDM) Spectrometer

The MDM spectrometer was constructed at Oxford University in 1982 and later brought to Texas A&M for use with the K500 cyclotron. It consists of multipole magnet, field clamp, dipole magnet, another field clamp and another multipole magnet listed in the order along the beam direction (as shown in the Fig. 3.2) (note: the multipole magnet after the dipole was not used in these experiments) It has an aberration limited resolution ΔE/E of 1/4000, and an 8 msr maximum solid angle (80 mrad for horizontal acceptance and 100 mrad for vertical acceptance). The details of the design, properties and testing of MDM spectrometer are given in Ref. [103]. The dipole magnet has a linear gradient field, and 100° of total bend with a 1.6 m central radius. It provides a large dispersion, with a low magnification and a high mass-energy product. The advantage of the single dipole magnet is that it provides simplicity and reliability for operation of MDM under experimental conditions. The spectrometer provides a horizontal linear magnification M_x=0.4 and a vertical linear magnification M_y=5.0.

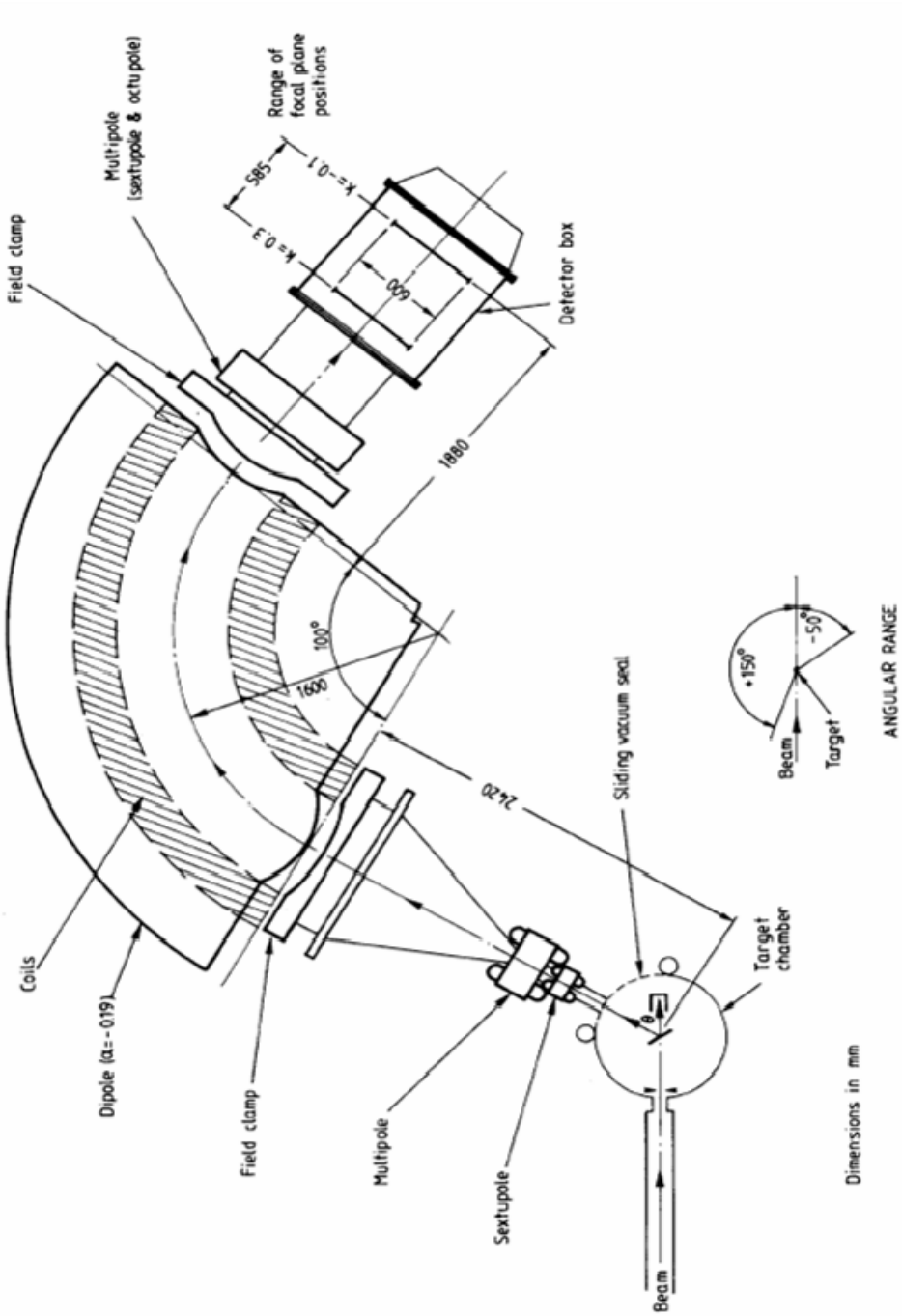

FIG. 3.2 Layout of the spectrometer which shows the magnet elements, target chamber and detector chamber (originally from [103]).

When the spectrometer was set at 0°, the beam passed through the beam pipe located on the high ρ side of the detector box and stopped in a Faraday cup inserted in a wall (see Fig. 3.3). In order to protect the detector from radiation damage, shielding consisting of a layer of lead brick and 24 inch thick plastic and paraffin was put behind the detector to attenuate the flux of neutrons and gamma rays. When the spectrometer was set at 4°, the beam was collected in a Faraday cup in the slit box. At 6° and above, the beam was stopped in a Faraday cup inside the target chamber. When the spectrometer was set at angles greater than ~ 10°, paraffin and lead shielding were placed between the detector and the target chamber.

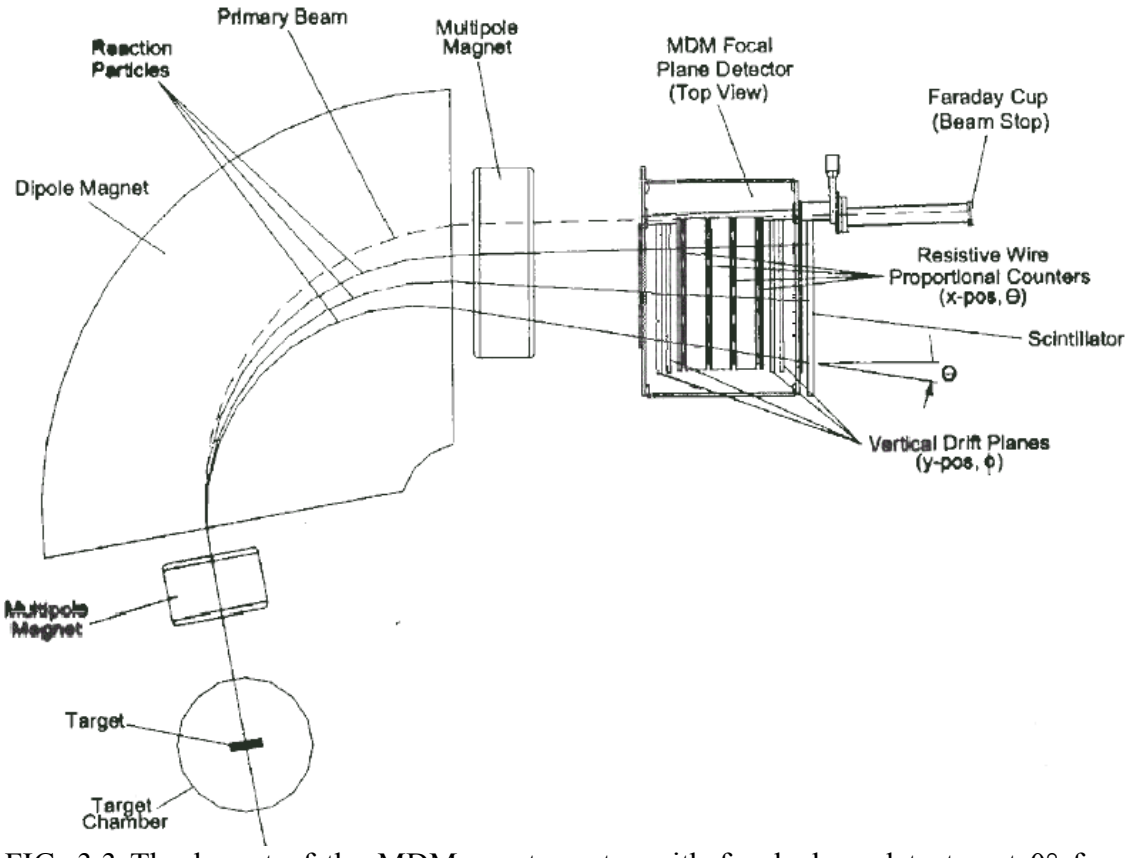

FIG. 3.3 The layout of the MDM spectrometer with focal plane detector at 0° for giant resonance measurement.

3.1.3 Focal Plane Detector for MDM Spectrometer

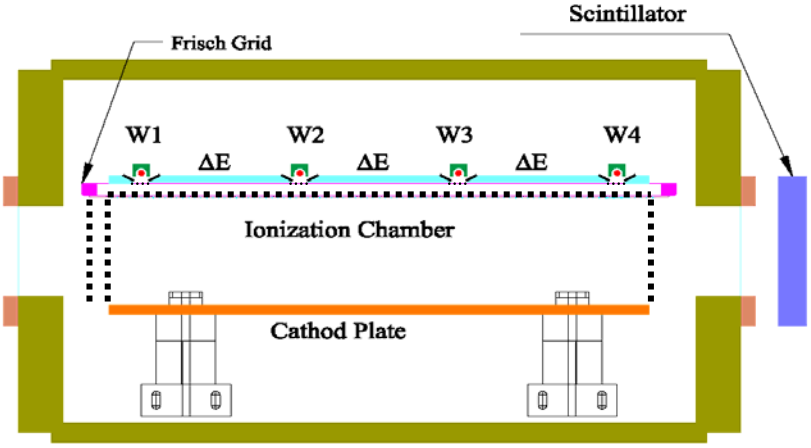

FIG. 3.4 Cross section view of the focal plane detector of MDM spectrometer.

The focal plane detector of the MDM spectrometer [104, 105] must measure position and angle of the particles entering the detector so that ray tracing can be used to determine the position where the particle intercepts the focal plane and the angle the path of the particle makes as it enters the spectrometer (related to the scattering angle). In addition, the dE/dx (energy loss) and total energy are measured to aid in particle identification. A cross-section of the detector is shown in Fig. 3.4. There are four 60 cm long resistive wire counters (spaced at 13.55 cm intervals) to measure horizontal position from which angle information is derived, an ionization chamber to provide ΔE signals and a scintillator on the back to measure total energy and to provide a fast timing signal. An electrical diagram of the components of the detector is shown in Fig. 3.5.

Gas ionization chambers [106] have been used for many years to determine the energy loss of charged particles. The simplest ionization chamber has two plane parallel electrodes in a gaseous medium with an electrostatic field between them. The electrons freed by the ionization are collected on the positive plate. However, the positive ions produced in the ionization, which have mobility 1000 times slower than electrons, induce a charge on the anode. This causes a pulse from the anode to have a nonlinear response to the energy loss in the gas chamber. O.R. Frisch [107] suggested that a grid

(usually called a Frisch Grid) fixed at a voltage lower than the anode and placed near the anode but between the anode and cathode would screen the effects of positive ions (as shown in Fig. 3.6) from the anode. The drift field in the ionization chamber is then determined by the voltage between the Frisch grid and the cathode. However some of the drifting electrons will be collected on the Frisch grid, reducing the signal on the anode. The details of the design of grid ionization chambers were given by Bunemann, *et al.* [106] and the main criteria used in building the chamber are summarized below.

Assuming the applied potentials are $\mathbf{V_a}$ on the cathode, $\mathbf{V_g}$ on Frisch grid wires and $\mathbf{V_p}$ on the anode (now called the collector plate), the inefficiency of the shielding is defined as [106]

$$\sigma \equiv \frac{dE_P}{dE_Q} \approx \frac{d}{2\pi p}\log\left(\frac{d}{2\pi r}\right), \quad for \quad V_p - V_g = const., \tag{3.1}$$

where E_p is the field between the grid and collector plate and E_Q is the field induced by the positive charges created in the ionization region between the Frisch grid and the cathode. On the other hand, the condition on potential difference for zero grid interception (transparency) can be expressed as[106]

$$\frac{V_p - V_g}{V_g - V_a} \geq \frac{p + p\rho + 2l\rho}{a - a\rho - 2l\rho} \tag{3.2}$$

where $\rho = \frac{2\pi r}{d}$ and $l = \frac{d}{2\pi}(\frac{1}{4}\rho^2 - \log\rho)$, **a** is the distance between cathode and the Frisch grid.

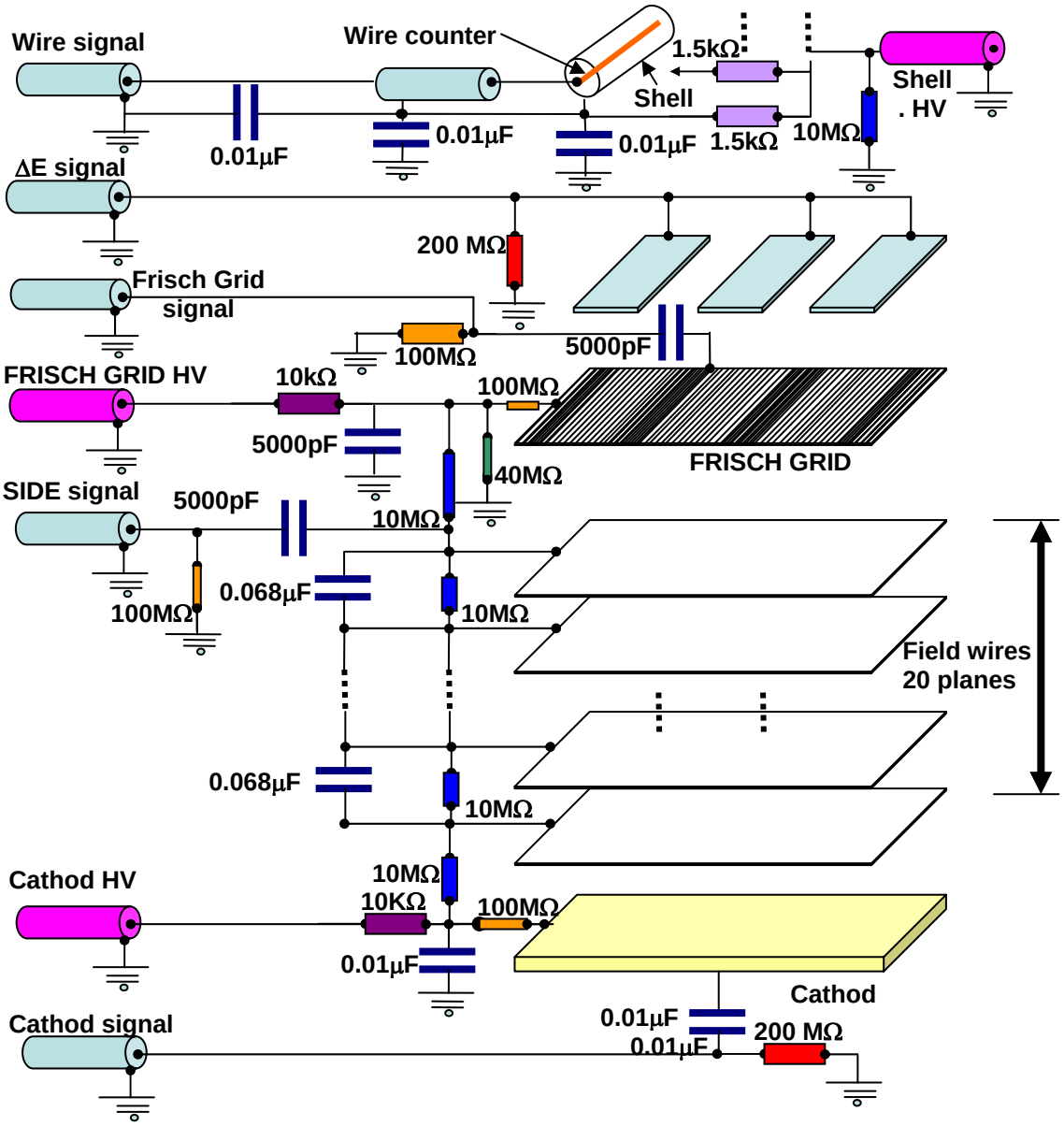

FIG. 3.5 Diagram of electrical circuit to provide HV for each component and to obtain signals from ionization chamber and wire counters (originally from H.L. Clark [108]).

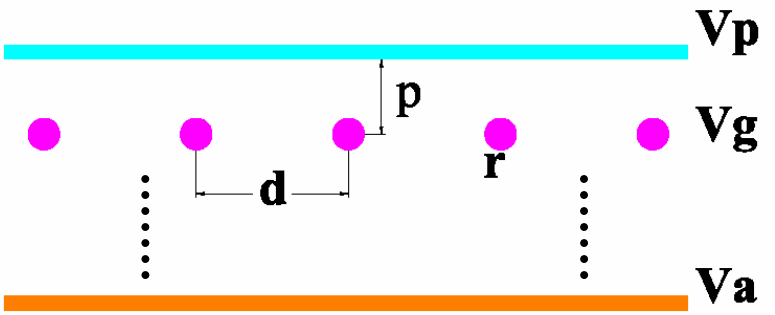

FIG. 3.6 Diagram of ionization chamber with Frisch grid. The blue plate on the top is the anode, the orange plate on the bottom is the cathode and the pink circles are Frisch grid wires. **r** is the radius of the Frisch grid wire, **p** is the distance between the Frisch grid and the anode and **d** is the pitch of the Frisch grid wires. $\mathbf{V_a}$, $\mathbf{V_g}$, $\mathbf{V_p}$ are the electric potentials for cathode, Frisch grid wires and anode respectively. Black dots means the actual distance between cathode and Frisch grid is much large than that shown in the figure.

The balance between small σ for efficient shielding and high transparency depends on proper choice of **d,** the pitch of the Frisch grid wire, **p,** the distance between the Frisch grid and the collector plate, and the high voltages on the cathode and Frisch grid. For the ionization chamber in the MDM focal plane detector, the radius of the Frisch Grid wire (BE copper alloy) r = 50.8 μm, the pitch d = 1.5 mm, p = 15 mm, a = 105 mm. Negative 3000 V was applied to the cathode, while negative 667 V was distributed on Frisch grid wires and the anode was grounded through a 200MΩ resistence. So the inefficiency σ =0.025 and $\frac{V_p - V_g}{V_b - V_a} = 0.25 > 0.22$, where 0.22 is the condition limit for zero grid interception. The electric circuits for the ionization chamber are shown in Fig. (3.5).

The resistive wire counters [109] measure position by charge division. The charge collected at each end of a resistive wire is proportional to the distance from the point the charge is injected to the other end. Assume a resistive wire with total length *L* and two

ends A and B. If a certain charge is injected at C, somewhere on the wire, and Q_A and Q_B are detected at end A and end B respectively, the distance AC then can be expressed as

$$AC = \frac{Q_B}{Q_A + Q_B} L \,. \tag{3.3}$$

The resistive wire used in the wire counter is STABLOHM 675, obtained from California Fine Wire Company, with diameter of 0.0007 inch and R = 1678 Ω/FT. The four wire counters are mounted directly above the ionization chamber. As a particle passes through the ionization chamber beneath the wire counters, electrons released by the ionization drift toward the Frisch grid and pass through the Frisch grid and some eventually drift into the avalanche region of the wire counter through the gap between the ΔE plates. Four small grids between the wire counters and Frisch Grid are used to shield the Frisch Grid from the large number of positive ions generated in the avalanche region.

The detector was filled with a mixture of 97% isobutane gas and 3% Dimethoxymethane alcohol (http://www.sigma-aldrich.com) with the gas pressure typically set at 150 torr. It has been shown [110-112] that isobutane has two advantages over argon-methane mixtures for hybrid counter use: a greater stopping power and less multiple scattering. The alcohol is used to clean the wires. Gas flows continuously through the detector to avoid the contamination in the detector which results from the impurity of the gas and ionization processes (ionization changes the properties of the gas). The details of the gas control system are shown in Fig. (3.7). Isobutane gas from the gas bottle passes through a 247C MFC gas flow controller and is split into two flows. About 94% of the gas goes directly to a gas mixer, while ~ 6% of the gas bubbles through the alcohol bottle and then flows to the gas mixer containing ~3% alcohol. The isobutane-alcohol mixture then passes through an electric valve to the detector. The pressure at the inlet to the detector is maintained at 600 torr by dynamically adjusting the opening of an electric valve controlled with MKS 250B controller. The gas mixture flow through the detector and

then is pumped out with a roughing pump. The pressure in the detector chamber is maintained by an electric valve on the pump out flow with another MKS 250 controller.

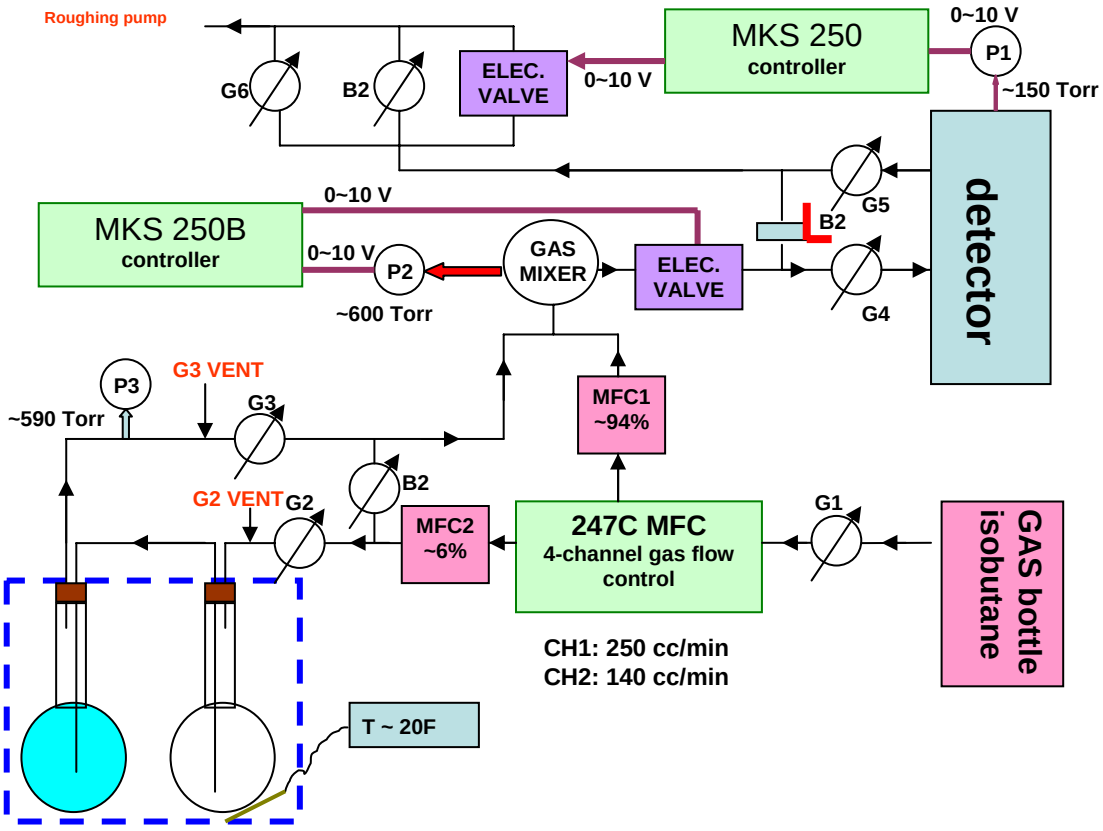

FIG. 3.7 The gas control system for MDM focal plane detector (from H.L. Clark [113]).

A 25.4μm thick Poly-Aramid foil is used as front window and a 0.25mm Mylar foil is used as back window in the detector. For 240 MeV ^{6}Li particles, the energy loss in the front window is about 500 keV and the energy loss in the back window is 4~5 MeV. A 5mm BC400 plastic scintillator on the back of the detector is used to provide energy loss and fast timing signals. The thickness of 5mm is chosen to allow separation of the ^{6}Li particles from α particle and deuterons. Compared to inorganic crystal scintillation detectors, a plastic scintillator offers a very fast signal with a decay constant of about 2~3 ns and a high light output. It comes in many sizes and shapes and can be easily machined. For the MDM focal plane detector, a conical Lucite light guide was glued to

one end of the scintillator and coupled to a HAMAMATSU H1949 photon-multiplier tube (PMT).

3.1.4 Electronics and Data Acquisition System

There are two kinds of high voltage (HV) supplies needed for the detector. The photomultiplier tubes used for the monitor detector inside the target chamber and for the scintillator behind the focal plane detector require several mA of current and the Tennelec TC 952 was used for these. The BERTAN 375P(N) was used for applications that draw no or very little current, such as HV for the position wires, the cathode, the beam pipe correction field and the shell. The voltages applied to various elements of the detector and typical currents for the 240 MeV ^{6}Li scattering experiments are listed in Table 3.1. The diagram of electronics of signal processing and the data acquisition system is shown in Fig. 3.8.

Table 3.1 The voltages applied to different components of the detector and typical current for 240 MeV ^{6}Li scattering.

	Wire1	**Wire2**	**Wire3**	**Wire4**	**Cathode**	**Beam pipe**	**Shell**	**Monitor**	**PMT**
HV for Elastic (V)	1662	1661	1664	1664	-3000	-2230	199	-652	-1680
HV for Inelastic (V)	1663	1663	1662	1663	-3000	-2230	202	-709	-1680
typical current	0 μA	0 μA	0 μA	0 μA	16.1 μA	43.1 μA	20 μA	several mA	several mA

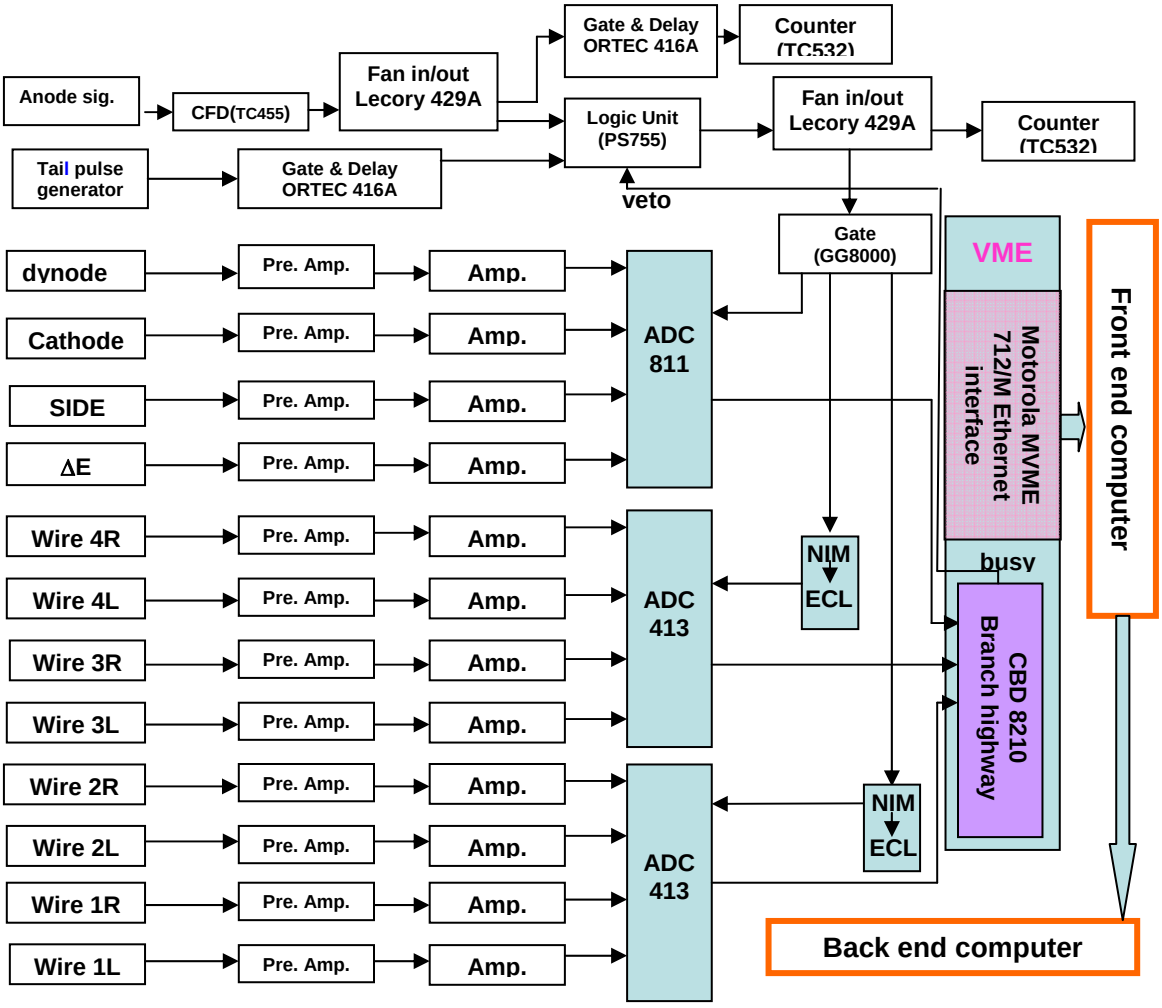

FIG. 3.8 The diagram of electronics of signal processing and the data acquisition system. The preamplifiers used for wire counters are modified CANBERRA 2004 preamplifiers. The preamplifiers used for Cathode, side and ΔE signals are CANBERRA 2004 preamplifiers. The preamplifier used for the dynode signal is the ORTEC 113 preamplifiler.

During the experiment, the signal of the phototube dynode from plastic scintillator provided an energy loss signal while the phototube anode signal provided a fast timing trigger for each event. A TENNELEC TC 455 constant-fraction discriminator (CFD) was used to convert the anode signal into logic signal. Noise was rejected by setting the threshold higher than the noise level. The output of the CFD, together with the logic

signal from a random (in time) pulse generator and a veto signal from a CBD 8210 module (veto signal is given when the module is busy transfering data to the front end computer and can not accept signals from ADC's) were added by a coincident logic unit ORTEC 755 and then passed through the GG8000 to produce gate signals with adjustable width for ADC's. Eight charge signals collected from left and right ends of the 4 wire detectors, a ΔE signal from collector plate, and a cathode signal went through CANBERRA 2004 preamplifiers and were converted into negative unipolar voltage pulses for which the peak amplitude was linearly proportional to the charge input. The outputs of the preamplifiers were sent to ORTEC 571 or 671 spectroscopy amplifiers, shaped into Gaussian pulses and then converted into digital signals by AD413 or AD811. The dynode signal first went through an ORTEC 113 preamplifier and was sent to an ORTEC 571 spectroscopy amplifier and then converted into a digital signal by AD811. All the digitalized signals were passed on by branch highway cable from CAMAC crate to VME front end, which consists of a VME crate with a CBD 8210 module and a Motorola MVME 712/M Ethernet interface module. A Dell PowerEdge 1650 computer worked as a front end host server connected with the electronics through optical fiber for data acquisition. Another DELL PowerEdge 2950 was used to analyze data on-line as well as to store data on disk for off-line analysis.

3.1.5 Experimental Details

The targets were self-supporting foils, 9.9 mg/cm^2 thick enriched to 95% in ^{116}Sn, 7.56 mg/cm^2 thick natural Si and 4.35 mg/cm^2 thick enriched to 99% ^{24}Mg. The thickness of the Sn target was determined by measuring the energy loss of a 240 MeV α beam passing through the target. The thickness's of Si and Mg targets were determined by measuring the energy loss of the 240 MeV ^{6}Li beam passing through the target. The procedure for each target thickness measurement was as follows : a) measure the position in the focal plane of the particles without a target in place; b) measure the position with the beam passing through the center of the target; c) repeat a) again (to check the beam stability); d) measure the position with the beam passing through the

upper part of the target (to check the uniformity of the target). ^{6}Li inelastic scattering was measured over an excitation energy range from several MeV to 60 MeV to obtain giant resonance data. ^{6}Li elastic scattering was also measured to extract optical potential parameters. The magnet field settings, the spectrometer angles and the slit openings used in both elastic and inelastic scattering are listed in Table 3.2.

Table 3.2 The spectrometer angles and magnetic field settings used for measuring the elastic scattering and inelastic scattering for ^{116}Sn, ^{28}Si and ^{24}Mg. The numbers in parenthesis are the slit opening used (horizontal × vertical in degree).

	^{116}Sn		^{28}Si		^{24}Mg	
	Elastic	GR	Elastic	GR	Elastic	GR
Dipole Field (Gauss)	11001.0	10679.5	11001.0	10679.5	11001.0	10679.5
Quad. Field (Gauss)	7546	7550	7546	7550	7546	7550
θ_{spec}	5°, 7°, 9° (4°×2°) 11°, 13°,15°, 17°, 19°,21°, 23°, 26°,29°, 32°, 35° (4°×4°)	0°, 4° (4°×4°)	5°, 7°, 9° (4°×2°) 11°, 13°,15°, 17°, 19°,21°, 23°, 26°,29°, 32°, 35° (4°×4°)	0°, 4° (4°×4°)	5°, 7°, 9° (4°×2°) 11°, 13°,15°, 17°, 19°,21°, 23°, 26°,29°, 32°, 35° (4°×4°)	0°, 4°, 6° (4°×4°)

3.2 Detector Calibration and Data Processing

3.2.1 Position Calibration

Data were taken for the elastic scattering of ^{6}Li from ^{12}C using an entrance slit for the spectrometer that had 5 narrow vertical openings, spaced to correspond to -2°, -1°, 0°, 1°, 2° relative to the central ray (see Fig. 3.9) entering the spectrometer. This was repeated for sixteen dipole-field settings such that the focal plane positions of the ^{6}Li ions spanned the useful length of the detector. The positions of the centroids of peaks for

each wire counter were obtained for all sixteen dipole-field setting (channel numbers). They were then compared with **RAYTRACE** [114] predictions of the position (in centimeters) to obtain the relation between the channel number and position (in centimeters) along the focal plane for each of the four wire detectors.

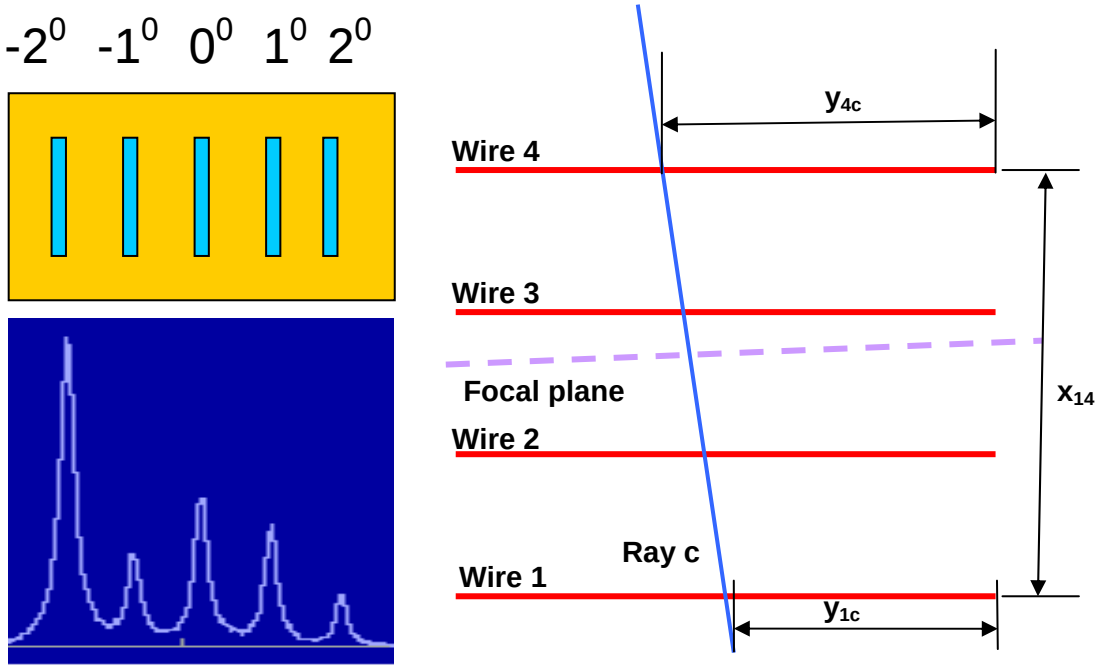

FIG. 3.9 Figure at the top left is a schematic of the collimator used to obtain angle calibrations and calibrations of channel number versus position for each of the resistive wires. The figure on the bottom left is a spectrum taken with this collimator showing the calculated angle. The figure on the right shows schematically the four resistive wires and the parameters defining a ray and the location of the focal plane.

3.2.2 Angle Calibration

An angle calibration was obtained by measuring inelastic scattering of ^{6}Li from ^{12}C providing particles covering the entire detector using the same collimator in the opening to the spectrometer as for the position calibration (see Fig. 3.9). The angle in the detector

for each ray was calculated from the positions of the ray measured on two resistive wires (usually wire1 and wire 4 are chosen for angle calculations). For example, as shown in Fig. 3.9, ray **c** is one ray with detector angle θ_{Dc}, for which y_{1c} and y_{4c} are the positions measured by wire1 and wire 4 respectively. Assuming the distance between wire 1 and wire 4 is x_{41}, the angle θ_{Dc} for ray **c** can be expressed as:

$$\tan\theta_{Dc} = \frac{y_{4c} - y_{1c}}{x_{41}}. \tag{3.4}$$

This angle measured at the detector and the position of this ray along the focal plane are then used to calculate the angle that the particle traveled away from the target relative to the beam. This angle relative to the beam at the target is then converted into an integer between 0- 4096 for plotting in spectra. From the resultant angle spectrum, the centroid channels for the five peaks corresponding to the openings in the slit are obtained and fitted with a linear expression:

$$\theta_i = a + b \cdot N_i \tag{3.5}$$

where $\theta_i = -2^0, -1^0, 0^0, 1^0, 2^2$, N_i is the centroid channel for each peak in the angle spectrum and a and b are fitted parameters for angle calibration.

Both $4° \times 2°$ (horizontal and vertical angle acceptances of 4° and 2° respectively) and $4° \times 4°$ solid angle defining slits were used in experiments. Each data set was divided into 10 angle bins (as shown in Fig 3.10) so that each angle bin corresponded to $\Delta\theta \approx 0.4°$. The average angle for each angle bin was obtained by integrating over the height of the height of the slit and the width of the angle bin. Assuming the *i*th angle bin is divided into many small areas S_j and θ_j is the angle extended from center of the small area to the center of the target, the average angle $\bar{\theta}_i$ for the angle bin can be approximately expressed as:

$$\bar{\theta}_i = \frac{\sum S_j \theta_j}{\sum S_j} \tag{3.6}$$

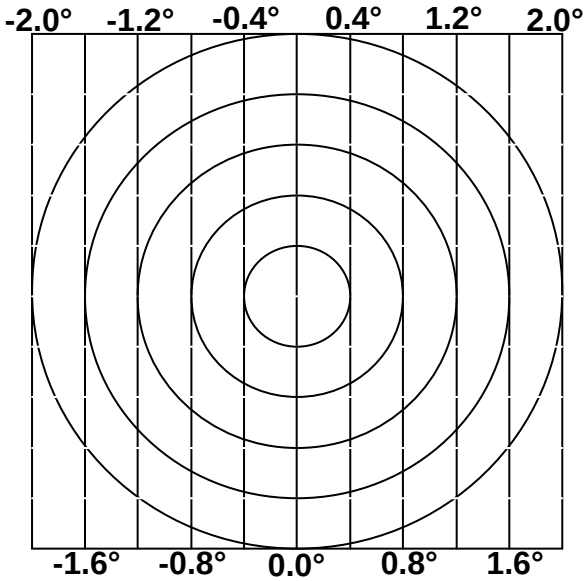

FIG. 3.10 The figure shows a 4°× 4° slit opening with each circle showing the same polar angle relative to the beam direction. The area between adjacent horizontal lines represents one angle bin for which the average angle was obtained by Eq.(3.8).

3.2.3 Energy Calibration

Energy calibrations for elastic scattering were obtained from the position calibration. With **RAYTRACE** calculations, the relation between the particles momentum and position on focal plane had been obtained. So the position spectrum could be converted into a momentum spectrum with position calibration and then converted into an energy spectrum with relativistic kinematics. The energy calibrations for inelastic scattering to the giant resonance region were obtained by measuring inelastic scattering on ^{12}C, ^{24}Mg and ^{28}Si with the spectrometer set at 4^{o}, at the actual field settings used in the experiments. The positions of the 3^{-} state at E_x=10.18±0.02 MeV and 2^{+} states with E_x=18.67±0.05, 20.43±0.05 MeV[115] in ^{28}Si, the 2^{+} states with E_x= 12.86±0.05, 17.36±0.05 MeV[115] in ^{24}Mg and, and 3^{-} states with E_x= 9.641±0.005, 18.35±0.05 MeV[116] in ^{12}C were used for calibration. During the experiment, calibration runs with

a ^{24}Mg target were done before and after the data runs for each spectrometer angle to check the calibration using the 13.68±0.05 MeV 0^+ state.

3.2.4 Data Processing

The raw data files for each run were sorted into ten position spectra corresponding to ten angle bins. The position spectra were then converted into excitation energy spectra. The experimental differential cross section for a given excitation energy and angle bin was obtained with the following expression:

$$\frac{d\sigma}{d\Omega} = \frac{N'}{IN_T} = \frac{Y \times DT}{Q/Z_p \times T \times \Delta\Omega} \tag{3.7}$$

where *N'* is the reaction number per second, *I* is the flux of incident particles, N_T is the number of target nuclei per unit area, *Y* is the number of events in a particular angle bin and excitation energy range, *DT* is the correction for the dead time of electronics and computer and includes the detector efficiency, *Q* is the total charge of the beam collected by the Faraday cup, Z_P is the charge of the incident particle, *T* is the thickness of the target and ΔΩ is the solid angle. The average angle in the lab system was calculated with Eq.(3.8) and converted into center of mass angle with relativistic kinematics for further data analysis. The angular distributions of absolute differential cross section for ^{6}Li + ^{116}Sn elastic scattering and inelastic scattering to 2^+ and 3^- low-lying states of ^{116}Sn are shown in Fig. (3.11). The angular distributions of absolute differential cross section for ^{6}Li +^{28}Si elastic scattering and inelastic scattering to 2^+ and 3^- low-lying states of ^{28}Si are shown in Fig. (3.12). The angular distributions of absolute differential cross section for ^{24}Mg elastic scattering and inelastic scattering to the first 2^+ state in ^{24}Mg are shown in Fig. (3.13).

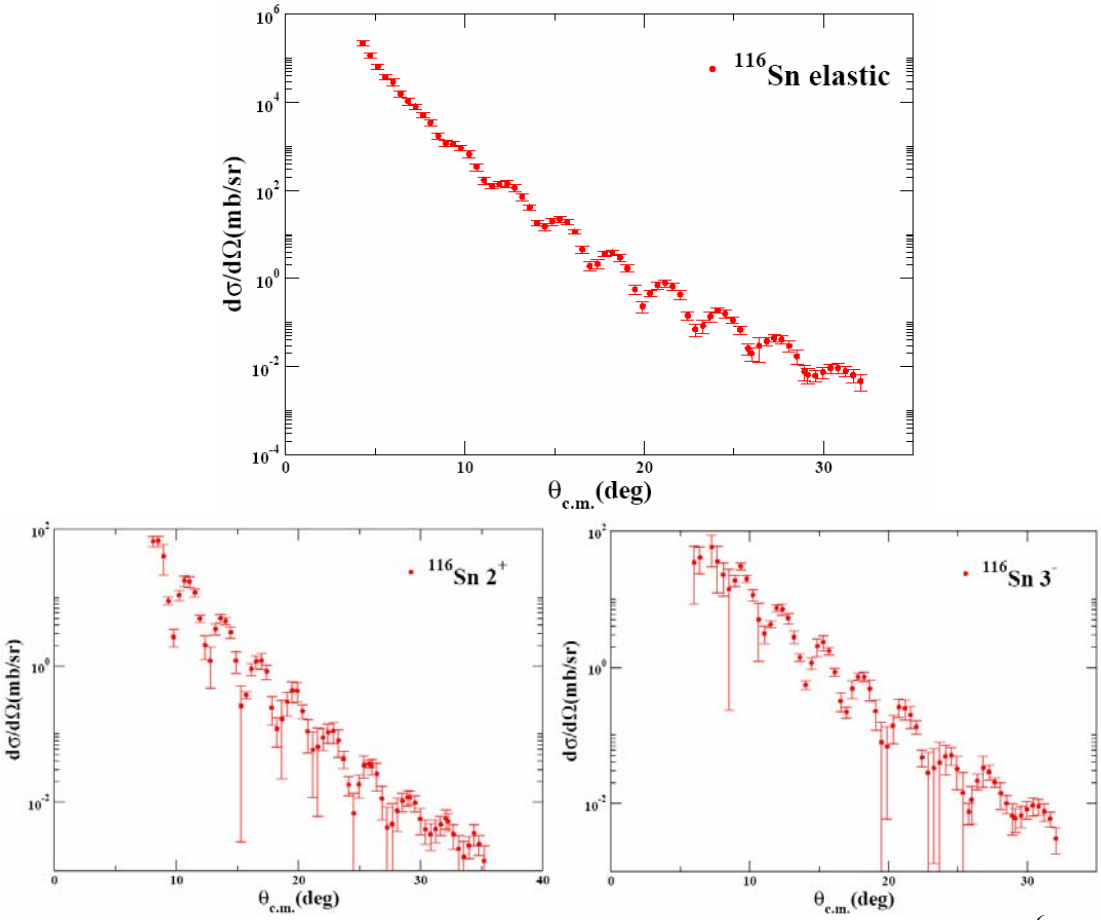

FIG. 3.11 The angular distributions of absolute differential cross section for ^{6}Li + ^{116}Sn elastic scattering and inelastic scattering to 2^{+} 1.29 MeV and 3^{-} 2.27 MeV states in ^{116}Sn are shown. The error bars shown represent statistical plus systematic errors.

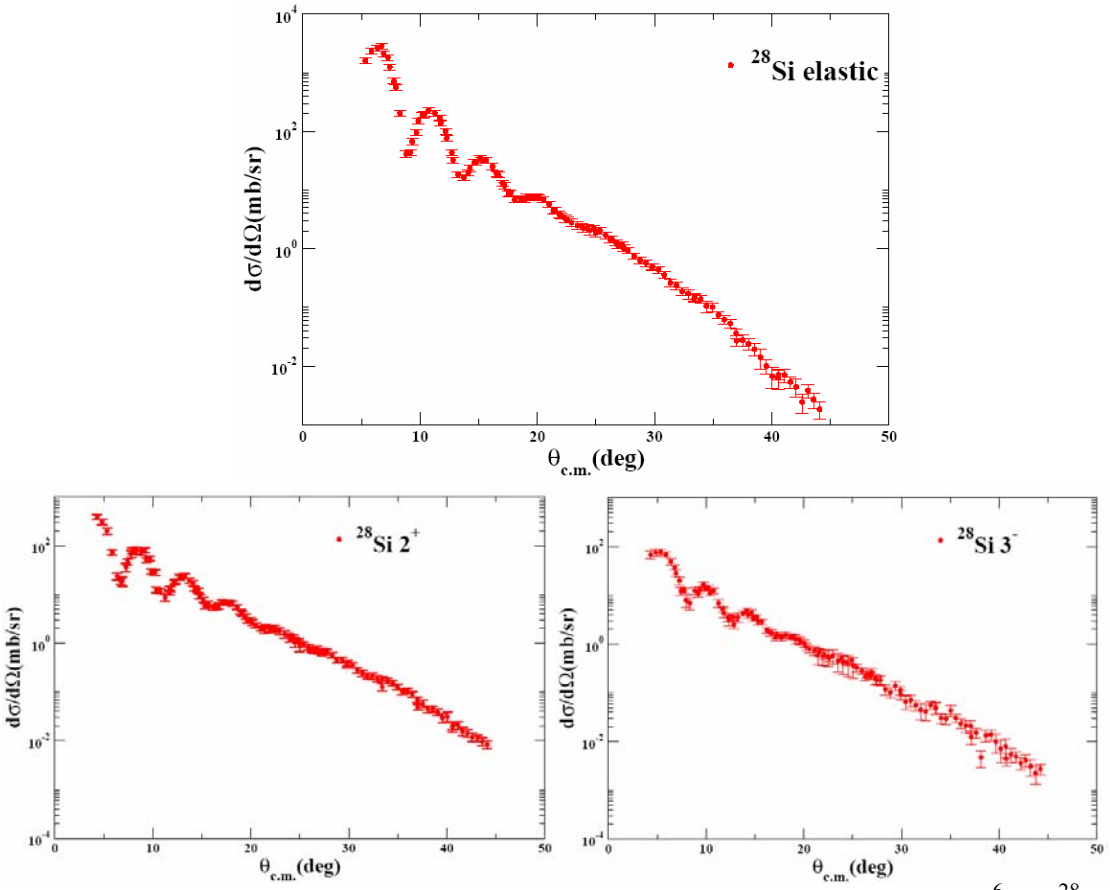

FIG. 3.12 The angular distributions of absolute differential cross section for ^{6}Li +^{28}Si elastic scattering and inelastic scattering to 2^{+} 1.78 MeV and 3^{-} 6.89 MeV states in ^{28}Si are shown. The error bars shown represent statistical plus systematic errors.

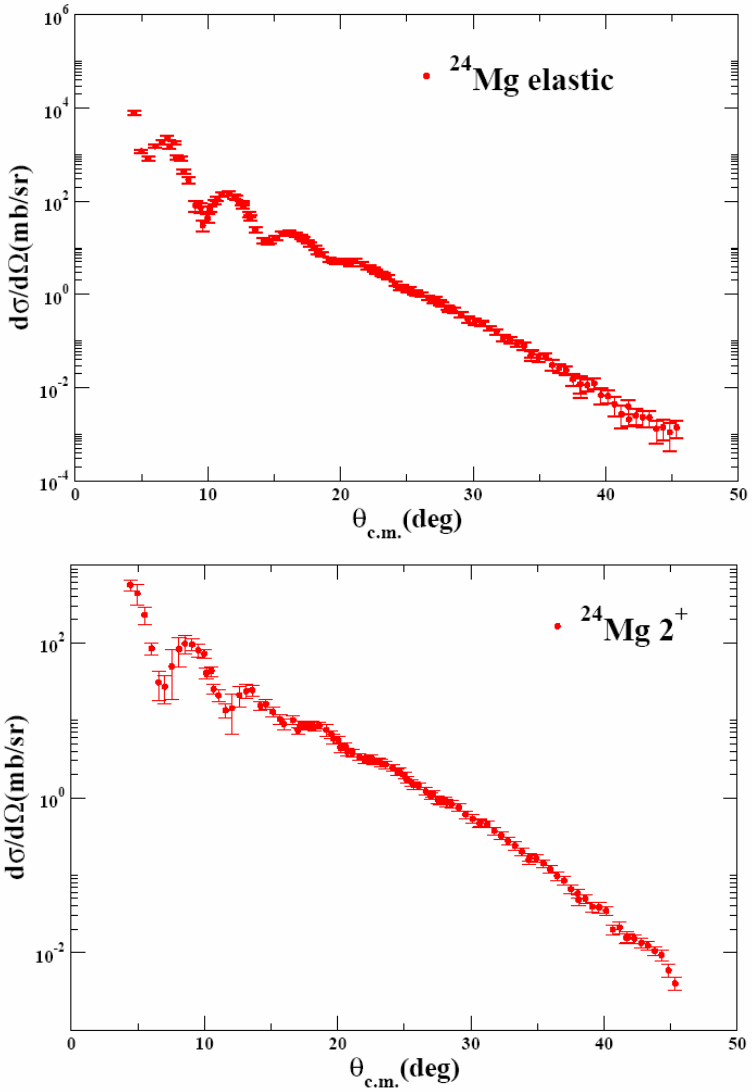

FIG. 3.13 The angular distributions of absolute differential cross section for ^{24}Mg elastic scattering and inelastic scattering to 2^{+} 1.37 MeV state in ^{24}Mg. The error bars shown represent statistical plus systematic errors.

4. DATA ANALYSIS AND RESULTS*

In this section, the data analysis is described and discussed thoroughly in detail. Section 4.2 describes the analysis of elastic scattering of 240 MeV ^{6}Li from ^{116}Sn with the optical model where optical parameters were obtained by fitting the elastic scattering data with a W-S potential and a folded potential. The cross sections of inelastic scattering to low-lying 2^+ and 3^- states were also obtained and used to check the optical potential parameters by comparing to DWBA calculations. The parameters were then used to calculate differential cross sections for inelastic scattering to giant resonances. The strength distribution was extracted and compared to those obtained by alpha inelastic scattering. In section 4.3, analysis of elastic and inelastic scattering of 240 MeV ^{6}Li on ^{28}Si and ^{24}Mg is discussed.

4.1 Data Analysis Procedure

The data analysis procedure with the double folding model calculation is shown in Fig. 4.1. The elastic scattering data was fitted by **ECIS** with the real and Coulomb potential obtained from **DFDP4**, and with W-S imaginary potential. Optical parameters obtained from fitting were checked by comparing to inelastic scattering to low-lying states. The optical parameters together with transition potential calculated by **DFPD4** for L = 0 - 4 sum rule limit were input to **ECIS** to get the angular distributions of the differential cross section. The angular distributions for L = 0 − 4 were then read to spread sheet **fit.xls** [117]. The inelastic scattering data for giant resonance were input to spread sheet **analysis.xls [117]**, where a suitable background was chosen and the GR excitation energy range was split into many small energy bins. An angular distribution of differential cross section was obtained for each energy bin. The spread sheet **fit.xls** automatically accesses **analysis.xls** to get angular distributions of the cross sections over

*Part of this section was reprinted with permission from X. Chen, et al., Physical Review C **76**, 054606 (2007), copyright (2007) by American Phyical Society.

the GR region. L = 0 − 3 strength distribution were obtained by fitting the GR data with the calculated cross sections of sum rule limits for each multipolarity.

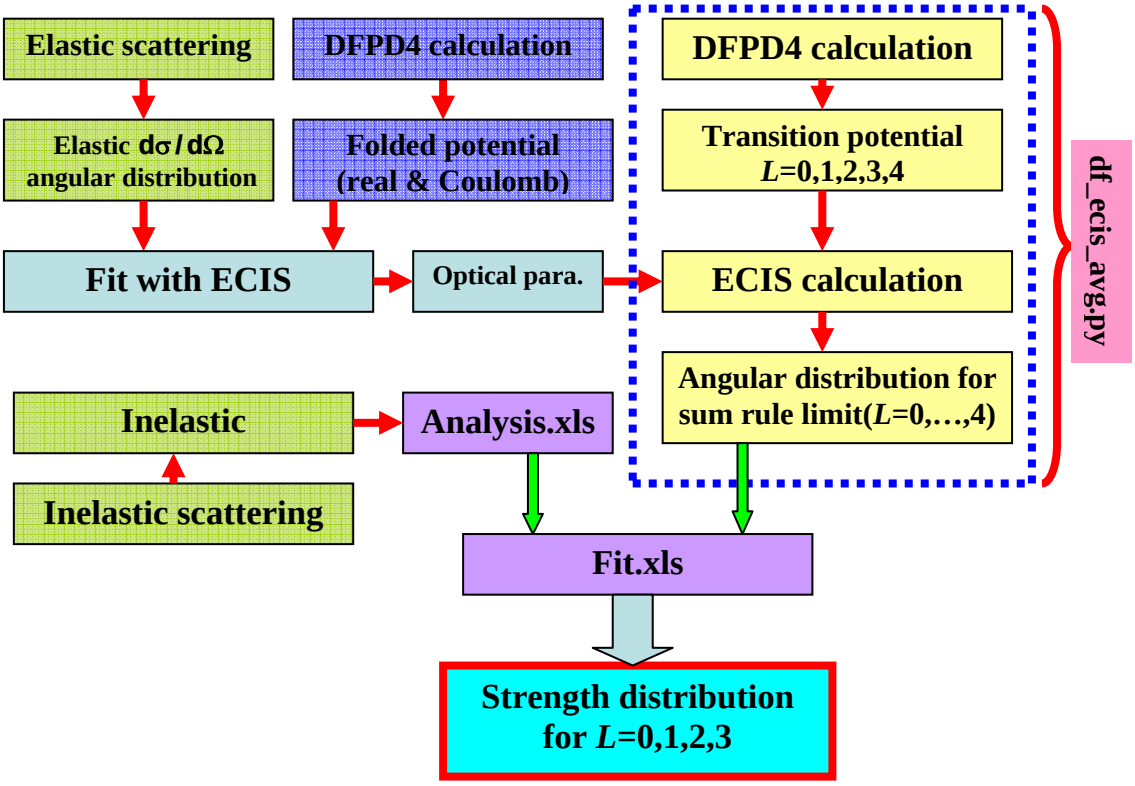

FIG. 4.1 Block diagram of the data analysis procedure.

The DFPD4 calculations of transition potentials were usually time consuming because as many one hundred of calculations have to be done for L = 0 − 4 over GR excitation range from approximately 8 MeV to 40 MeV with 1 MeV interval. Each calculation took roughly 6~7 minutes on Dell Poweredge computer with double Intel (R) 2.4GHz CPU. A computer code **df_ecis_avg.py**, written with PYTHON script, was used to control the calculations. The code fulfilled the following functions: calculate deformation parameters corresponding to sum rule limits for L = 0 − 4 for a given energy; calculates transition potential with **DFPD4** for a certain multipolarity for a given energy (The initial energy point and the energy interval is specified by input parameter file **df_ecis_avg.in)**; calculate differential cross section with **ECIS** for a certain multipolarity

and do solid angle correction; output array of differential cross sections in terms of excitation energy and center of mass angle.

The matter deformation parameters β_m^L for multipolarities L = 0 − 4 were obtained from the EWSR limit definition (see section 2). The deformation length δ_i^L for imaginary transition potential given for $L \geq 2$ are obtained with the assumption

$$\delta_m^L = \beta_m^L c = \delta_i^L \quad . \tag{4.1}$$

The deformation parameters β_i^L for imaginary transition potential for L = 0, 1 are obtained with the assumption [59, 118]

$$\beta_m^{0,1} c = \beta_i^{0,1} r_{i0} (A_T^{1/3} + A_P^{1/3}) \tag{4.2}$$

where A_T and A_P are the mass of the target and projectile respectively.

4.2 240 MeV ^{6}Li Scattering on ^{116}Sn

4.2.1 Elastic Scattering

Elastic scattering data of ^{6}Li + ^{116}Sn were fitted by the W-S phenomenological potential model and potentials derived from double folding. Fermi distributions obtained from droplet model calculations [94] were used for target and projectile density in the density independent folding (DIF) calculation. In the density dependent folding (DDF) calculation, a Fermi distribution was used for the ground state of ^{116}Sn, with the parameters obtained from Ref. [88], and the ^{6}Li ground state density was obtained from proton scattering with the cluster-orbital shell-model approximation (COSMA)[119]. The proton and the neutron densities of ^{6}Li were expressed as:

$$\rho_{n,p} = N_c \frac{\exp(-r^2/a^2)}{\pi^{3/2} a^3} + N_v \frac{2\exp(-r^2/b^2)}{3\pi^{3/2} b^5} \left[Ar^2 + B\left(r^2 - \frac{3}{2} b^2 \right)^2 \right], \tag{4.3}$$

where N_c= 2.0, N_v = 1.0, a = 1.55, b = 2.07, A = 1.0 and B = 0.0. The density parameters used in the folding calculations are listed in Table 4.1.

Table 4.1 Density parameters for the folding calculations. Fermi parameters c (half density radius) and a (diffuseness) are given for the matter distribution. R_m and R_{Coul} stand for mean square root radii for matter distribution and Coulomb interaction respectively.

model	density form	Nucleus	c(fm)	a(fm)	R_m(fm)	R_{Coul}(fm)
DIF	Fermi[94]	^{6}Li	1.508	0.5	2.195	2.195
	Fermi[94]	^{116}Sn	5.469	0.5	4.626	4.626
DDF	COSMA[119]	^{6}Li	—	—	2.444	1.833*
	Fermi[88]	^{116}Sn	5.49	0.515	4.663	4.253*

*****Uniform charge distribution is used in the calculations to estimate the Coulomb interaction for elastic scattering.

Elastic scattering fits with W-S phenomenological potentials were carried out with **ECIS**. The W-S potential has the 3-parameter form:

$$V(r) = V/[1+\exp((r-R_V)/a)], \quad R_V = r_0(A_T^{1/3} + A_P^{1/3}), \tag{4.4}$$

where A_T is the mass number of the target and A_p is the mass number of projectile. The real and imaginary parts have the same form except the parameter values are different.

Satchler and Khoa [118] found that better fits to the measurements including those taken at angles beyond the Fraunhofer diffraction region were obtained by a hybrid model in which the real interaction was obtained with folding and the imaginary part was represented by a Woods-Saxon potential. So in this work, only the real parts of the optical potentials were obtained by a folding procedure with both the DIF model and the DDF model. The DDF folding calculations were carried out with the folding code **DFPD4** [93], while the DIF calculations were carried out with **CHEN2** [94], and the differential cross sections were obtained with ECIS. In the DIF calculation, the Reid version of the M3Y NN interaction was used and the knock-on exchange contribution

was represented by zero-range approximation which is a δ function with strength shown in Eq. (2.74). In the DDF calculation, the Paris version M3Y NN interaction was used and the knock-on exchange effect was represented by a finite range approximation shown in Eq. (2.75). The density dependent function is expressed as [77]:

$$F(\rho) = 0.2658\left(1 + 3.8033e^{-1.4099\rho} - 4.0\rho\right). \tag{4.5}$$

There is also a weak energy dependence included in the density dependent NN effective interaction, which is used to reproduce the empirical energy dependence of the nucleon-nucleus optical potential [76] and is expressed as following:

$$g(\varepsilon) \approx 1 - 0.003\varepsilon \tag{4.6}$$

where ε is the bombarding energy per nucleon (in MeV). The direct term and exchange term of the NN effective interaction in the DDF calculation thus are expressed as

$$v_{D(EX)}(\rho, \varepsilon, r) = g(\varepsilon)F(\rho)v_{D(EX)}(r). \tag{4.7}$$

The optical potential parameter sets obtained from both folding model fits as well as the W-S fit are listed in Table 4.2. The calculated angular distributions for the ratio between absolute differential nuclear cross section and Rutherford cross section are plotted along with elastic scattering data in Fig. 4.2. The (real potential) renormalization factors in both folding calculation are around 0.65, consistent with earlier folding analysis of ^{6}Li scattering [69, 120]. The real parts of the potentials obtained from the different models are plotted in Fig. 4.3, where the folded potentials are multiplied by the renormalization factor N_R obtained from the fits of elastic scattering data. The amplitudes of the potentials are quite different for smaller radii, however they overlap well for radii in the surface region (R~7.4 fm is roughly the sum of radii of the projectile and target), indicating that peripheral collisions dominate in the angular range studied here. From Fig. 4.2 it is apparent that even an additional 10° (out to 40°) could have improved the parameterization and such larger angles measurements would help to determine the amplitude of interior potential.

The quality of fit of elastic scattering and inelastic scattering to low-lying 2^+ and 3^- states is estimated by χ^2, defined by:

$$\chi^2 = \frac{1}{N}\sum_{i=1}^{N}\left[\frac{\sigma(\theta_i)^{cal} - \sigma(\theta_i)^{\exp}}{\Delta\sigma(\theta_i)}\right]^2 \tag{4.8}$$

where N is the number of data points, $\sigma(\theta_i)^{cal}$ is the *i*th calculated cross section, $\sigma(\theta_i)^{exp}$ is the experimental cross section and $\Delta\sigma(\theta_i)$ is the corresponding uncertainty. The χ^2 obtained from W-S model fit is not significantly different than those obtained from folding model fits. Since there have been no ^{6}Li + ^{116}Sn scattering data reported before, the optical parameter sets from Ref. [120] for 210 MeV ^{6}Li scattering on ^{90}Zr and ^{208}Pb are also shown in Table 4.3 for comparison. Farid and Hassanain [120] obtained their χ^2 assuming the ^{90}Zr and ^{208}Pb data have uniform 10% error. In order to compare the fit for ^{90}Zr and our ^{116}Sn, χ^2 was recalculated for ^{116}Sn by assuming the data have 10% uncertainty. The calculations show that W-S model fit for ^{116}Sn data (χ^2 ~5.16) is better than the W-S fit for ^{90}Zr data (χ^2 ~8.3), while fits with double folding models for ^{116}Sn (χ^2 ~5.18) and ^{90}Zr (χ^2 ~4.9) have approximately the same quality.

Table 4.2 Optical parameters sets obtained from the analysis of ^{6}Li scattering. W-S means Woods-Saxon potential. DIF means density independent folded potential and DDF means density dependent folded potential. * means that $R_{V(W)}=r_{0(i0)}A_T^{1/3}$.

E_{6Li} (MeV)	target	Potential type	N_R	V (MeV)	r_0 (fm)	A (fm)	W (MeV)	r_{I0} (fm)	a_I (fm)	J_v (MeV fm^3)	J_w (MeV fm^3)	χ^2	σ_r (mb)
240	^{116}Sn	W-S		195.9	0.825	0.934	27.98	1.178	0.823	254.3	91.4	0.77	2885
		DIF	0.637				39.99	1.075	0.992	234.4	106.4	1.19	3031
		DDF	0.659				28.77	1.151	0.905	202.1	89.9	0.98	2956
210 [8]	^{90}Zr	W-S		177	1.182*	0.939	31.30	1.627*	0.810	257.0	106.0	8.3	2618
		DIF	0.70				31.30	1.596*	0.917	263.0	103.0	4.9	2744
	^{208}Pb	W-S		224.0	1.104*	1.001	35.10	1.518*	0.824	259.0	93.0	0.6	3536
		DIF	0.60				31.40	1.537*	0.842	224.0	86.0	1.8	3582

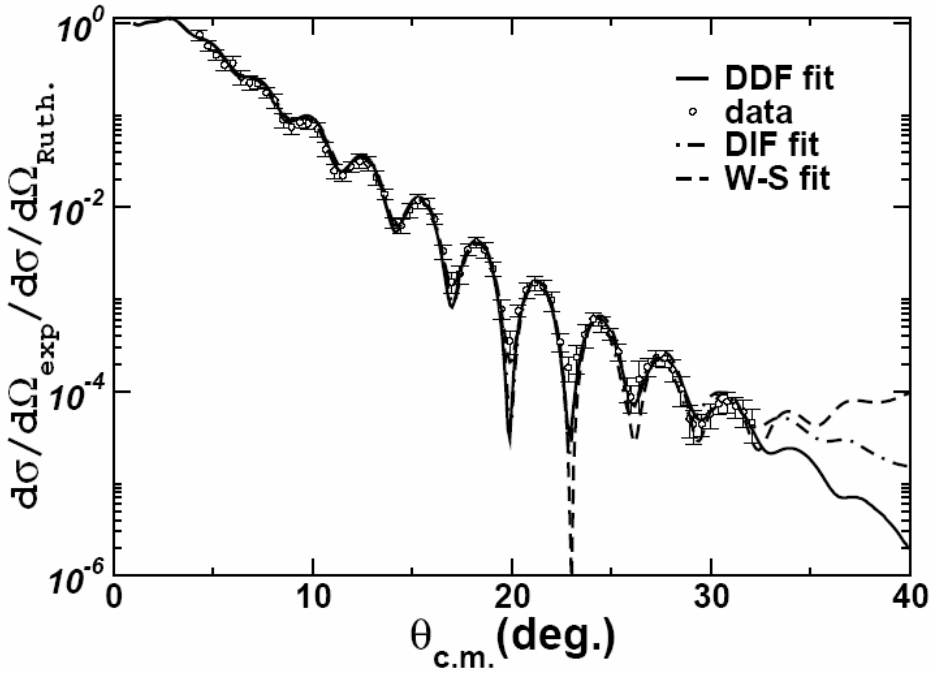

FIG. 4.2 Experimental angular distribution of the cross-section (relative to Rutherford cross section) and fits for $^{6}Li+^{116}Sn$ elastic scattering using W-S potential, DIF potential and DDF potential parameters are shown. The error bars indicate statistical and systematic errors.

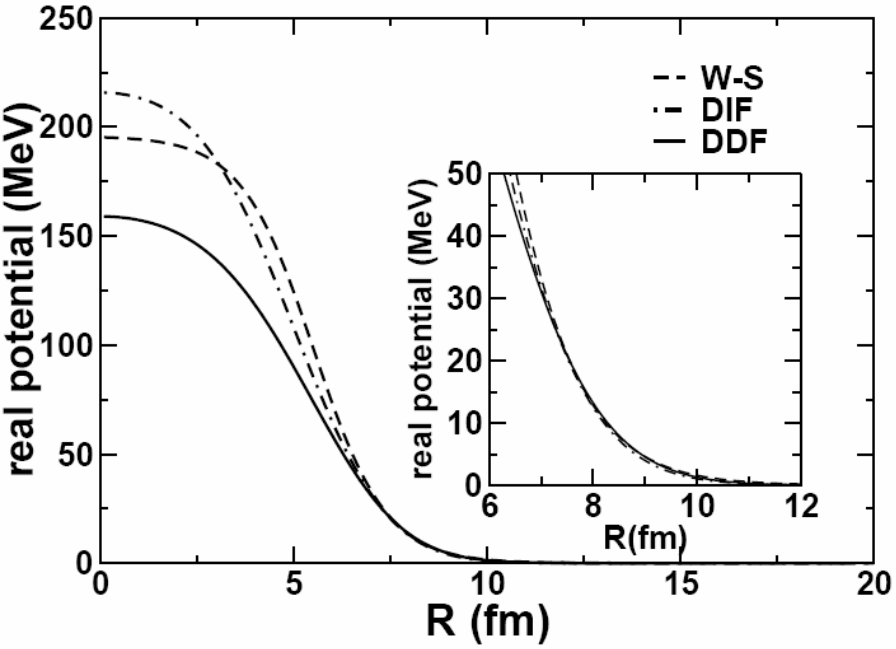

FIG. 4.3 Real optical potentials obtained from W-S, DIF, DDF models. For DIF model, the dash and dot curve shows the folded potential obtained from CHEN2 multiplied by renormalization factor N_R=0.637. For DDF model, the black curve shows the folded potential obtained from DFPD4 multiplied by renormalization factor N_R =0.659. The inset has the vertical scale expanded to show the region of overlap.

The volume integral of optical potentials per interacting nucleon pair were determined by the relation

$$J_{V,W} = \frac{1}{A_T A_p} \int V(r), W(r) d\tau \tag{4.9}$$

where V(r) and W(r) are the real and imaginary parts of the optical potential and A_T and A_P are the mass numbers of the target and projectile. Based on folding model analysis of light HI elastic scattering with density independent S1Y NN interaction at intermediate energy [121], Satchler obtained a qualitative expression for the volume integral per nucleon pair with linear energy dependence:

$$J_V^{S1Y} = -259(1 - 0.005E / A_P) \tag{4.10}$$

where E is the incident energy and A_p is the mass of the projectile. For 240 MeV ^{6}Li scattering, J_v^{S1Y}=207 MeVfm^3. Even earlier, Gupta and Murthy [122] proposed a semi-empirical formula for the real volume integrals based on nucleon-nucleus optical potential derived from the JLM interaction. The volume integral given by the semi-empirical formula is both energy dependent and target mass dependent. The value of volume integral will slowly decrease as the incident energy and target mass increase. For 240 MeV ^{6}Li scattering on ^{116}Sn, J_v^{JLM} = 217 MeVfm^3. On the other hand, Nadasen *et al*. [123] analyzed 210 MeV ^{6}Li scattering on ^{90}Zr with W-S potential model and suggested an empirical logarithmic energy dependence form for the volume integral per nucleon pair:

$$J_V^{WS} = J_0 - \beta \ln E \tag{4.11}$$

where J_0=855±30 MeVfm^3, β=113±5 MeVfm^3, and E is the incident energy of the projectile. For 240 MeV ^{6}Li scattering, J_v^{WS}=236 MeVfm^3.

These are compared with those obtained in this experiment in Fig. 4.4. The volume integral obtained with W-S potential model and DIF model are close to the calculation based on Nadasen *et al*.'s formula, while DDF calculation is closer to Satchler's expression and Gupta and Murthy's expression. The volume integral per nucleon pair for 240 MeV ^{6}Li scattering on ^{116}Sn should be slightly smaller than that of 210 MeV ^{6}Li scattering on ^{90}Zr because it has a higher incident energy and a heavier target and that is seen for both the W-S model and folding model calculations.

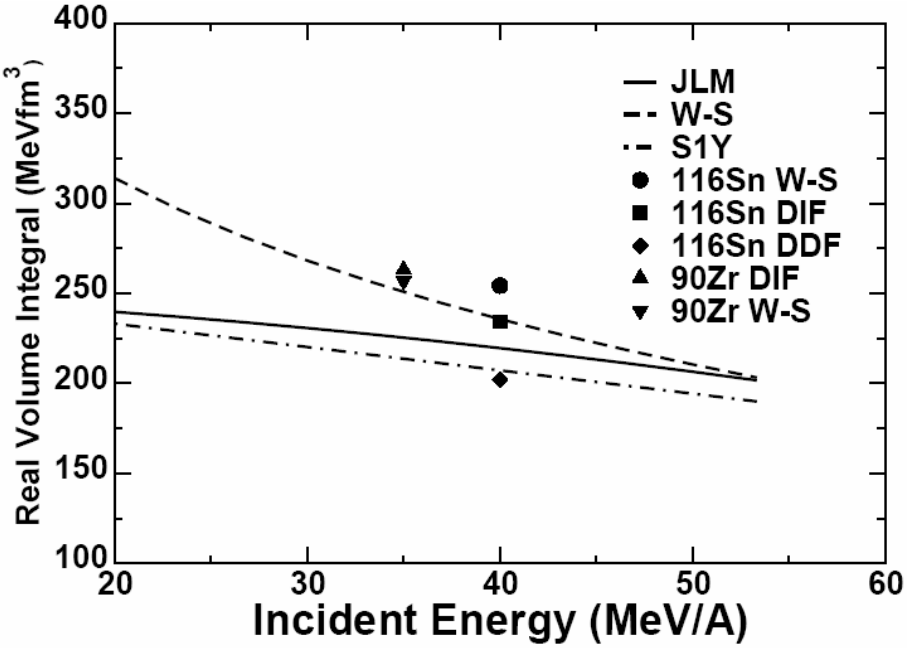

FIG. 4.4 The volume integral for real part of optical potential obtained with W-S model, DIF model and DDF model. The curves with dash, solid and dash-dot represent Nadasen *et al*.'s expression obtained with W-S potential [123], Gupta and Murthy's expression obtained with JLM effective interaction [122] and Satchler's expression obtained with S1Y effective NN interaction[121] respectively. Volume integrals obtained from Ref.[120] for 210 MeV ^{6}Li scattering on ^{90}Zr are also plotted in the figure for comparison.

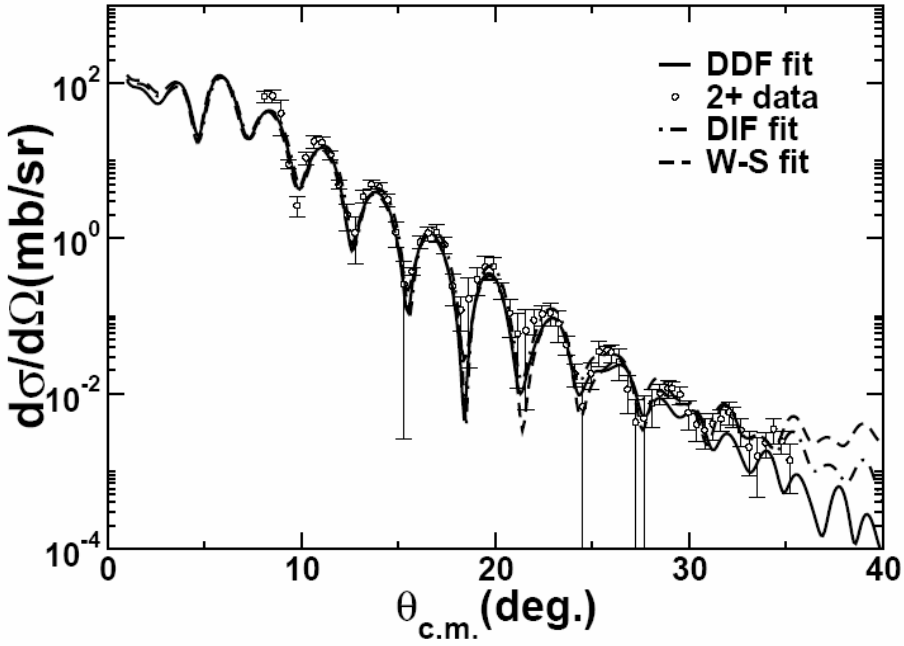

FIG. 4.5 The differential cross-sections calculated with deformed potential model and folding models for inelastic scattering to the 1.29 MeV 2^+ state of ^{116}Sn along with the data points are plotted versus average center of mass angle. The B(E2) values used for DP, DIF and DDF models calculations are best fit values of 0.229, 0.182, 0.233 e^2b^2 respectively. The error bars represent statistical and systematic errors.

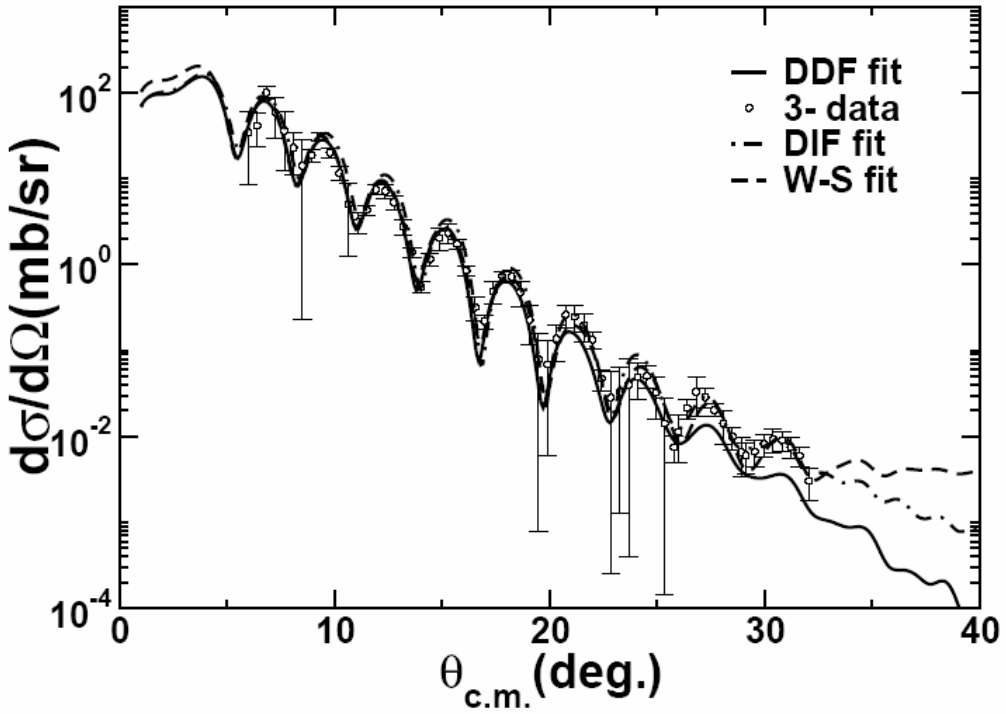

FIG. 4.6 The differential cross-sections calculated with deformed potential model and folding models for inelastic scattering to the 2.27 MeV 3^- state of ^{116}Sn along with the data points are plotted versus average center of mass angle. The B(E3) value used for DP, DIF and DDF models calculations are best fit values of 0.116, 0.101, 0.133 e^2b^3 respectively. The error bars represent statistical and systematic errors.

The DWBA calculations with deformed potential model and folding models for low-lying 2^+ and 3^- states of ^{116}Sn were carried out with ECIS. The angular distributions of the cross sections with different models for 2^+ and 3^- states are plotted in Fig. 4.5 and Fig. 4.6 along with the data. For the folding model calculations, the mass deformation length and coulomb deformation length were assumed to be the same, and in deformed potential model calculations the potential deformation length and coulomb deformation length were assumed to be the same. In DIF model calculation, the real transitional potentials for 2^+ and 3^- states were generated with CHEN2 and the imaginary part was obtained by the DP model, while in the DDF calculation, the real transitional potentials were generated by DFPD4 and the imaginary parts were obtained by DP model. The best

fit B(EL) values for 2^+ and 3^- states with different model calculations were extracted by fitting the inelastic scattering cross section and are listed in Table 4.3. There are two errors given for each fitted B(EL) value. The superscript one represents statistical error which comes from the fit of inelastic scattering cross sections and is about 3-4% of the fitted value. The subscript one represents the total error including both statistical error and systematic error which is about 10% of the fitted value.

The results are compared with B(EL) values obtained using electron inelastic scattering [124, 125] and α inelastic scattering [126], and also are compared with the adopted B(E2) [127] and B(E3)[128] values in Table III. The B(E2) and B(E3) values obtained with DP and DDF model in this work agree within errors with adopted values, and the values obtained from electron inelastic scattering and α inelastic scattering. It is interesting that B(EL) values obtained with DP and DDF model are very close to those obtained from α inelastic scattering. DIF model calculations do not agree with either adopted B(EL) values or B(EL) values obtained from electron scattering or α scattering. Since the scattering process explored here is peripheral, lack of the density dependence for NN interaction may not be adequate to explain the discrepancy. The density used for the projectile in DIF calculation, a Fermi distribution obtained from the droplet model which gives a radius significantly smaller than the known ^{6}Li radius[69], may not be suitable for the projectile since ^{6}Li is a loosely bound light heavy ion.

Table 4.3 The best fit B(EL) value for 2+ and 3- states of 116Sn obtained with W-S, DIF and DDF models. Adopted values of B(E2) and B(E3), as well as values extracted from α inelastic scattering and from electron scattering, are shown in the table. For B(EL) values obtained from 6Li scattering, the superscript errors represent statistical errors, while the subscript errors represent total errors including statistical and systematic errors. For α scattering, DIWS represents potential from density-independent single folding, while DDWS represents potential from density-dependent single folding.

		$J^{\pi}=2^{+}$, E_x=1.29 MeV	$J^{\pi}=3^{-}$, E_x=2.27 MeV
work	Model	B(E2)(e^2b^2)	B(E3)(e^2b^3)
present	DP	$0.229^{\pm0.007}_{\pm0.024}$	$0.116^{\pm0.003}_{\pm0.012}$
	DIF	$0.182^{\pm0.006}_{\pm0.019}$	$0.101^{\pm0.003}_{\pm0.011}$
	DDF	$0.233^{\pm0.007}_{\pm0.024}$	$0.133^{\pm0.004}_{\pm0.014}$
α scattering[c]	DP	0.231±0.023	0.114±0.012
	DIWS	0.231±0.023	0.134±0.014
	DDWS	0.231±0.023	0.134±0.014
e scattering	EM	0.229±0.015[a]	0.120±0.015[b]
	Adopted Value	0.209±0.006[d]	0.132±0.018[e]

a: Ref. [124], b: Ref. [125], c: Ref. [126], d: Ref. [127], e: Ref. [128]

4.2.2 Giant Resonance Analysis

^{6}Li inelastic scattering on ^{116}Sn to giant resonance range was measured at spectrometer angle 0° and 4°. The excitation energy spectrum for each angle bin was stored in spread sheet **analysis.xls**. The spectrum was divided into a peak and continuum, where the continuum was assumed to have the shape of a straight line at high excitation joining onto a Fermi shape at low excitation energy to model particle threshold effects as shown in Eq. (4.12) [129]:

$$Y = A + BE_X + \frac{Y_0}{1 + e^{\frac{E_x - E_{th}}{C}}} \tag{4.12}$$

where A and B are determined from a fit to the high excitation region (39~49 MeV), E_{th} and C are adjusted to model the behavior of the spectrum near the particle threshold, and Y_0 is adjusted so that the continuum obtained is zero just below the particle threshold (6~7 MeV). The excitation energy range was divided in many energy bins with bin width no more than 2 MeV. The angular distributions of differential cross section for the peak and continuum of each energy bin were obtained and sorted in the spread sheet.

^{116}Sn giant resonance data was analyzed first with the deformed potential model. A sample of giant resonance spectrum is shown in Fig. 4.7. Angular distributions for a 2.0 MeV wide bin centered at E_x=15.6 MeV of the giant resonance peak and the continuum are shown in Fig. 4.8 along with DWBA fits. The distributions of the energy weighted sum rule (EWSR) strength obtained for ISGMR, ISGDR, ISGQR, and ISGOR of ^{116}Sn are shown in Fig. 4.9. The peak positions of the ISGMR and ISGQR strength distribution are consistent with those obtained from α inelastic scattering, but there are some differences in sum rule strength. This may be due to different continuum choices or the simplicity of the deformed potential model. No matter how the continuum was chosen, unlike other multipolarities, the strength of ISGDR was always much higher than 100% of the EWSR. H.L. Clark, *et al.* [130] have pointed out that the predicted cross section for the ISGDR is very sensitive to the imaginary component of the optical and transition potential.

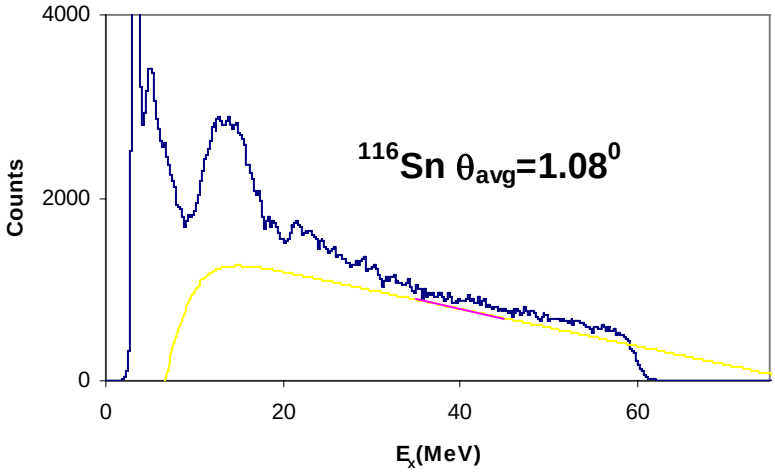

FIG. 4.7 Inelastic ^{6}Li spectrum for ^{116}Sn at θ_{avg}=1.08^0. The yellow line shows the continuum chosen for the analysis.

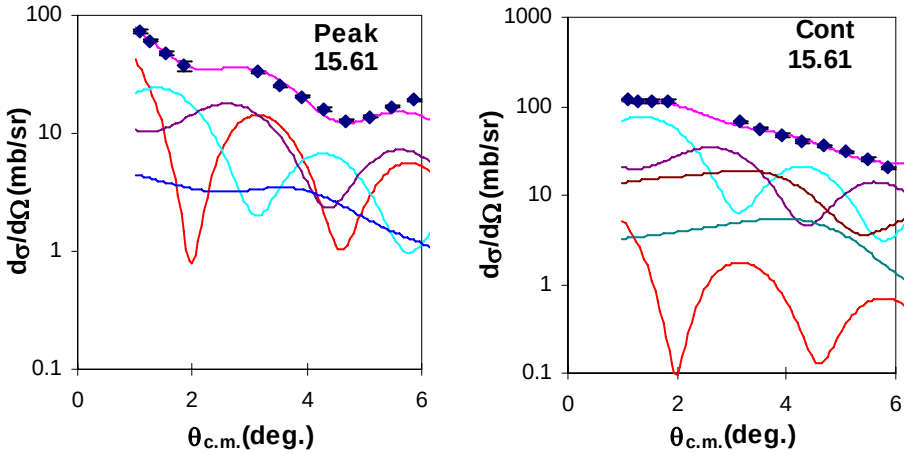

FIG. 4.8 The angular distributions of the ^{116}Sn cross section for a 2 MeV wide bin centered at the excitation energy indicated on the figure (in MeV) for ^{6}Li inelastic scattering for GR peak and the continuum. The line through the data points indicates the multipole fits. Contributions of each multipole are shown.

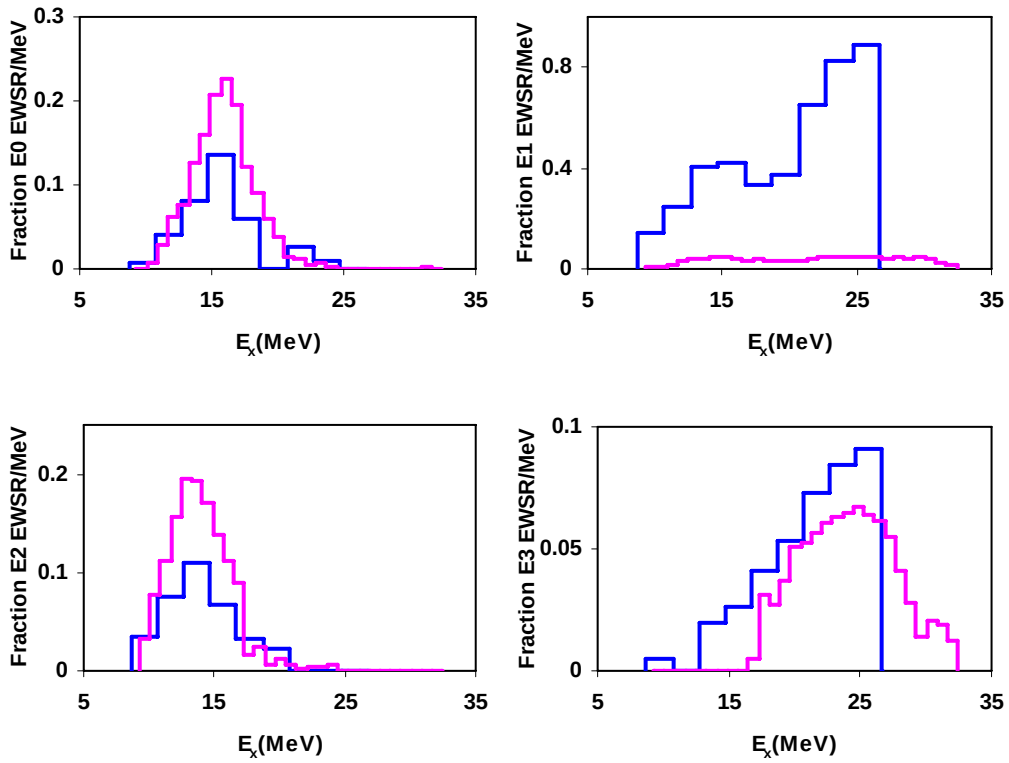

FIG. 4.9 Comparison of the strength distribution for E0, E1, E2, E3 extracted from ^{6}Li inelastic scattering using the deformed potential model (blue color) with those obtained from α inelastic scattering[5] using a folding potential (pink color).

^{116}Sn giant resonance data were then analyzed with the double folding model. The optical potential parameter set for analysis of the ^{116}Sn inelastic scattering data is the folded potential obtained with DDF model (as shown in Table 4.3). The transition potentials for L = 0−4 transitions were calculated with **DFPD4** for the excitation range from 8 MeV – 40 MeV in 1 MeV steps. The corresponding angular distributions of differential cross section were obtained with **ECIS** (see Fig.4.10). A set of angular distributions for L = 0 − 4 with E_x=15.0 MeV are shown in Fig. 4.11. The angular distributions for L = 0 peak at 0° and are well distinguished from others. Two sample excitation energy spectra at average center of mass angle 1.08° and 5.87° with continuum choice are shown in Fig. 4.12. A set of sample angular distributions for 1.6

MeV wide bins centered at E_x = 12.62, 22.20, 30.17 MeV for the giant resonance peak and the continuum are shown in Fig. 4.13 along with DWBA fits. The multipole decomposition analysis techniques used here were described in detail in Ref. [39, 40, 129, 131]. The isovector giant dipole resonance (IVGDR) contributions were calculated from the known distributions [132] and were fixed in the fits. The strength distributions obtained for ISGMR, ISGDR, ISGQR, and ISGOR of ^{116}Sn are plotted as blue curves with Gaussian fits plotted in dark green curve in Fig. 4.14.

The strength distributions obtained for E0-E3 are compared with those obtained with α inelastic scattering [49] which are plotted as red curves. The parameters obtained for E0, E2 and E3 excitation are given in Table 4.4 and those for E1 excitation are given in Table 4.5 and are compared to those from Ref. [49, 133]. There are two centroid energies listed in Table 4.4. Following the notation in Ref. [49], the first one is defined as m_1/m_0 which is described in section 1 and the second one is the peak position of Gaussian fit. Γ is the full width at half maximum (FWHM) for Gaussian fit, while Γ* is equivalent FWHM for m_1/m_0 obtained by multiplying the rms width by a factor of 2.348

$$rms\ width = \sqrt{\frac{\sum_{i=1}^{n}(E_i - E_c)^2 S(E_i)}{\sum_{i=1}^{n} S(E_i)}} \tag{4.13}$$

where E_c is the centroid energy, E_i is the average energy of each energy bin and $S(E_i)$ is the corresponding strength distribution.

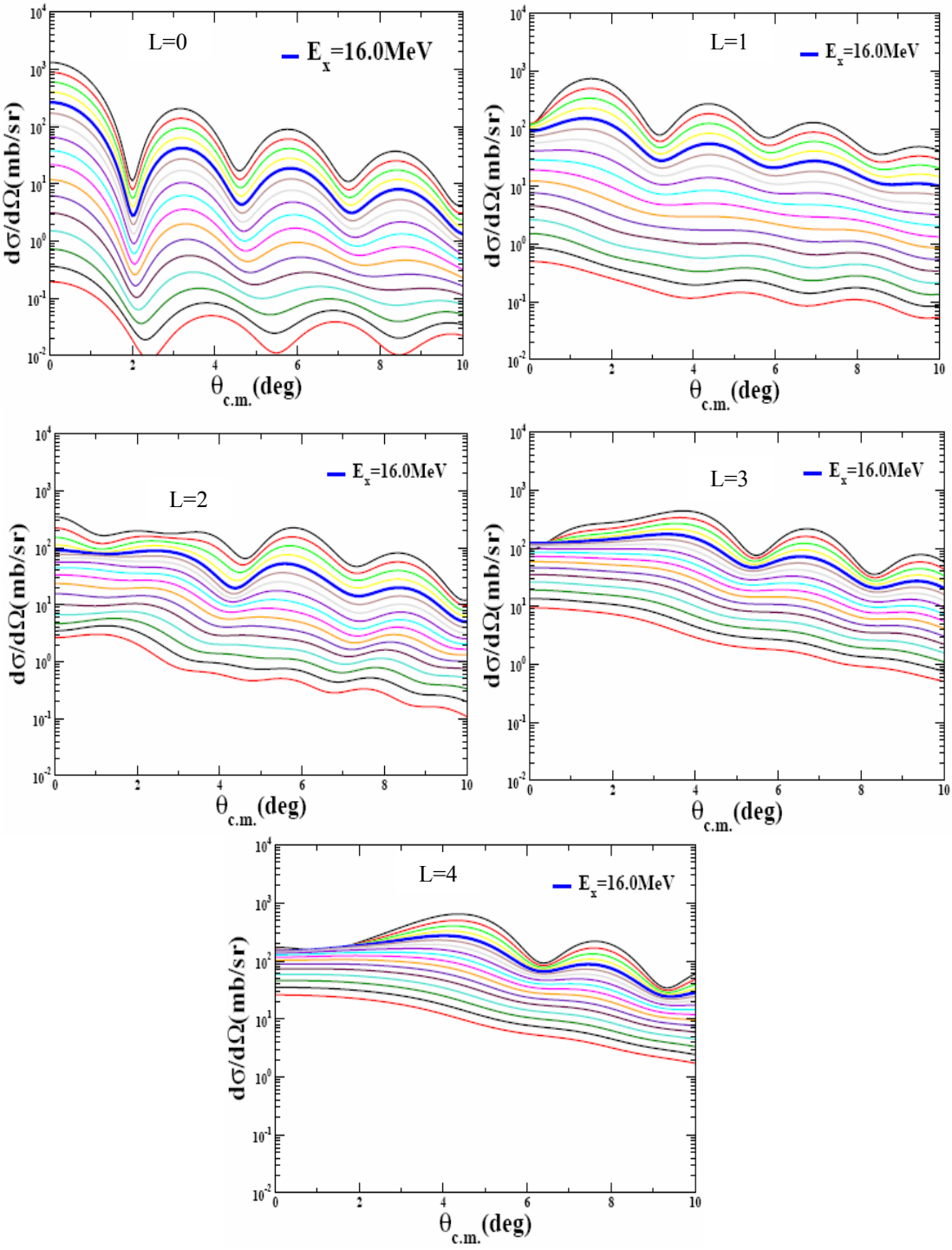

FIG. 4.10 Angular distributions of differential cross sections for 240 MeV ^{6}Li inelastic scattering from ^{116}Sn for 100% sum rule with L = 0−4 over the excitation energy range 8 - 40 MeV in 2 MeV intervals.

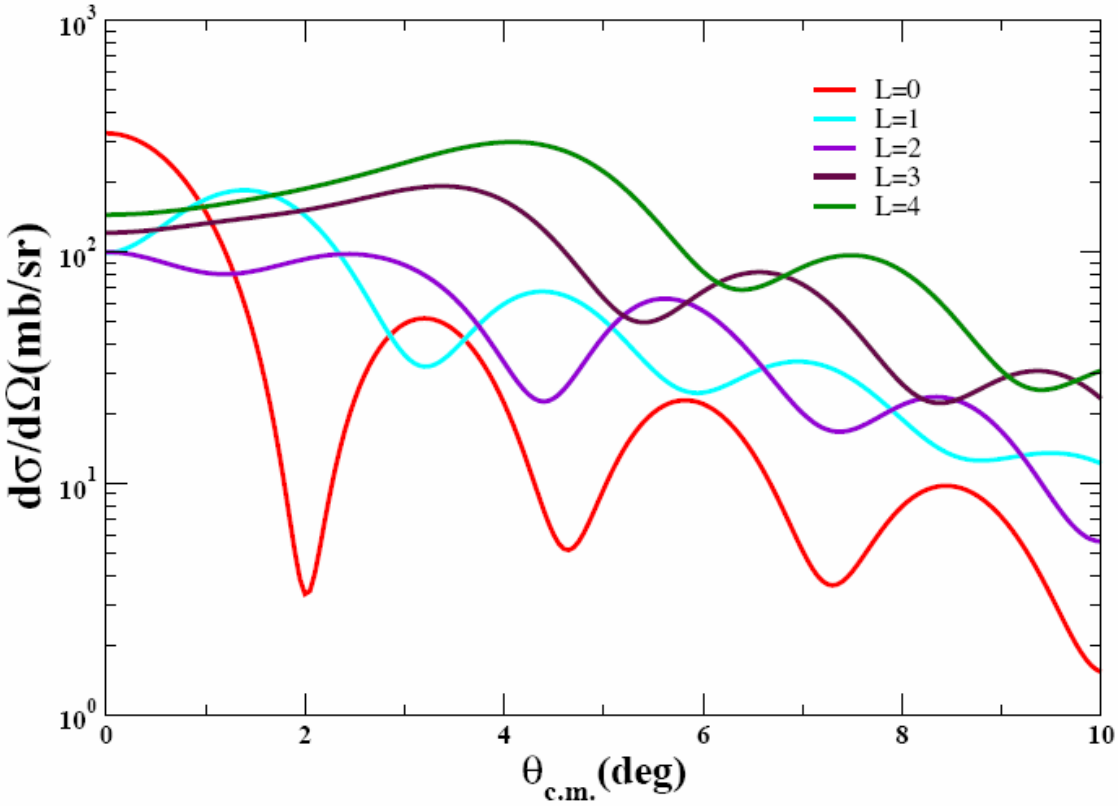

FIG. 4.11 Angular distributions of differential cross section for 240 MeV ^{6}Li inelastic scattering from ^{116}Sn with L = 0 - 4 for excitation energy E_x=15.0 MeV.

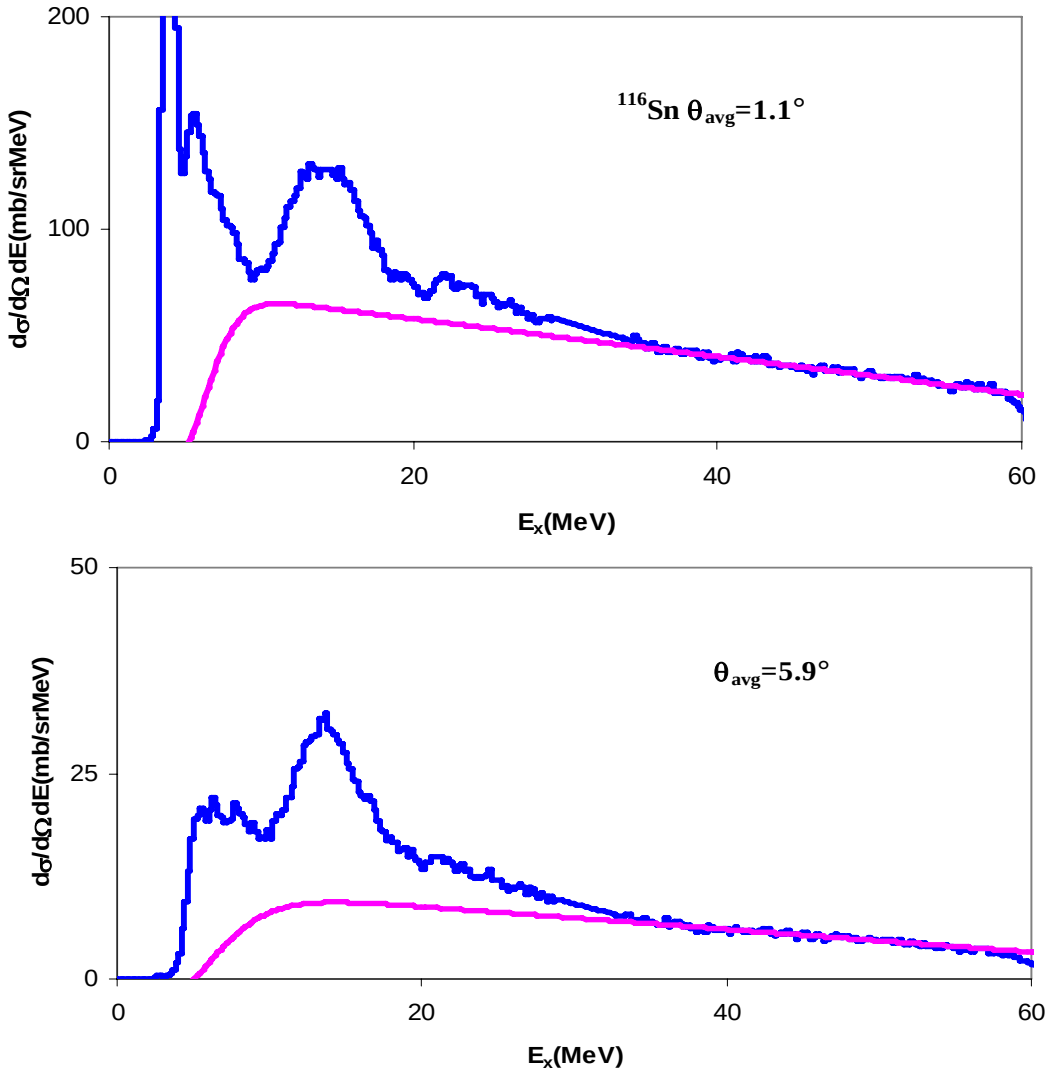

FIG.4.12 Sample excitation spectra at average center of mass angle 1.1° and 5.9° for ^{116}Sn. The pink curves are the continuum chosen for the analysis.

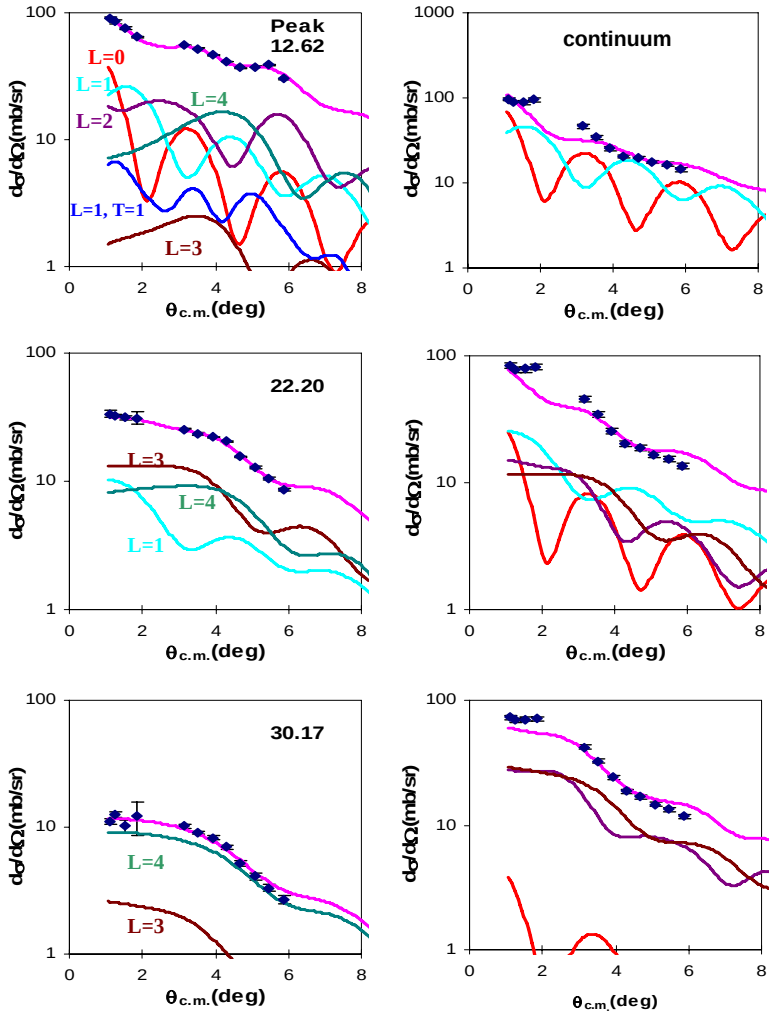

FIG. 4.13 Angular distributions of the crosssection for inelastic scattering from ^{116}Sn for 1.6 MeV wide bin centered at E_x=12.62, 22.20, 30.17 MeV of the giant resonance peak and the continuum along with DWBA fits. The left side figures are angular distributions for giant resonance peak and the right side figures are those for continuum. The pink lines through the data show the fits. The E0 contribution is shown by the red line, the isoscalar E1 contribution by the light blue line, the E2 contributions by the purple lines, the E3 contributions by the brown lines, E4 contributions by the dark green lines and the isovector E1 contributions by the dark blue lines.

Table 4.4 E0, E2, E3 multipole parameters obtained for ^{116}Sn in this work compared to those obtained from analysis of α scattering.

	240 MeV ^{6}Li scattering					240 MeV α scattering			
	m_1/m_0 (MeV)	Γ* (MeV)	Gaussian fit (MeV)	Γ (MeV)	EWSR (%)	Ref.	m_1/m_0 (MeV)	Γ* (MeV)	EWSR (%)
E0	$15.39^{+0.35}_{-0.20}$	$6.10^{+0.85}_{-0.34}$	15.58±0.19	5.46 ± 0.18	106^{+27}_{-11}	[49]	15.85 ± 0.20	5.27±0.25	112±15
						[133]	15.9±0.5*		117±12
E2	$14.34^{+0.26}_{-0.20}$	$6.90^{+0.78}_{-0.18}$	14.09±0.27	5.48±0.35	94^{+14}_{-10}	[49]	13.50±0.35	5.0±0.30	108±12
						[133]	14±0.5*		103±10
E3	21.66±0.21	10.87±0.23			116±8	[49]	23.3±0.8	10.9±0.6	70±12
						[133]	21.8±0.5	7.1±0.5	67±10

Γ* means equivalent FWMH obtained by multiplying the rms width by a factor of 2.348.

Table 4.5 ISGDR parameters obtained for ^{116}Sn in this work compared to those obtained from analysis of α scattering.

	Peak1 Gauss. (MeV)	Γ (MeV)	EWSR (%)	Peak2 Gauss. (MeV)	Γ (MeV)	EWSR (%)	Total EWSR(%)
this work	15.32±0.20	$5.56^{+0.20}_{-0.19}$	66±10	21.73±0.20	$2.80^{+0.26}_{-0.28}$	52^{+20}_{-14}	118^{+20}_{-14}
[49]	14.38±0.25	5.84±0.30	25±15	25.5±0.60	12.0±0.6	61±15	88±20
[133]	14.7±0.5	3.8±1.2	13±4	23.0±0.6	8.7±1.2	33±11	46±11

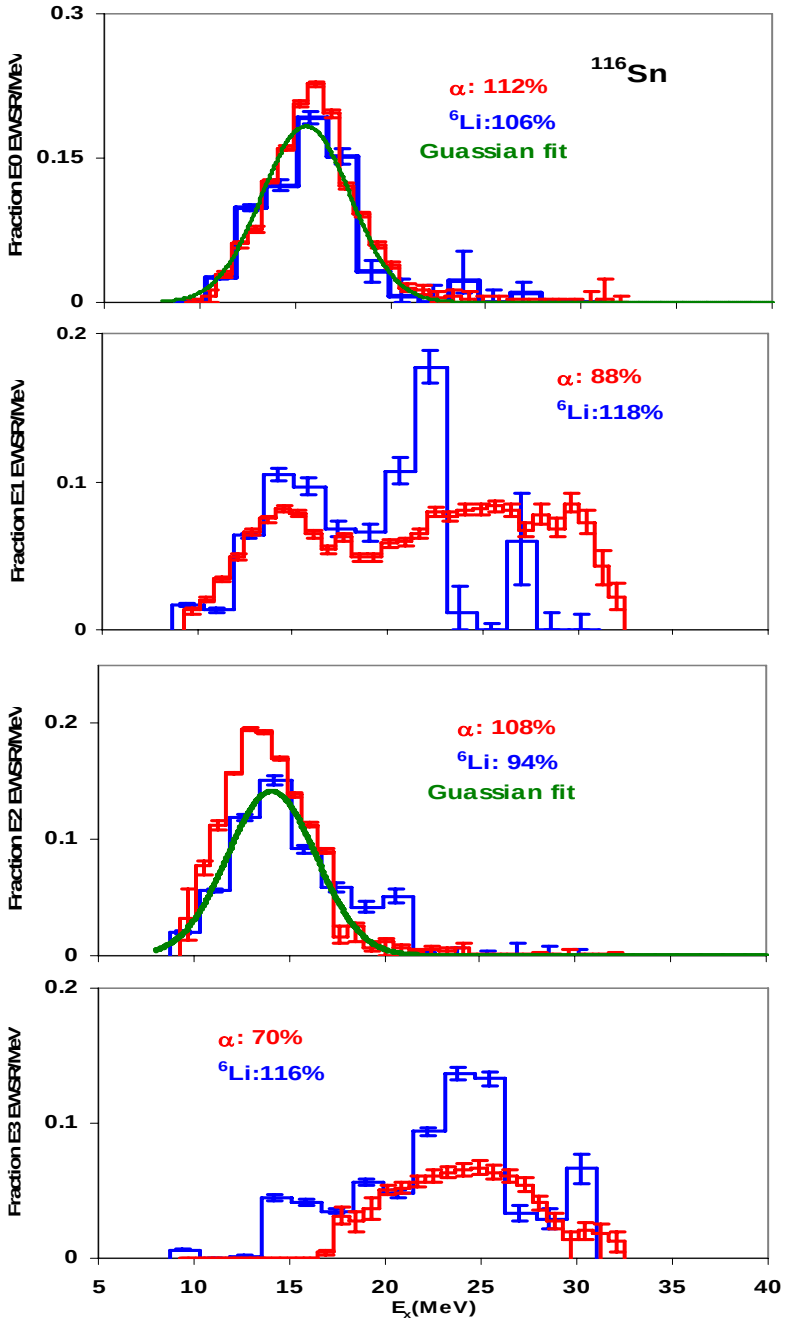

FIG. 4.14 E0, E1, E2 and E3 Strength distributions for ^{116}Sn obtained from analysis of ^{6}Li inelastic scattering (blue curve). The red curve was obtained with α inelastic scattering [49]. Error bars represent the uncertainty due to the fitting of the angular distributions and different choices of the continuum.

The errors for the centroid energy and rms width listed in Table 4.4 were calculated considering the possible error sources shown in Table 4.6. The beam energy uncertainty gives very little error on excitation energy calibration as a 5 MeV difference in beam energy gives a 0.004 MeV difference in kinematic calculations for excitation energy. The standard deviation from the states used to do energy calibration contributes ~ 0.06 MeV of the total error. The error from the energy calibration slope, obtained by varying the minimum χ^2 by unit 1, varies with the excitation energy. The error from uncertainty of the 0^+ state of ^{24}Mg which is used to adjust the energy calibration for 0 degree spectra is around 0.06 MeV. The error caused by choosing different widths of energy bins is ~ 0.1 MeV. The target thickness uncertainty gives about ~0.04 MeV error. All the errors, combined with statistic fitting error, give the total error for each centroid energy and rms width.

Table 4.6 Error estimated for centroid energy and rms width.

error source	excitation energy error (MeV)
beam Energy uncertainty (±5MeV)	0.004
Calibration Standard deviation	0.06
Calibration Slope error	Varied with excitation Energy
^{24}Mg(0^+, 13.86MeV)	0.06
energy bin effect	0.1
target thickness uncertainty	0.04
Statistic fitting error	Varied with centroid energy

The E0 strength distribution obtained in this work corresponds to 106^{+27}_{-11} % of the E0 EWSR with a centroid (m_1/m_0) energy $15.39^{+0.35}_{-0.20}$ MeV and equivalent width $6.10^{+0.85}_{-0.34}$ MeV. The Gaussian fit of the E0 strength distribution gives a centroid of 15.58 ± 0.19 MeV and a width of 5.46±0.18 MeV, which is in good agreement with 112±15% of the E0 EWSR given in Ref. [49] with a centroid of 15.85±0.20 MeV and a width of 5.27±0.25 MeV.

The E2 strength extracted in this work corresponds to 94^{+14}_{-10} % of the E2 EWSR with a centroid energy of $14.34^{+0.26}_{-0.20}$ MeV and an equivalent width $6.90^{+0.78}_{-0.18}$ MeV. The Gaussian

fit of the E2 strength distribution gives a centroid of 14.09±0.27 MeV and a width of 5.48±0.35 MeV, which is in agreement with that given in Ref. [49] which corresponds to 108±12% of the E2 EWSR with a centroid of 13.50±0.35 MeV and a width of 5.00±0.30 MeV, and also in agreement with that given in Ref. [133] which corresponds to 103±10% of E2 EWSR with a centroid energy of 14±0.5 MeV.

The E3 strength extracted in this work corresponds to 116±11% of the E3 EWSR, which is much larger than 70±12% identified in Ref. [49] and 67±10% extracted in Ref. [133]. The centroid energy obtained in this work agrees with that given in Ref. [133] while the equivalent width agrees with that given in Ref. [49].

The ISGDR strength extracted in both ^{6}Li and α scattering is split into two peaks and the position of the lower peaks are similar, but otherwise there are significant differences. The ISGDR strength extracted in this work corresponds to 118^{+20}_{-14} % of the E1 EWSR whereas 88% of the EWSR was identified with α scattering. The strength extracted from ^{6}Li scattering is larger but very little strength is seen above E_x=27 MeV, while significant strength was seen with α scattering above 27 MeV. When fitted with two Gaussians, the low energy peak strength corresponds to 66±10% of the E1 EWSR with a centroid of 15.32±0.20 MeV and a width (FWHM) of $5.56^{+0.20}_{-0.19}$ MeV, the high energy peak strength corresponds to 52^{+20}_{-14} % of the EWSR with a centroid energy of 21.73±0.20 MeV and a width (FWHM) of $2.8^{+0.26}_{-0.28}$ MeV, while, in α scattering [49], the low energy peak corresponds to 25±15% of the E1 EWSR with a centroid of 14.38±0.25 MeV and a width (FWHM) of 5.84±0.30 MeV, the high energy peak corresponds to 61±15% of the EWSR with a centroid energy of 25.50±0.60 MeV and width (FWHM) of 12.0±0.6 MeV. Youngblood *et al*. pointed out in a series of papers [46, 49, 134] that the E1 strength distributions are quite sensitive to continuum choices. The large difference in E1 strength shown here may come from different continuum choices.

4.3 240 MeV ^{6}Li Scattering on ^{28}Si and ^{24}Mg

4.3.1 ^{6}Li Elastic Scattering on ^{28}Si and ^{24}Mg.

The W-S model as well as double folding models were used in analysis of elastic scattering on ^{28}Si and ^{24}Mg. The best fit optical parameters of the W-S potential are listed in Table 4.7. In the folding model analysis, two different *NN* effective interactions (M3Y [73] and JLM [84]) were used to get the folded potential. Folding calculation **I** (FC**I**) used a density dependent M3Y *NN* interaction described in detail by D.T. Khoa [78], while folding calculation **II** (FC**II**) used the JLM effective interaction described by F. Carstoiu *et al.* [135], L. Trache *et al.* [85] and the references in these two papers. Two different density forms, Fermi distribution and Hartree Fork (HF) density [100], were used for the target ground density during the folding procedures (see Table 4.8). The cluster-orbital shell-model approximation [119] form was used for ^{6}Li ground density (see Eq.(4.3)) with FC**I**. FC**I** was carried out with **DFPD4** and elastic scattering data were fitted with **ECIS**. The optical parameters obtained are listed in Table 4.9. FC**II** and the elastic scattering fit were carried out with **OPTJLM1**. HF densities were used for both target and projectile. The optical parameters are listed in Table 4.10. The angular distributions of the cross-sections calculated with different models are plotted along with the data in Fig. 4.15 for ^{24}Mg and Fig. 4.16 for ^{28}Si. Both FC**I** and FC**II** give almost the same quality fits for each nucleus.

Table 4.7 Optical parameters obtained from analysis of ^{6}Li elastic scattering on ^{28}Si and ^{24}Mg with the W-S potential.

Target	V (MeV)	r_0 (fm)	a (fm)	W (MeV)	r_{i0} (fm)	a_i (fm)	J_v (MeVfm^3)	J_w (MeVfm^3)	σ_r (mb)	χ^2
^{28}Si	143.34	0.720	0.937	32.13	1.004	0.921	261.18	125.40	1650	1.43
^{24}Mg	114.52	0.762	0.879	34.518	0.956	1.027	244.4	138.2	1680	1.14

Table 4.8 Density parameters for different density choices. Den1 and Den2 are Fermi distributions. R_p, R_n, R_m, R_{ch} means the root mean square radii of the calculated proton, neutron, mass and charge distributions respectively.

target	Density choice	ρ_0 (fm)	C (fm)	A (fm)	R_p (fm)	R_n (fm)	R_m (fm)	R_{ch} (fm)
^{24}Mg	Den1[18]	0.17	2.995	0.478	2.922	2.922	2.922	3.040
	Den2[19]	0.166	2.979	0.523	3.017	3.017	3.017	3.040
	HF	–	–	–	2.928	2.906	2.917	3.000
^{28}Si	Den1[18]	0.175	3.15	0.475	3.010	3.010	3.010	3.875
	Den2[19]	0.167	3.155	0.523	3.123	3.123	3.123	3.154
	HF	–	–	–	3.059	3.031	3.045	3.132

Table 4.9 Optical model parameters obtained from fits of elastic scattering with folding calculation **I**. N_r is the renormalization factor for the real potential. S_r is the scaling factor for the real potential radius. W, r_{i0}, a_i are W-S parameters for the imaginary potentials. J_v and J_w are the volume integral per nucleon pair for the real and imaginary potentials respectively. σ_r is the total reaction cross section.

Target	N-N int	Target density	N_r	S_r	W (MeV)	r_{i0}(fm)	a_i(fm)	J_v (MeVfm^3)	J_w (MeVfm^3)	σ_r (mb)	χ^2
^{24}Mg	CDM3Y6	Den1	0.824	1.062	58.7	0.731	1.204	242	154	1799	1.038
	CDM3Y5	Den1	0.823	1.062	58.67	0.731	1.204	242	154	1799	1.039
	CDM3Y4	Den1	0.822	1.062	58.73	0.7311	1.204	242	154	1799	1.039
	CDM3Y5	HF	0.766	1.055	59.14	0.728	1.208	240	155	1803	1.042
	CDM3Y5	Den2	0.846	1.079	57.92	0.737	1.198	242	154	1793	1.032
^{28}Si	CDM3Y5	Den1	0.887	1.0624	41.33	0.9049	1.048	256	136	1757	1.461
	CDM3Y5	Den2	0.924	1.083	41.38	0.9049	1.046	258	136	1755	1.439
	CDM3Y5	HF	0.933	1.059	41.85	0.9011	1.051	257	137	1761	1.485

Table 4.10 Optical potential parameters obtained from the fit of elastic scattering with folding calculation **II** .N_r and N_w are the normalization factor for the real and imaginary potential respectively. t_r and t_w are range parameters for the real and imaginary potential respectively.

Target	N-N int.	target density	N_r	t_r (fm)	N_w	t_w (fm)	J_v (MeVfm^3)	J_w (MeVfm^3)	σ_r (mb)	χ^2
^{24}Mg	JLM	HF	0.519	0.9559	0.862	2.586	237	144	1803	1.6
^{28}Si	JLM	HF	0.546	0.9165	0.825	2.4275	248	137	1734	1.94

A scaling factor on the radius of the real optical potential is necessary to fit the elastic scattering for both ^{24}Mg and ^{28}Si when FC**I** is used. Different density choices (as shown in Table 4.8) will slightly change the value of the scaling factor (as shown in Table 4.9.), but do not eliminate the factor. Different types of density dependent M3Y interactions such as CDM3Y4, CDM3Y5, CDM3Y6 (see Table 2.1) give almost the same scaling factors for ^{24}Mg elastic scattering. One possible reason for this factor could be the density used in the density dependent function. The density is defined as the sum of the densities of target and projectile, which may over-estimate the nuclear matter density in certain regions. The fit to elastic scattering with the JLM folding calculation does not need the scaling factor on the radius. However there is an adjustable smearing factor **t** in the smearing function which greatly increases the ability of the folding form factor to simulate the radial dependence of DPP [135]. FC**I** was used to analyze inelastic scattering for convenience, because **DFPD4** can generate the transition density for inelastic scattering and calculate the transition potentials.

The volume integrals of real parts of the optical potentials for ^{6}Li scattering on ^{28}Si and ^{24}Mg were calculated for each of the potentials obtained. The difference of the volume integrals obtained for ^{28}Si with different models is less than 13 MeV·fm^3 while the difference for ^{24}Mg is less than 5 MeV·fm^3. The results are shown and compared with Nadasen *et al*.'s expression, Gupta and Murthy's expression and Satchler's expression in Fig. 4.17. The volume integrals obtained with different models for ^{28}Si are consistent with or close to Nadasen *et al*.'s prediction and Gupta and Murthy's prediction, while the volume integrals for ^{24}Mg lie below these two predictions and above Satchler's prediction. (note: Since Satchler's prediction is based on the different target and projectile systems[121], as large as 50 MeVfm^3 uncertainty was found in previous folding model analysis of 210 MeV ^{6}Li scattering [120]).

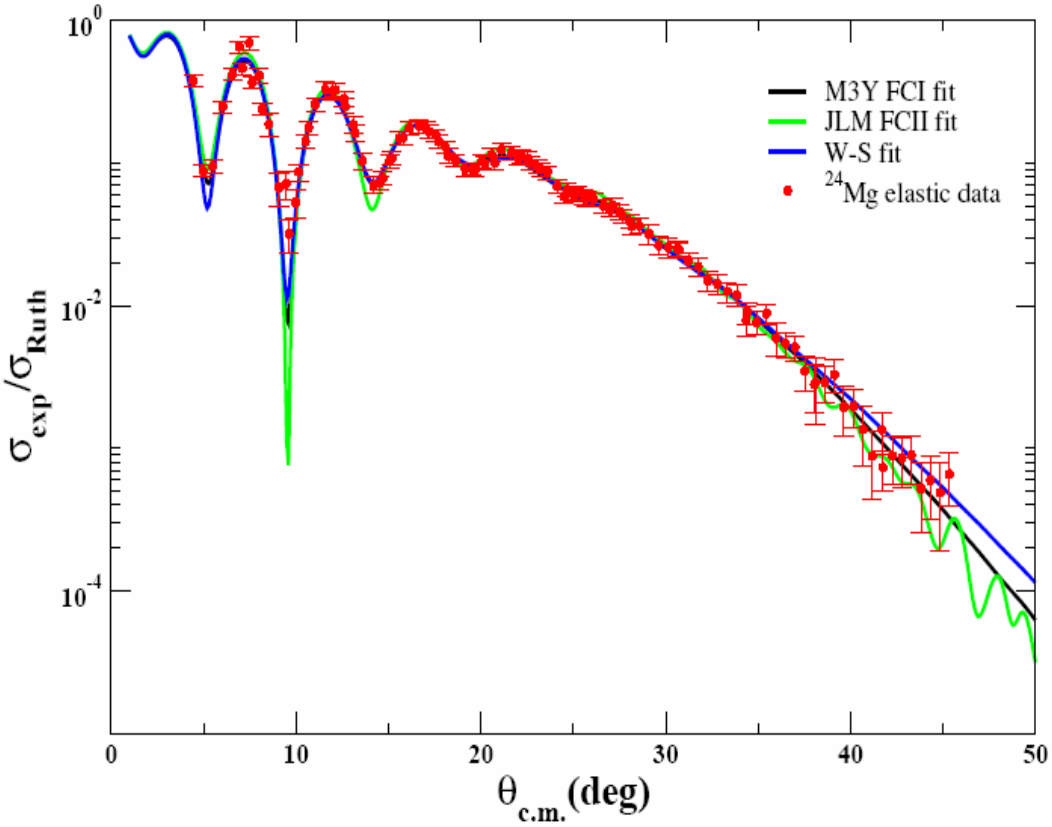

FIG. 4.15 Experimental angular distribution of the cross-section (relative to Rutherford cross section) and fits for ^{6}Li + ^{24}Mg elastic scattering using W-S potential (blue curve), folding potential with CDM3Y6 NN interaction (black curve) and folding potential with JLM NN interaction (green) are shown. The error bars indicate statistical and systematic errors.

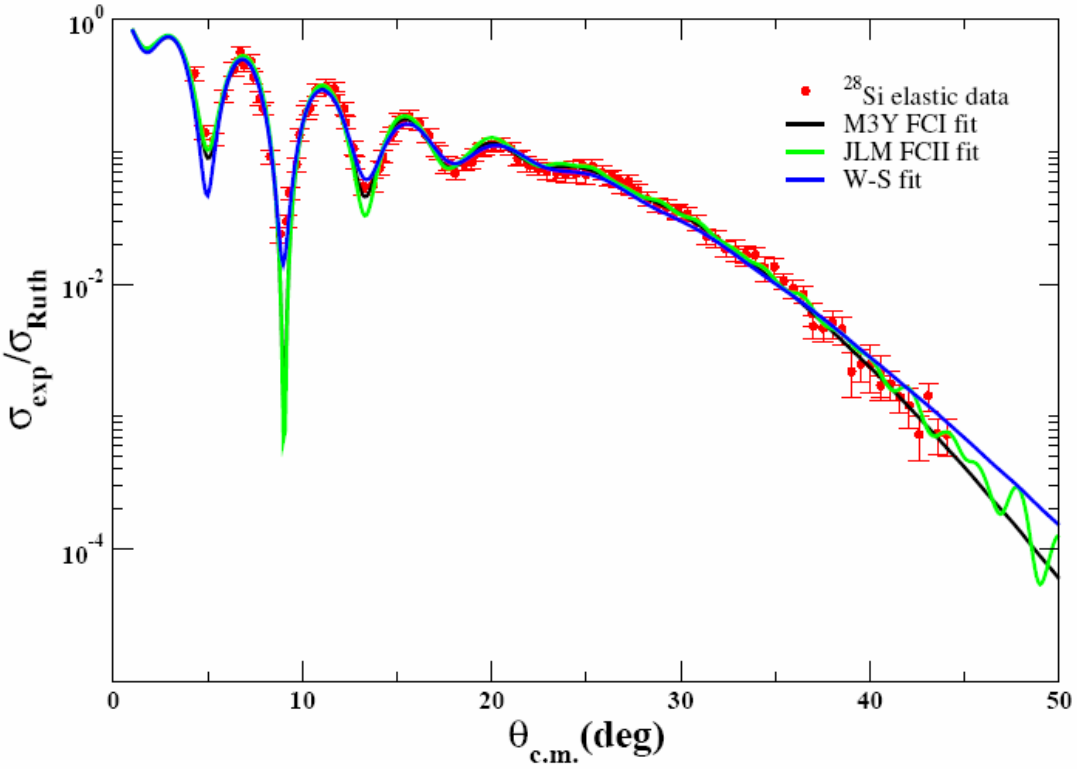

FIG. 4.16 Experimental angular distribution of the cross-section (relative to Rutherford cross section) and fits for ^{6}Li + ^{28}Si elastic scattering using W-S potential (blue curve), folding potential with CDM3Y5 NN interaction (black curve) and folding potential with JLM NN interaction (green) are shown. The error bars indicate statistical and systematic errors.

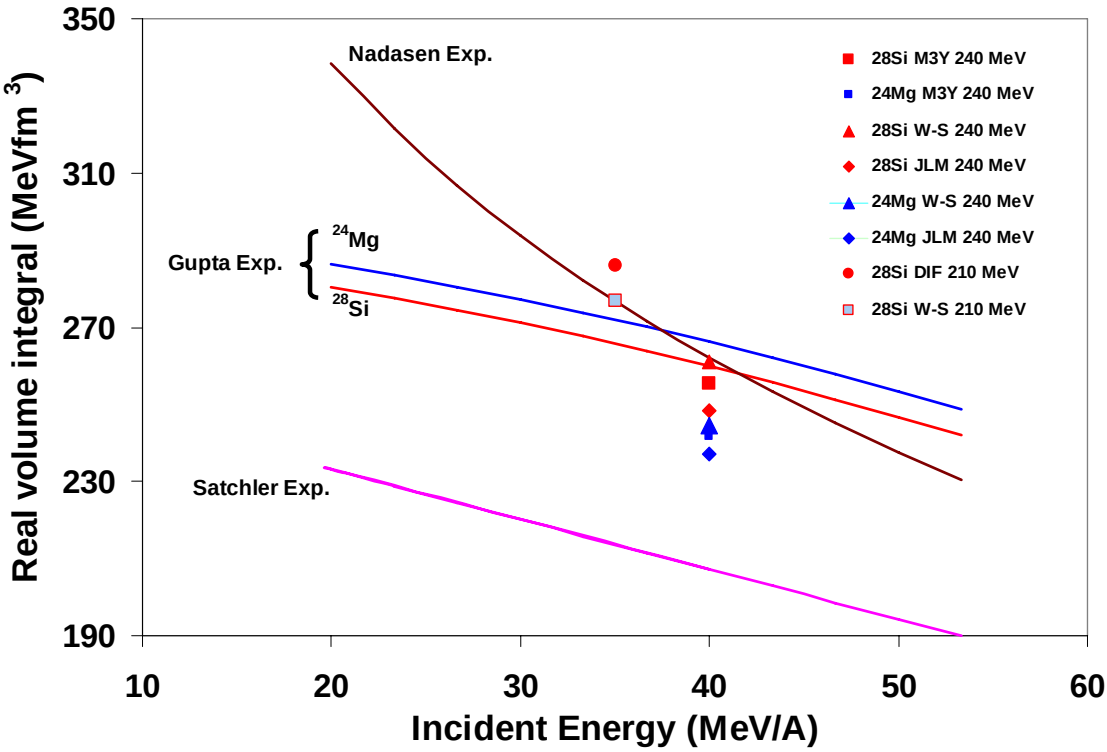

FIG. 4.17 The volume integral of the real part of the optical potential for ^{6}Li scattering on ^{28}Si and ^{24}Mg obtained with W-S model, folding model with JLM and M3Y effective NN interactions. The brown curve represents Nadasen *et al.*'s expression obtained with W-S potential [16]. The blue and red curves represent Gupta and Murthy's expression for ^{24}Mg and ^{28}Si obtained with JLM effective interaction [40]. The pink curve represents Satchler's expression obtained with S1Y effective NN interaction [27]. Volume integrals obtained from Ref. [8] for 210 MeV ^{6}Li scattering on ^{28}Si are also plotted in the figure for comparison.

DWBA calculations for ^{6}Li inelastic scattering to the low-lying 2^{+} state of ^{24}Mg and to low-lying 2^{+} and 3^{-} states of ^{28}Si were carried out with the optical parameter sets obtained by deformed potential model and folding model **I**. The CDM3Y5 density dependent NN interaction was used here and the Den1 form (as shown in Table 4.8) was chosen as the target density for both ^{24}Mg and ^{28}Si. The transition potentials were

calculated with DFPD4 and the cross sections were calculated with ECIS. The mass deformation parameters for the 2^+ and 3^- states were obtained from electromagnetic B(EL) values by assuming that the mass and coulomb deformation lengths are the same. The best fit B(EL) values for the 2^+ and 3^- states of ^{28}Si and the 2^+ state of ^{24}Mg were extracted by fitting the inelastic scattering cross section and are listed in Table 4.11. The fitted B(E2) values obtained for the ^{28}Si 2^+ state and ^{24}Mg 2^+ state obtained with the folding model calculations agree with the adopted value and with the value from electron scattering. The fitted B(E3) value for the ^{28}Si 3^- state does not agree with the adopted value, but it agrees with the value from electron scattering [136]. The B(EL) values obtained with the deformed potential model are all smaller than the adopted value or the value from electron scattering. This is consistent with Beene *et al.*'s conclusion [137]. The calculated angular distribution for the 2^+ state in ^{24}Mg is plotted in Fig. 4.18 along with the data. The calculated angular distributions for 2^+ and 3^- states of ^{28}Si are plotted in Fig. 4.19 and Fig. 4.20 respectively along with data.

Table 4.11 The best fit B(EL) values for 2+ and 3- states of ^{28}Si and 2+ state of ^{24}Mg obtained with the deformed potential model and the double folding model. Adopted values of B(E2) and B(E3), as well as values extracted from electron scattering, are shown in the table. For B(EL) values obtained from ^{6}Li scattering, the superscript errors represent statistical errors, while the subscript errors represent total errors including statistical and systematic errors.

Work	Model	^{28}Si $J^\pi=2^+$, E_x=1.779MeV B(E2)(e^2b^2)	^{28}Si $J^\pi=3^-$, E_x=6.888 MeV B(E3)(e^2b^3)	^{24}Mg $J^\pi=2^+$, E_x=1.369 MeV B(E2)(e^2b^2)
Present	DP	$0.0229^{\pm0.0003}_{\pm0.0023}$	$0.00135^{\pm0.00002}_{\pm0.00014}$	$0.0317^{\pm0.0004}_{\pm0.0032}$
	DDF	$0.0318^{\pm0.0004}_{\pm0.0032}$	$0.00311^{\pm0.00005}_{\pm0.00031}$	$0.0465^{\pm0.0006}_{\pm0.0047}$
electron scattering	EM	0.0337±0.0030[138]	0.00387±0.00075[136]	0.0420±0.0025[139]
	Adopted Value	0.0326±0.0012 [127]	0.0042±0.0005[127]	0.0432±0.0011[128]

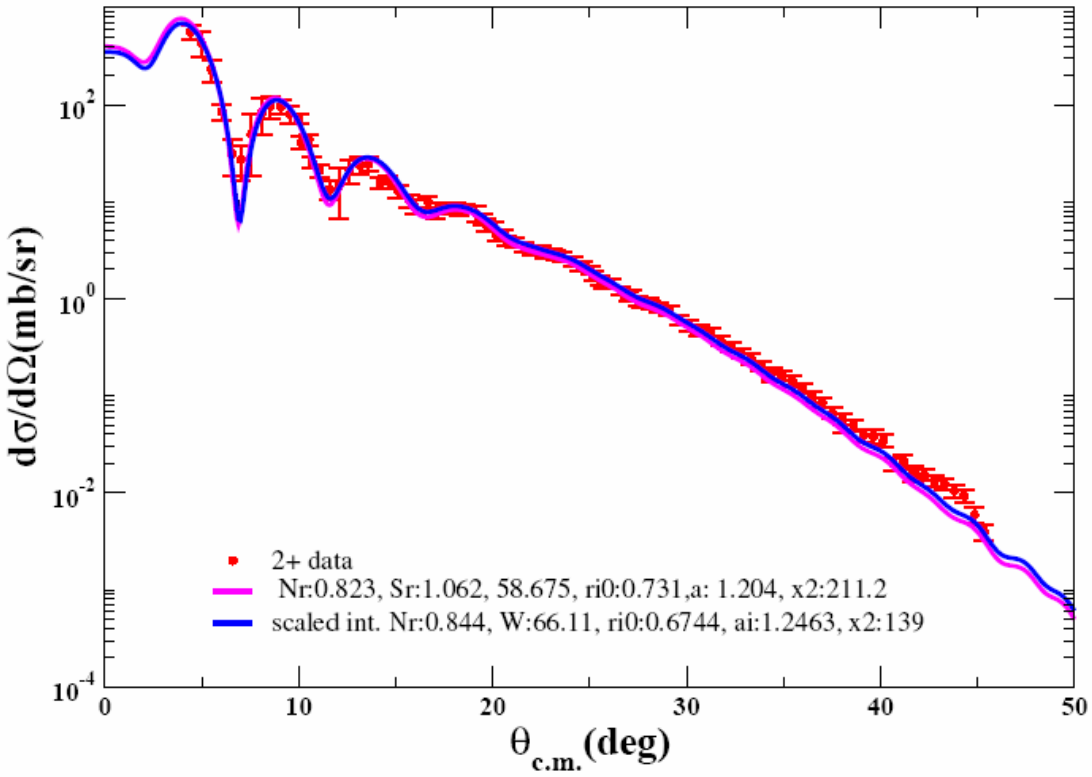

FIG. 4.18 The angular distributions of the differential cross sections for inelastic scattering to the 2^+ state of ^{24}Mg calculated with different scaled potentials along with the data points are plotted versus average center of mass angle. The pink curve shows the one with the potential scaled on radius and the blue curve represents the one scaled on density and M3Y NN effective interaction. The B(E2) value used was 0.0432 e^2b^2. [127].

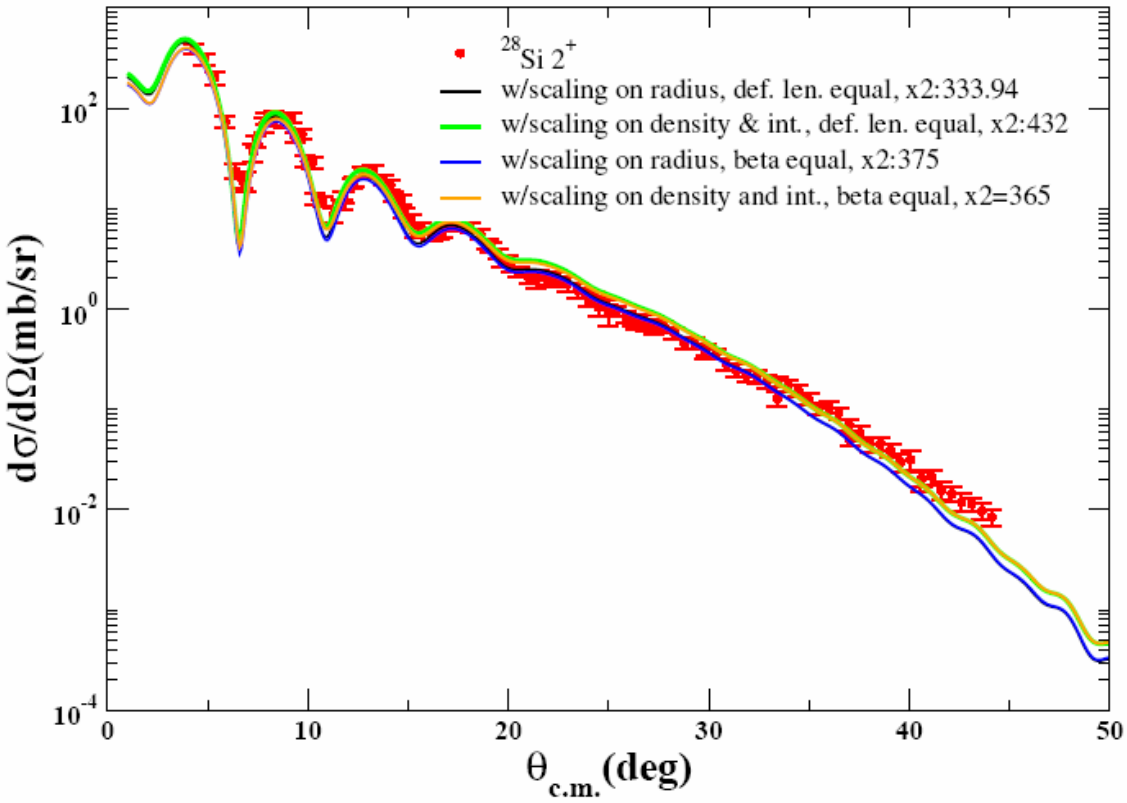

FIG. 4.19 The angular distributions of the differential cross sections for inelastic scattering to the low-lying 2^+ state of ^{28}Si with different scaled potentials along with the data points are plotted versus average center of mass angle. The black curve shows the result when the radius of the potential is scaled and the green curve shows the result when the density and the M3Y NN effective interaction are scaled, both calculations using the same **deformation length δ** for the real and imaginary potential. The blue curve shows the result when the radius of the potential is scaled and the orange curve shows the result when the density and the M3Y NN effective interaction are scaled, both calculations using the same **deformation parameter β** for the real and imaginary potential. The B(E2) value used was 0.0326 e^2b^2 [127].

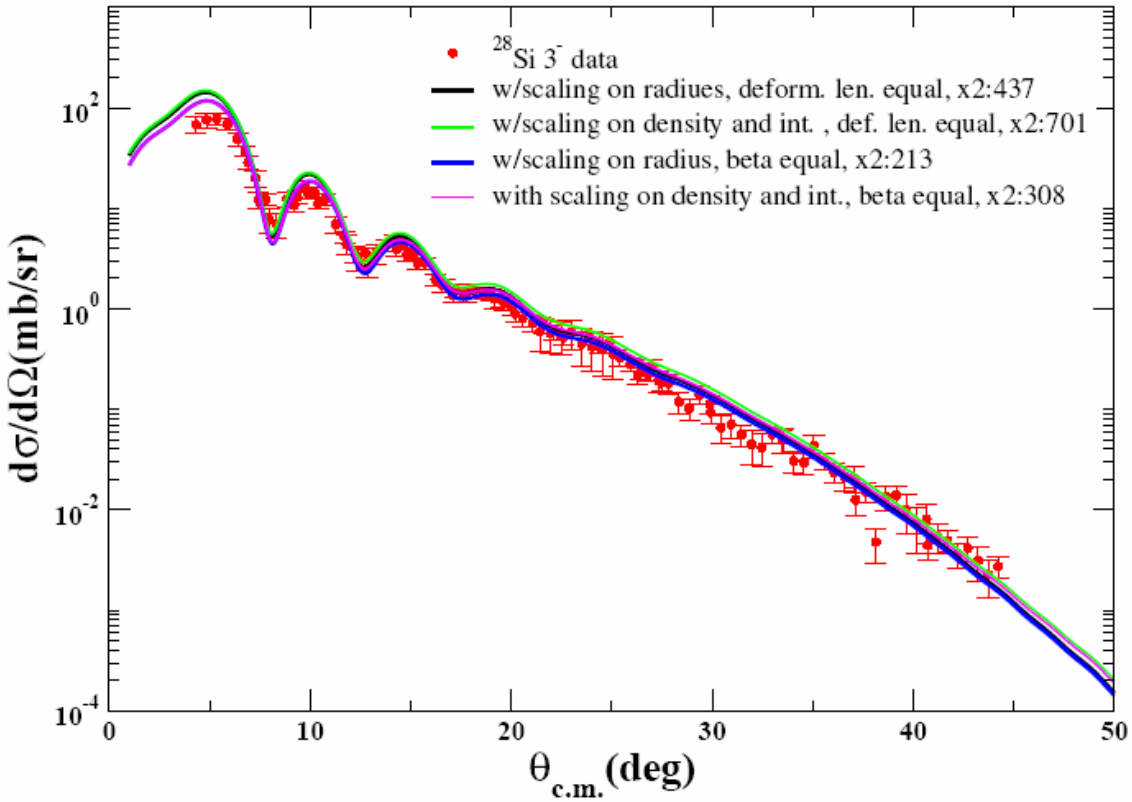

FIG. 4.20 The angular distributions of the differential cross sections for inelastic scattering to the low-lying 3$^-$ state of ^{28}Si calculated with different scaled potentials along with the data points are plotted versus average center of mass angle. The black curve shows the result when the radius of the potential is scaled and the green curve shows the result when the density and the M3Y NN effective interaction are scaled, both calculations using the same **deformation lengths δ** for the real and imaginary potential. The blue curve shows the result when the radius of the potential is scaled and the pink curve shows the result when the density and the M3Y NN effective interaction are scaled, both calculations using the same **deformation parameter β** for the real and imaginary potentials. The B(E3) value used was 0.0042 e^2b^3 [128].

One assumption made in the DWBA calculations with ECIS for low-lying states of ^{28}Si and ^{24}Mg was that the input real folded transition potentials had the same scaling factor on radius as the real folded optical potentials do. There is no justification for doing this. The scaling effect on inelastic scattering data analysis was further investigated by scaling the parameters of M3Y NN effective interactions, the parameters of the target and projectile, instead of scaling the radius. The folded potential and transition potential for ^{6}Li scattering on ^{24}Mg and inelastic scattering to the 2^{+} state at 1.369 MeV were calculated with scaling on the density and the effective interaction. Then it was compared with those potentials scaled on radius (see Fig. 4.21). Although the peak values of the potentials are different, the potentials obtained with scaled density and NN interaction and the potentials with scaled radius overlap well in the surface range. The angular distribution of the differential cross sections for inelastic scattering to the 2^{+} state of ^{24}Mg was calculated with scaled potentials and the results are shown in figure 4.18. Those for inelastic scattering to low-lying 2^{+} and 3^{-} states of ^{28}Si were also calculated and shown in Fig. 4.19 and Fig. 4.20. All the calculations show that the scaling on density and effective interaction gives almost the same quality of agreement with the data as scaling on the radius of the potential. So for convenience the potentials scaled on the radius were used in analysis of giant resonance data.

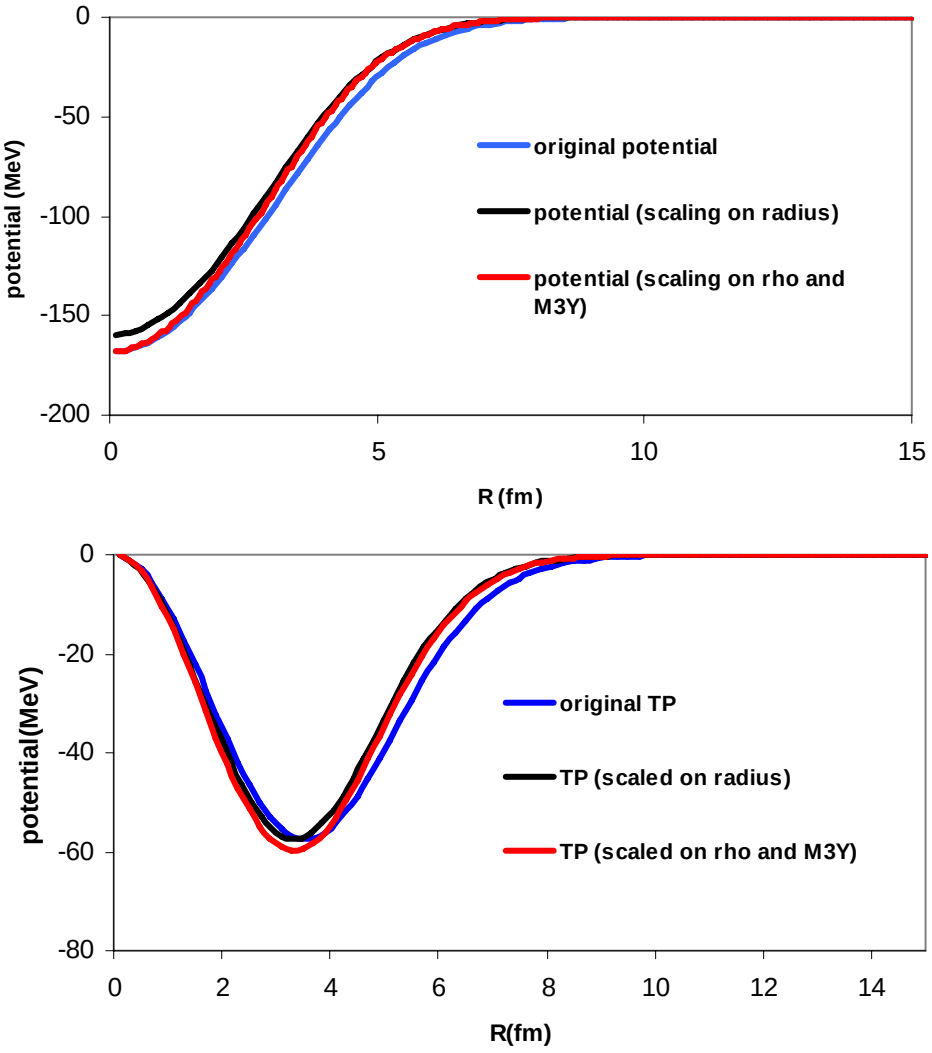

FIG. 4.21 The upper figure shows the original potential, potential scaled on radius, and potential scaled on density and M3Y effective interaction for ^{6}Li elastic scattering on ^{24}Mg. The lower figure shows the transition potential (TP) obtained from **DFPD4**, TP scaled on radius and the TP scaled on density and M3Y effective interaction for ^{6}Li inelastic scattering to 2^{+} 1.369 MeV state of ^{24}Mg.

4.3.2 Analysis of ^{6}Li Inelastic Scattering on ^{28}Si

Inelastic scattering of ^{6}Li from ^{28}Si excited into the giant resonance region was measured with the spectrometer at 0° and 4°. The data analysis procedure was described in SECTION 4.1. The folding optical potential obtained with the CDM3Y5 NN interaction and with density den1 (as shown in Table 4.9) were used to analyze ^{28}Si giant resonance data. Sample excitation energy spectra for ^{28}Si with average center of mass angles 1.3° and 6.4° are shown in Fig. 4.22 with pink curves representing the continuum choices. Angular distributions of differential cross sections for the giant resonance peak and background are shown in Fig. 4.23 along with DWBA fits for three energy bins with average excitation energies 10.14 MeV, 20.46 MeV and 29.14 MeV.

The E0, E1, E2 and E3 strength distributions obtained are shown in Fig. 4.24 along with those obtained from α scattering. The multipole parameters obtained for ^{28}Si are summarized and compared with those from α scattering in Table 4.12. The centroid, (m1/m0), rms width and percentage of the EWSR are calculated for the total excitation range measured (8 to 40 MeV), as well as the ranges 8 to 22.4 MeV and 22.4 to 40 MeV.

The E0 strength distribution extracted in this work agrees well with that obtained from α scattering[40] (see Fig. 4.24). The strength extracted for total excitation range corresponds to 80^{+35}_{-20} % of the E0 EWSR with a centroid of $20.59^{+0.78}_{-0.33}$ MeV and an rms width $5.78^{+1.34}_{-0.34}$ MeV, in good agreement with that observed in α scattering which corresponds to 74±10% of the E0 EWSR with a centroid of 21.46±0.38 MeV and an rms width 6.3±0.6 MeV (Note: 74±10% was obtained fitting only the GR peak in α scattering , and an additional 7% was obtained in the continuum fit resulting in 81±10% of the E0 EWSR as shown in Ref. [40]).

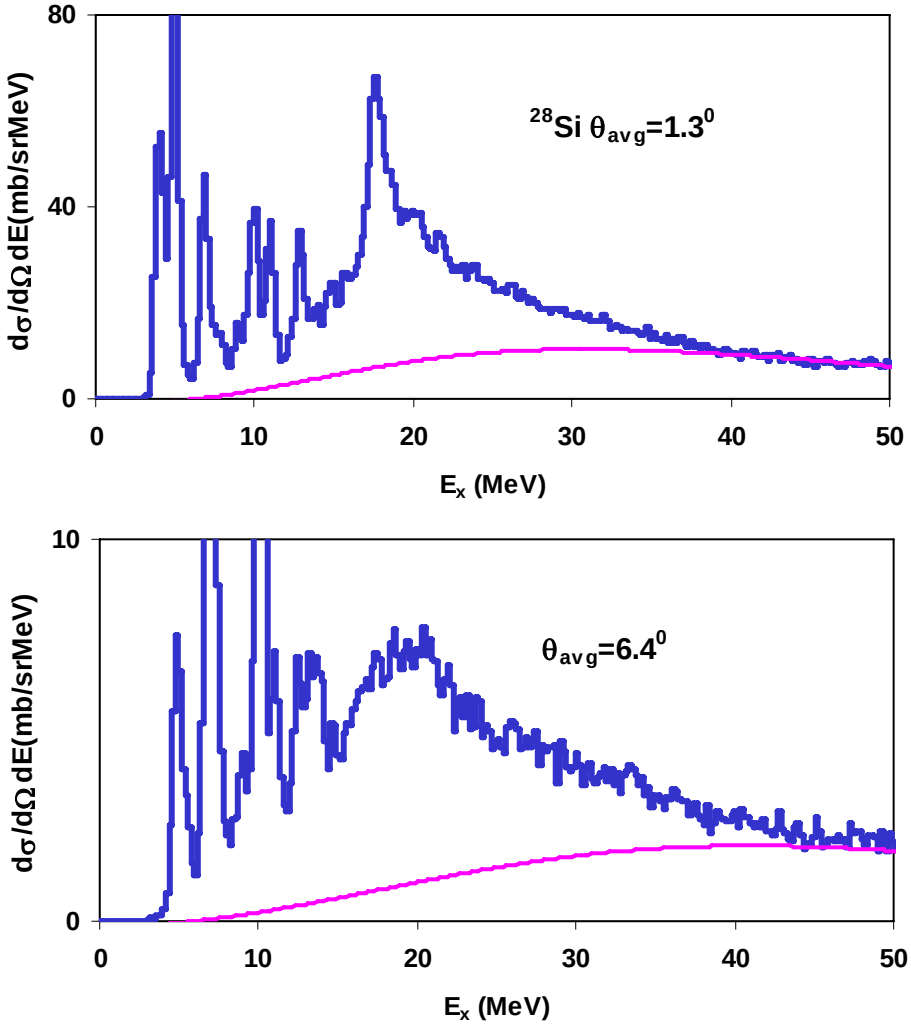

FIG. 4.22 Sample spectra for ^{28}Si at average center of mass angle 1.3° and 6.4°. The pink curves are the continuum chosen for the analysis.

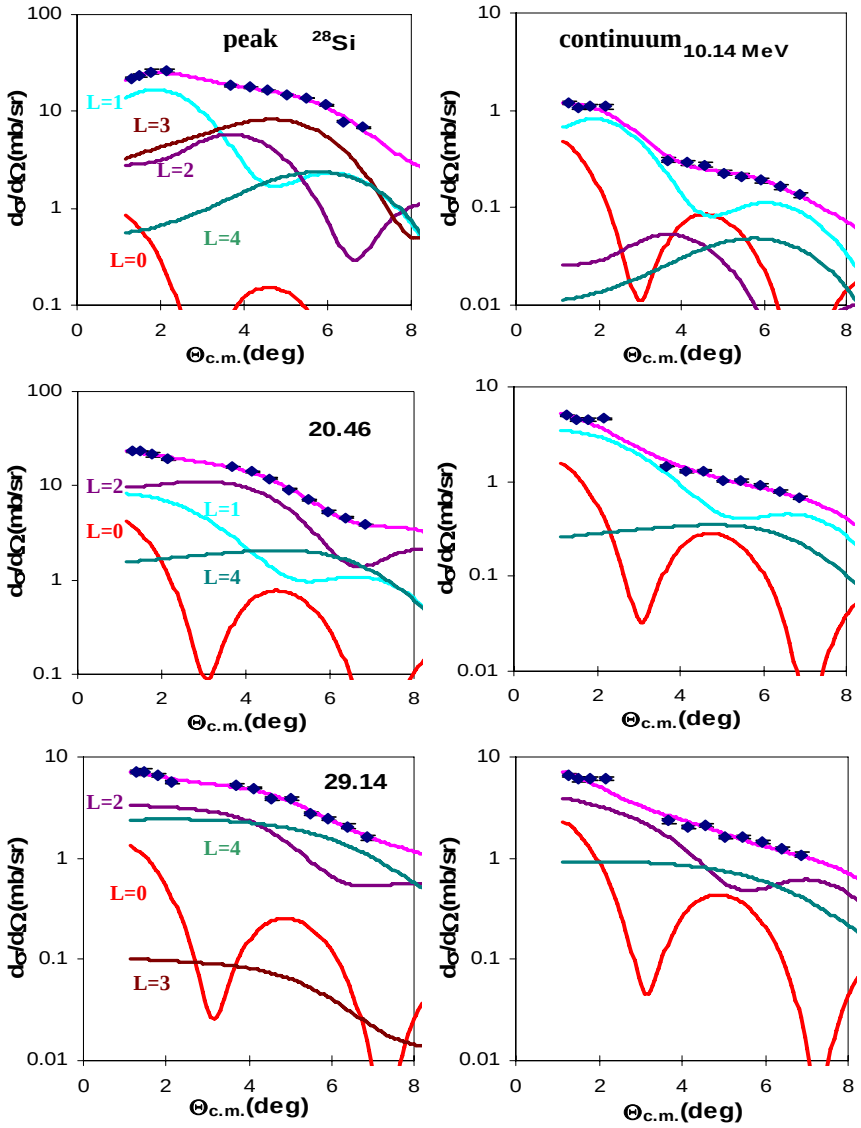

FIG. 4.23 Angular distributions of the cross section for ^{6}Li inelastic scattering from ^{28}Si for 0.8 MeV wide bins centered at E_x=10.14, 20.46, 29.14 MeV along with DWBA fits. The left column shows those for the giant resonance peak while the right column shows those for the continuum. The pink lines through the data show the fits. The E0 contribution is shown by the red line, the isoscalar E1 contribution by the light blue line, the E2 contributions by the purple lines, the E3 contributions by the brown lines and E4 contributions by the dark green lines.

Table 4.12 Multipole parameters obtained for ^{28}Si in this work compared to those obtained from analysis of α scattering.

	This work				α scattering [40]			
	E_x range (MeV)	m_1/m_0 (MeV)	rms width (MeV)	EWSR (%)	E_x range (MeV)	m_1/m_0 (MeV)	rms width (MeV)	EWSR (%)
E0	8.0-22.4	17.60±0.17	2.67±0.17	48±6	8.0-22.5	17.27±0.38	3.04±0.6	38±4
	22.4-40.0	$27.72^{+0.73}_{-0.25}$	$3.21^{+1.34}_{-0.34}$	31^{+30}_{-13}	22.5-40.0	28.22±0.38	3.75±0.6	37±4
	8.0-40.0	$20.59^{+0.78}_{-0.33}$	$5.78^{+1.34}_{-0.34}$	80^{+35}_{-20}	8.0-40.0	$21.46^{+0.38}_{-0.38}$	6.3±0.6	74±10
E1	8.0-22.4	16.9±0.17	$3.77^{+0.74}_{-0.19}$	40±4	8.0-22.5	15.3±0.60	4.75±0.7	8±0.8
	22.4-40.0	$27.27^{+0.34}_{-0.20}$	$2.69^{+0.74}_{-0.19}$	38^{+19}_{-10}	22.5-40.0	27.56±0.60	3.05±0.7	7±0.7
	8.0-40.0	$21.17^{-0.41}_{-0.24}$	$5.87^{+0.74}_{-0.19}$	84^{+21}_{-11}	8.0-40.0	19.27±0.60	6.9±0.7	15±4
E2	8.0-22.4	17.25±0.17	3.02±0.23	47±5	8.0-22.5	16.59±0.25	3.5±0.6	47±5
	22.4-40.0	$29.22^{+0.20}_{-0.19}$	3.81±0.23	64±6	22.5-40.0	27.21±0.25	2.98±0.6	18±2
	8.0-40.0	$22.69^{+0.23}_{-0.20}$	6.94±0.23	111±16	8.0-40.0	18.53±0.25	4.7±0.6	65±9
E3	8.0-22.4	$12.94^{+0.25}_{-0.19}$	6.54±0.18	4^{+5}_{-1}	8.0-22.5	13.31±0.25	4.57±0.6	7±0.7
	22.4-40.0	32.15±0.17	4.48±0.18	27±3	22.5-40.0	33.32±0.25	3.48±0.6	3±0.3
	8.0-40.0	27.71±0.24	8.09±0.18	31^{+7}_{-6}	8.0-40.0	16.3±0.25	9.22±0.6	10±1

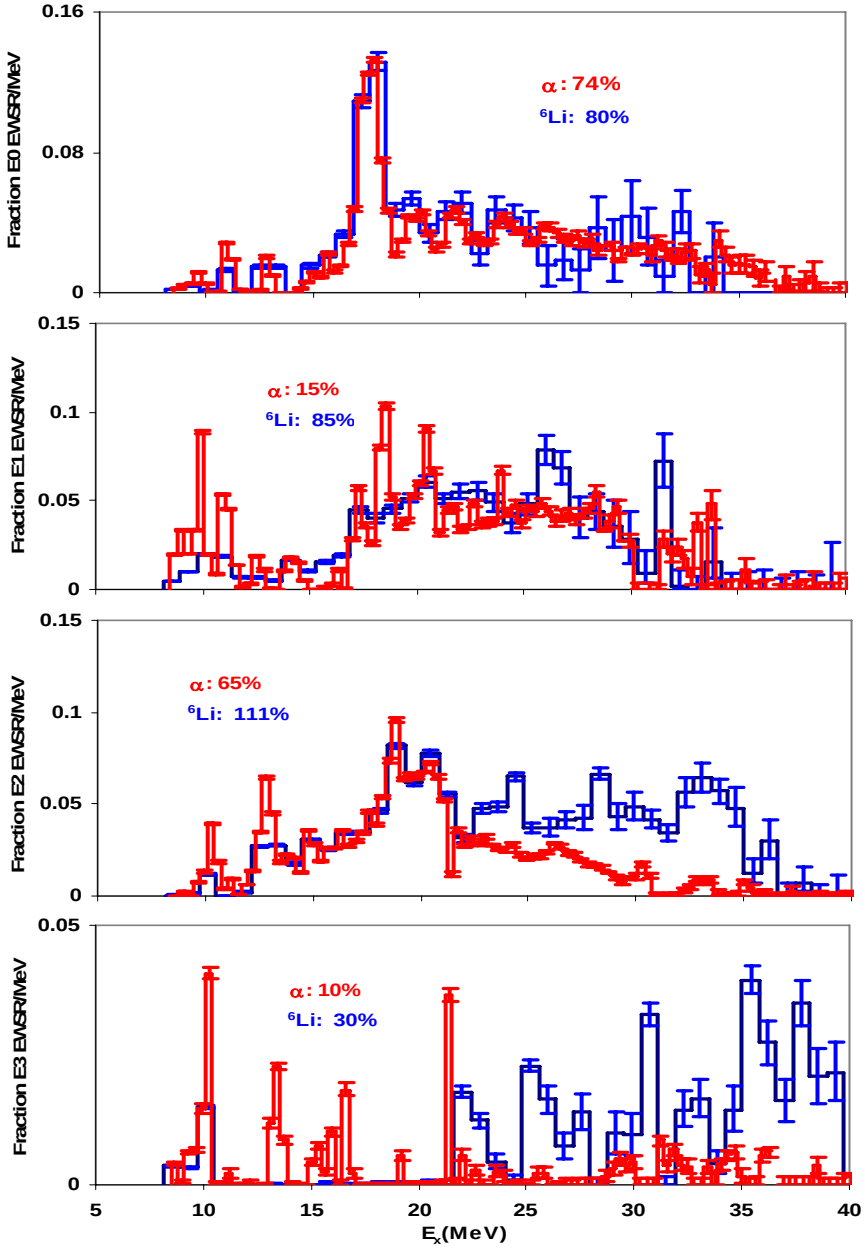

FIG. 4.24 The dark blue curves show E0, E1, E2 and E3 strength distributions for ^{28}Si obtained from analysis of ^{6}Li inelastic scattering. The red curves show those obtained with α inelastic scattering [40]. Error bars represent the uncertainty due to the fitting of the angular distributions and different choices of the continuum.

The E2 strength extracted for 8 MeV < E_x < 22.4 MeV in this work corresponds to 47±5% of the E2 EWSR with a centroid of 17.25± 0.17 MeV and an rms width 3.02±0.23 MeV, in good agreement with that obtained from α scattering corresponding to 47±5% of the E2 EWSR with a centroid of 16.59±0.25 MeV and an rms width of 3.5±0.6 MeV. Above 22 MeV, however, the E2 strength extracted from ^{6}Li scattering is higher than that obtained from α scattering, 64±6% of the E2 EWSR compared to 18±2% given in Ref.[40].

A total of 84^{+21}_{-11} % of the E1 EWSR was identified in this work whereas only 15±4% was identified in α scattering and there is a peak around 26.0 MeV which dose not show up in α scattering. The total strength obtained corresponds to 84^{+21}_{-11} %, which is much higher than 15±4% given in Ref.[40]. However, it is interesting to note that, if the strength obtained from α scattering is multiplied by a factor of 5.2, its overall profile overlaps well with that obtained in this work (see Fig. 4.25).

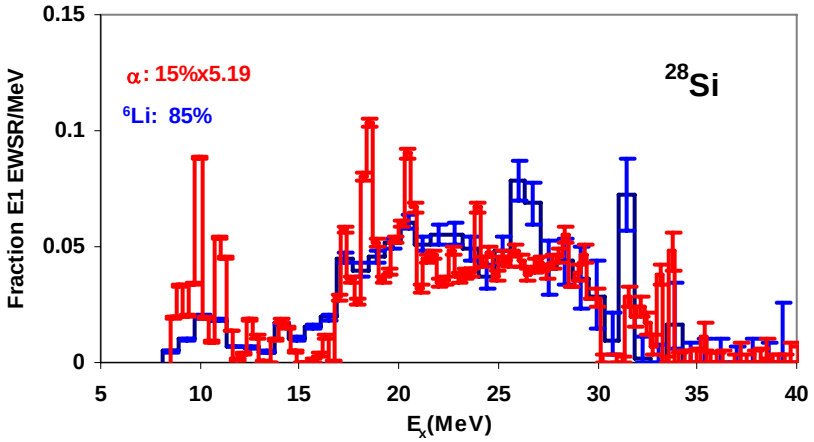

FIG. 4.25 The E1 strength distribution obtained from analysis of ^{6}Li scattering compared to that obtained from analysis of α scattering [40] multiplied by a factor of 5.20.

E3 strength corresponding to only about 30% of the E3 EWSR was identified, most above 22 MeV,-compared to that observed in α scattering [40] corresponding to 10% of the E3 EWSR, most of which was below E_x = 22 MeV.

In the most recent paper on ^{28}Si, Youngblood *et al*. [134] reported a new analysis of α inelastic scattering data with the assumption that all of the cross sections are due to multipole processes in the excitation range E_x < 42 MeV. No continuum was subtracted. The analysis showed that E0 strength extracted is only weakly dependent on the assumption made about the continuum. The E0 strength obtained, 74 ± 7% of the E0 EWSR, the centroid energy (m_1/m_0) 20.89 ± 0.38 MeV and rms width 5.9 ± 0.6 MeV all agree within the errors with those from Ref.[40] and from this work (see Fig. 4.26). For other multipolarities, especially for E1 excitation, the continuum choice does affect considerably the strength extracted. E2 strength reported in that paper corresponding to 102±11% of the E2 EWSR with a centroid of 18.77±0.35 MeV and rms width of 5.45±0.20 MeV, contrasts sharply with results of Ref. [40] (see Fig. 4.27). The percentage of E2 EWSR reported in that paper agree with 111±16% extracted in ^{6}Li scattering, but not much strength was seen from ~27< E_x < 35 MeV(see Fig. 4.27). The E3 strength reported in that paper corresponding to 81±8% of the E3 EWSR between 23 and 39 MeV, and is much higher than that extracted in this work (see Fig. 4.28).

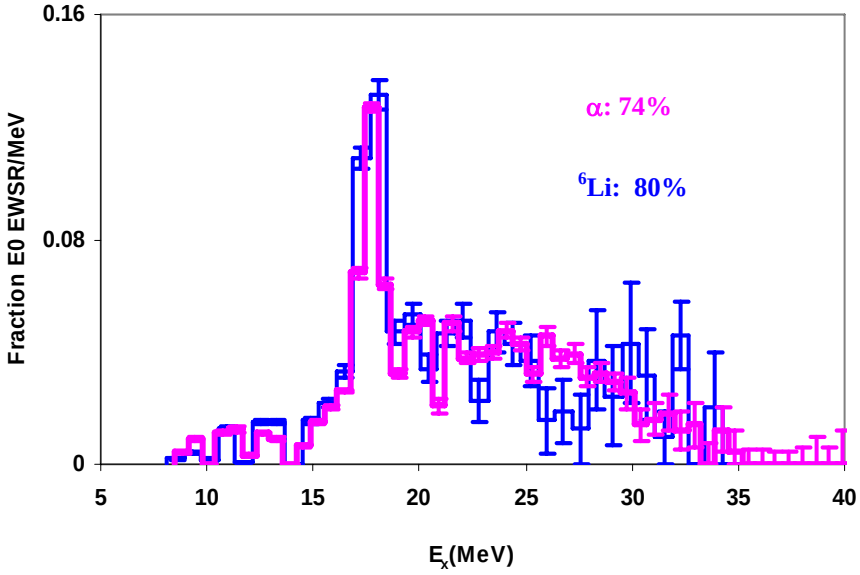

FIG. 4.26 E0 strength distribution obtained from analysis of ^{6}Li scattering compared to that obtained from analysis of α scattering without continuum subtraction[134] (pink curve).

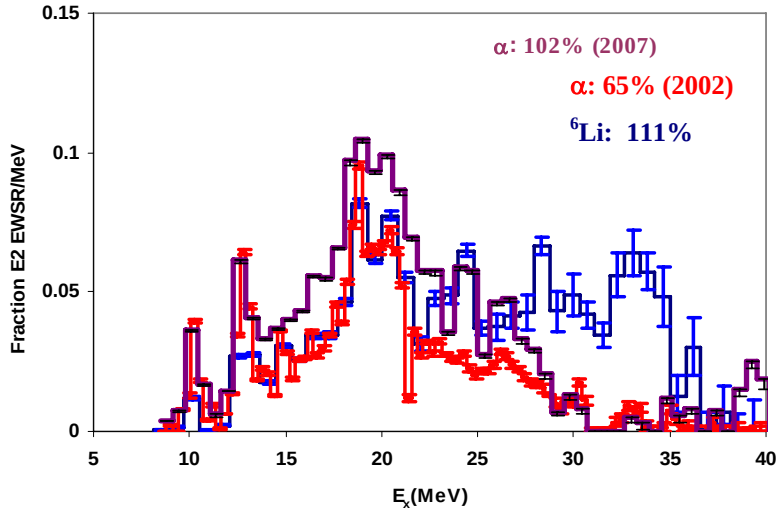

FIG. 4.27 E2 strength distribution obtained from analysis of ^{6}Li scattering compared to those obtained from analysis of α scattering without continuum subtraction [134] (purple curve) and with continuum subtraction [40] (red curve).

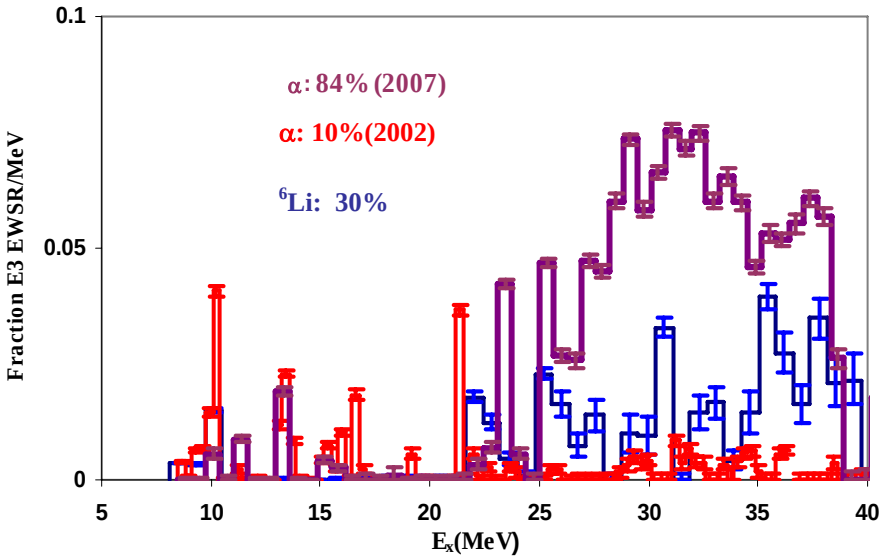

FIG. 4.28 E3 strength distribution obtained from analysis of ^{6}Li scattering compared to those obtained from analysis of α scattering without continuum subtraction [134] (purple curve) and with continuum subtraction[40] (red curve).

4.3.3 Analysis of ^{6}Li Inelastic Scattering on ^{24}Mg

Inelastic scattering of ^{6}Li from ^{24}Mg excited into the giant resonance region was measured with the spectrometer at 0°, 4° and 6°. The data analysis procedure was described in SECTION 4.1. The folding optical potential obtained with the CDM3Y5 NN interaction and with density den1 (as shown in Table 4.8) were used to analyze ^{24}Mg giant resonance data. Sample excitation energy spectra for ^{24}Mg with average center of mass angles 1.3°, 4.7° and 9.5° are shown in Fig. 4.29 with pink curves representing the continuum choices. Angular distributions of differential cross sections for the giant resonance peak and background are shown in Fig. 4.30 along with DWBA fits for three energy bins with average excitation energies 12.94 MeV, 20.08 MeV and 28.75 MeV.

The E0, E1, E2 and E3 strength distributions obtained are shown in Fig. 4.31 and Fig. 4.32 along with those obtained from two different analyses of α scattering. The

multipole parameters obtained for ^{24}Mg are summarized and compared with those from α scattering and 156 MeV ^{6}Li scattering in Table 4.13. The centroid, (m_1/m_0), rms width and percentage of the EWSR are calculated for the total excitation range measured (8 to 40 MeV), as well as for the ranges ~10 to 20 MeV.

The E0 strength for ^{24}Mg extracted in the energy range 9 to 40 MeV in this work 106^{+34}_{-24} % of the E0 EWSR, is in agreement within the errors with those obtained in α scattering 72±10% given in Ref. [39] and 82±9% given by new analysis of α scattering [50]. Dennert *et al*. [53] reported 97±25% of the E0 EWSR for the region Ex = 10 - 23 MeV obtained with 156 MeV ^{6}Li scattering. However, Youngblood *et al*. [39] pointed out that Dennert *et al*. used a non-conventional normalization of the DWBA to the angular distribution (see Fig. 3 in Ref. [53]), in which the peak of data for E0 strength is about a factor of 2 below the peak of the DWBA calculation. This resulted in the E0 strength being about a factor of 2 higher. If Dennert *et al.*'s result is divided by this factor of 2, the adjusted E0 strength in the range E_x = 10 - 20.2 MeV corresponds to 34±3% of the E0 EWSR with a centroid energy 16.66±0.5 MeV and rms width 2.48±0.5 MeV, which is in excellent agreement with the strength obtained in this work corresponding to 35±5% of the E0 EWSR with a centroid energy 16.88±0.17 MeV and rms width 2.13±0.17 MeV (see Fig. 4.33 and Table 4.13). S. Peru *et al.* [140] used the quasi-particle Random Phase approximation (QRPA) based on Hartree-Fock-Bogolyubov states (HFB) obtained with the Gogny D1S effective force [141, 142], to calculate the ISGMR strength distribution for ^{24}Mg. The results are shown in Fig. 4.34 along with the strength distribution obtained in this work. It is also interesting to see that, if the strength distribution obtained in the new analysis of α scattering data is multiplied by a factor of 1.7, it will overlap the strength obtained in this work (see Fig. 4.35) in the range E_x = 16 - 30 MeV.

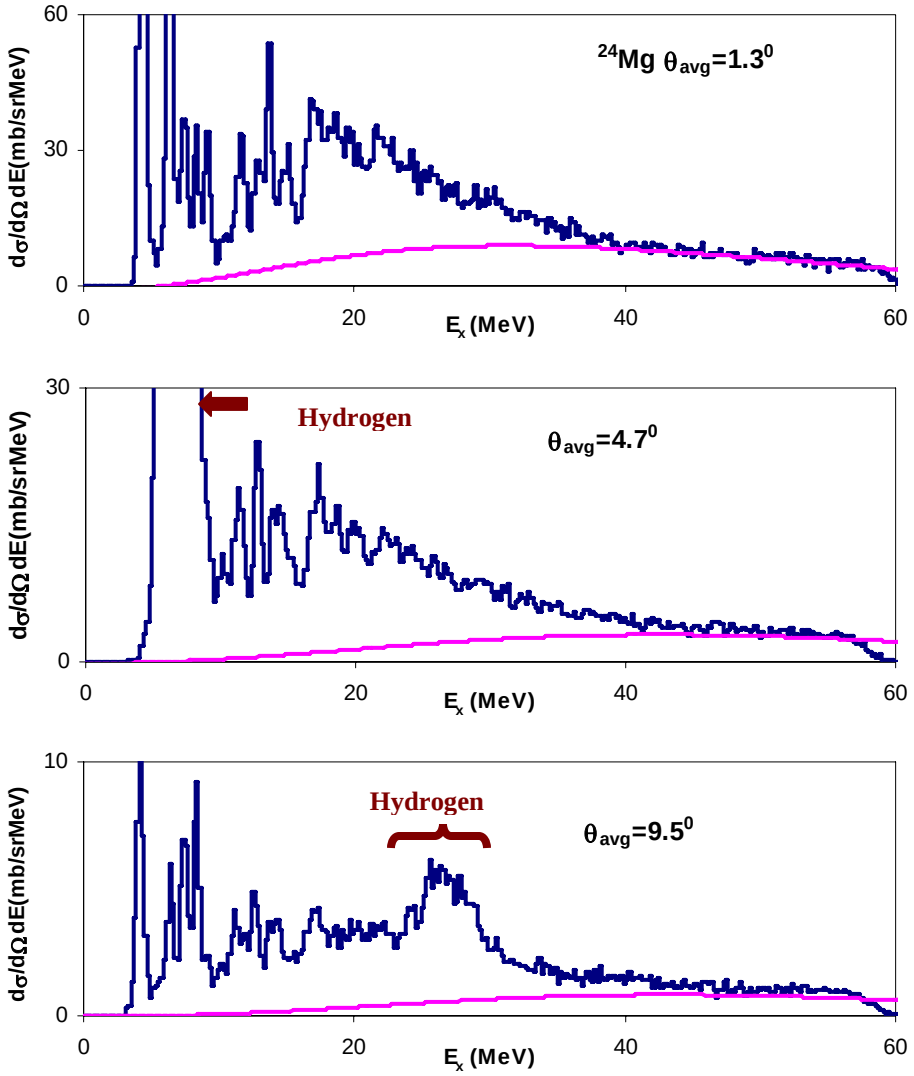

FIG. 4.29 Sample spectra for ^{24}Mg at average center of mass angle 1.3°, 4.7° and 9.5°. The pink curves are the continuum chosen for the analysis. The broad structures pointed by the brown arrow or covered by the parenthesis is contamination caused by ^{6}Li scattering on Hydrogen.

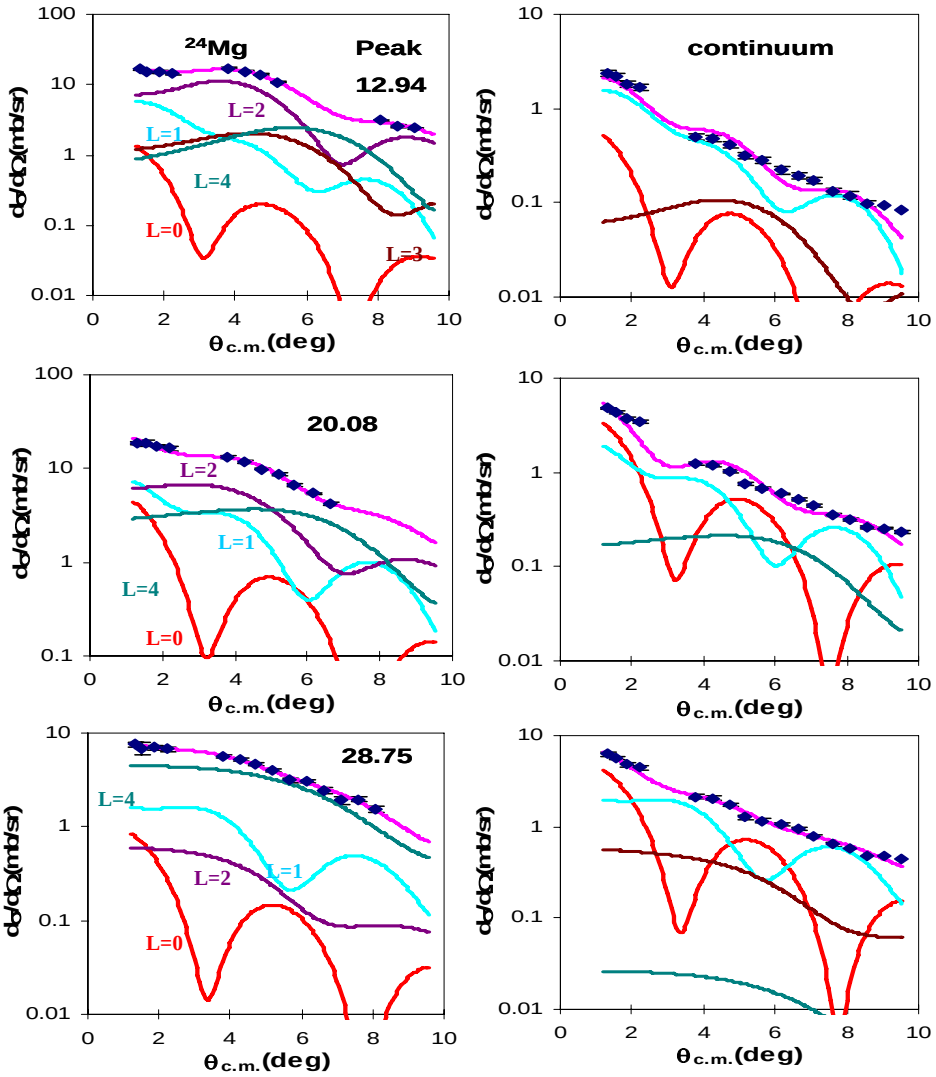

FIG. 4.30 Angular distributions of the cross section for inelastic scattering from ^{24}Mg for 0.8 MeV wide bin centered at E_x=12.94, 20.08, 28.75 MeV along with DWBA fits. The left column shows those for the giant resonance peak while the right column shows those for the continuum. The pink lines through the data show the fits. The E0 contribution is shown by the red line, the isoscalar E1 contribution by the light blue line, the E2 contributions by the purple lines, the E3 contributions by the brown lines and E4 contributions by the dark green lines.

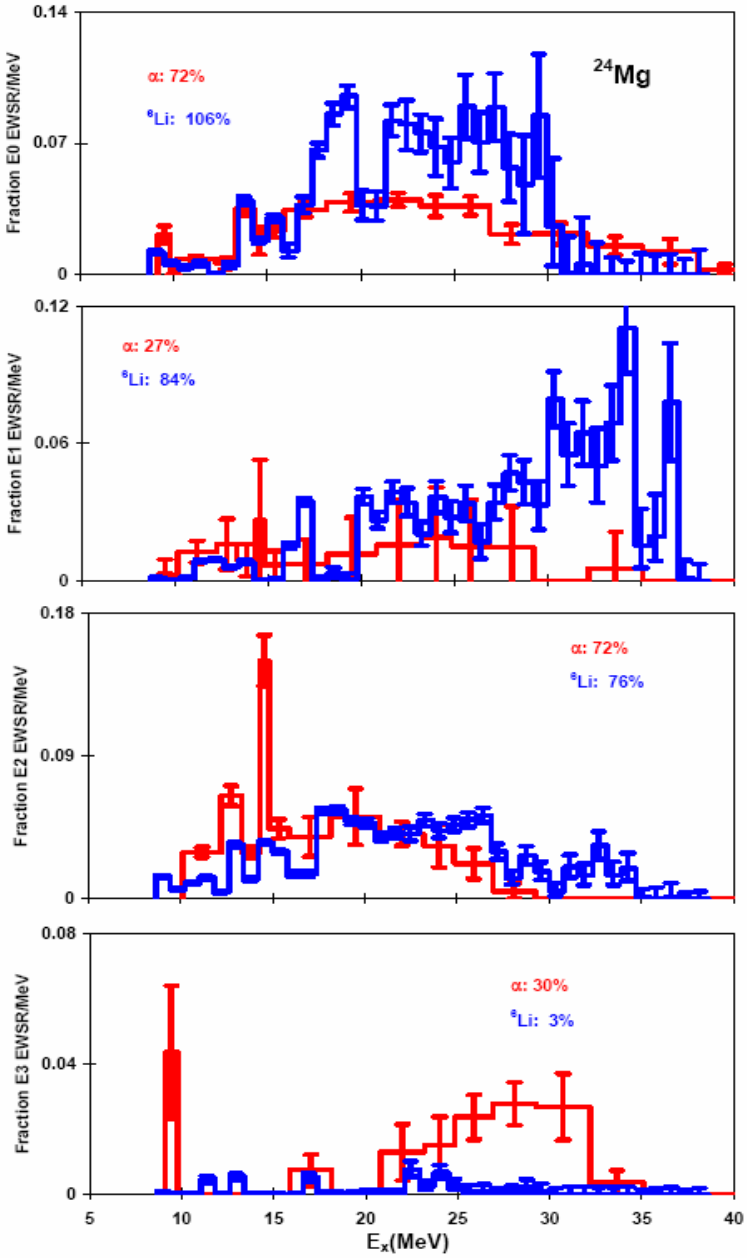

FIG 4.31 The blue curves show E0, E1, E2 and E3 strength distributions for ^{24}Mg obtained from analysis of ^{6}Li inelastic scattering. The red curves show those obtained with α inelastic scattering [39]. Error bars represent the uncertainty due to the fitting of the angular distributions and different choices of the continuum.

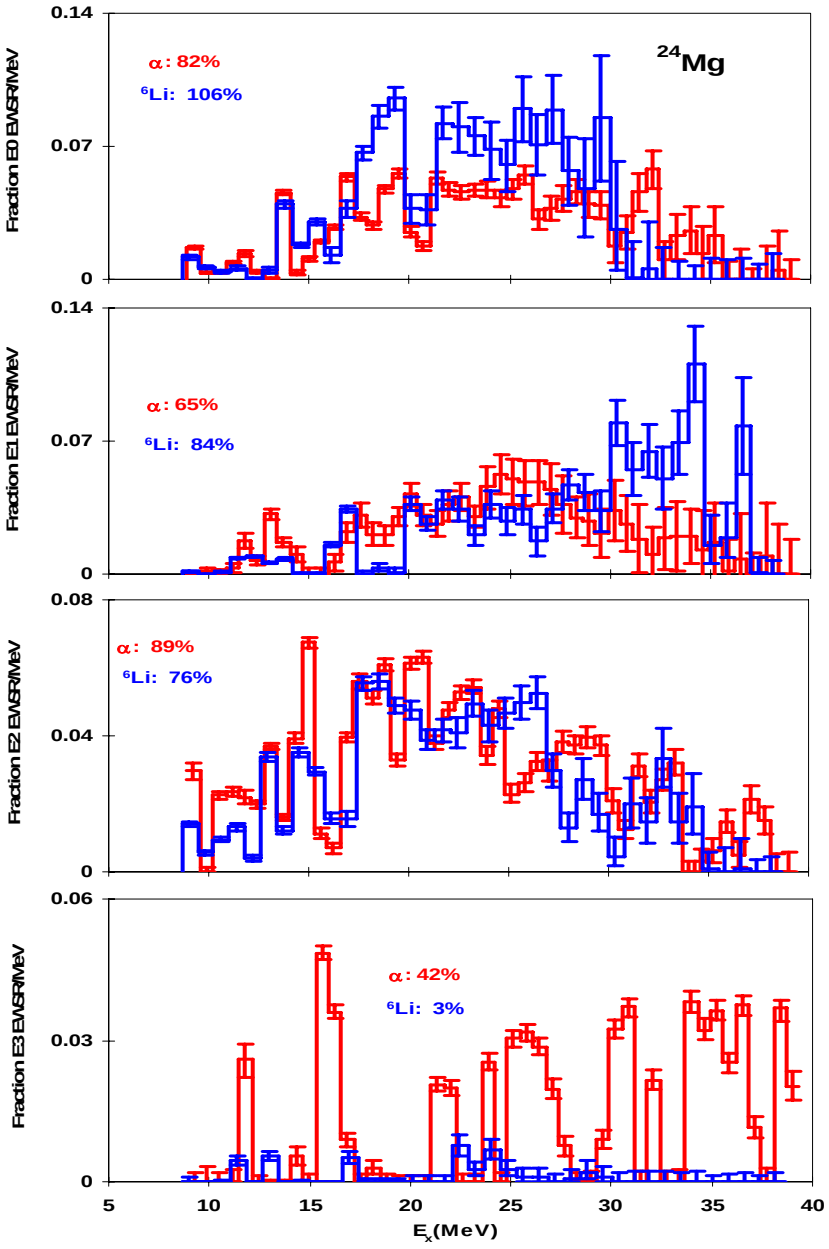

FIG. 4.32 The blue curves show E0, E1, E2 and E3 strength distributions for ^{24}Mg obtained from analysis of ^{6}Li inelastic scattering. The red curves show those obtained with new analysis of α inelastic scattering [50]. Error bars represent the uncertainty due to the fitting of the angular distributions and different choices of the continuum.

Table 4.13 Multipole parameters obtained for ^{24}Mg in this work compared to those obtained from analysis of α scattering and from previous 156 MeV ^{6}Li scattering.

	^{6}Li scattering					**α scattering**				
L	Ref.	E_x energy (MeV)	m_l/m_0 (MeV)	rms width (MeV)	EWSR (%)	Ref.	E_x range (MeV)	m_l/m_0 (MeV)	rms width (MeV)	EWSR (%)
0	This work	10.2-20.6	$16.88^{+0.17}_{-0.17}$	2.13 ± 0.17	35±5	[39]	10.1-20.9	16.31±0.6*	2.62±0.74	27±4
		8.6-38.6	$21.35^{+0.37}_{-0.26}$	$4.98^{+0.68}_{-0.32}$	106^{+34}_{-24}		9.0-41.0	21.0±0.6	7.3±1.2	72±10
	[53]	10.0-20.2	16.66±0.5	2.48±0.5	34±3	[50]	10.2-20.4	$16.44^{+0.33}_{-0.25}$	$2.48^{+0.48}_{-0.23}$	24±4
							9.0-41.0	$21.93^{+0.33}_{-0.25}$	$6.53^{+0.47}_{-0.23}$	82±9
1	This work	10.2-20.6	$14.75^{+0.20}_{-0.17}$	2.29 ± 0.17	10±3	[39]	10.1-20.9	14.68±2.21	3.14±0.97	12^{+11}_{-5}
							9.0-41.0	18.8±1.7	6.7±1.0	27^{+26}_{-11}
		8.6-38.6	$26.56^{+0.29}_{-0.26}$	$6.42^{+0.29}_{-0.27}$	84^{+24}_{-21}	[50]	10.2-20.4	$16.12^{+0.23}_{-0.20}$	$3.33^{+0.68}_{-0.49}$	16±5
							9.0-41.0	$22.70^{+0.23}_{-0.20}$	$6.19^{+0.67}_{-0.49}$	65±8
2	This work	10.2-20.6	15.79±0.17	2.58±0.17	30±4	[39]	10.1-20.9	15.07±0.6*	2.07±0.6*	51^{+5}_{-8}
							9.0-41.0	16.9±0.6	3.4±0.6	72±10
		8.6-38.6	$20.23^{+0.25}_{-0.20}$	$6.29^{+0.34}_{-0.25}$	76^{+14}_{-12}	[50]	10.2-20.4	15.56 ± 0.18	$2.93^{+0.25}_{-0.20}$	36±4
							9.0-41.0	$19.92^{+0.18}_{-0.18}$	$7.25^{+0.25}_{-0.20}$	89±9
3	This work	8.6-38.6	$18.54^{+1.40}_{-0.38}$	$5.85^{+0.28}_{-0.19}$	3^{+4}_{-1}	[39]	9.0-41.0	25.2±1.0	4.5±1.2	31^{+9}_{-6}
						[50]	9.0-41.0	$25.43^{+0.37}_{-0.23}$	$8.31^{+0.23}_{-0.22}$	42±5

*: assume the uncertainty is the same as in the total energy range

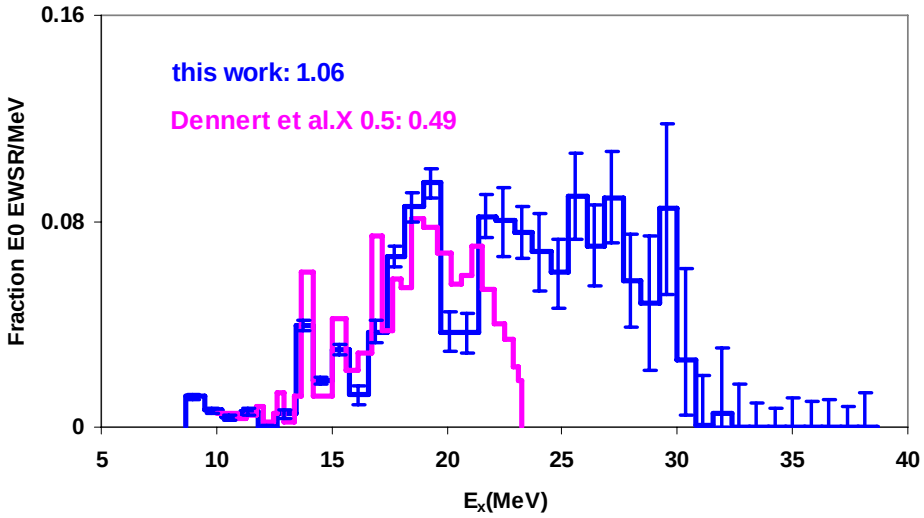

FIG. 4.33 E0 strength distribution obtained for ^{24}Mg in this work compared to that obtained from previous 156 MeV ^{6}Li scattering [53] multiplied by 0.5.

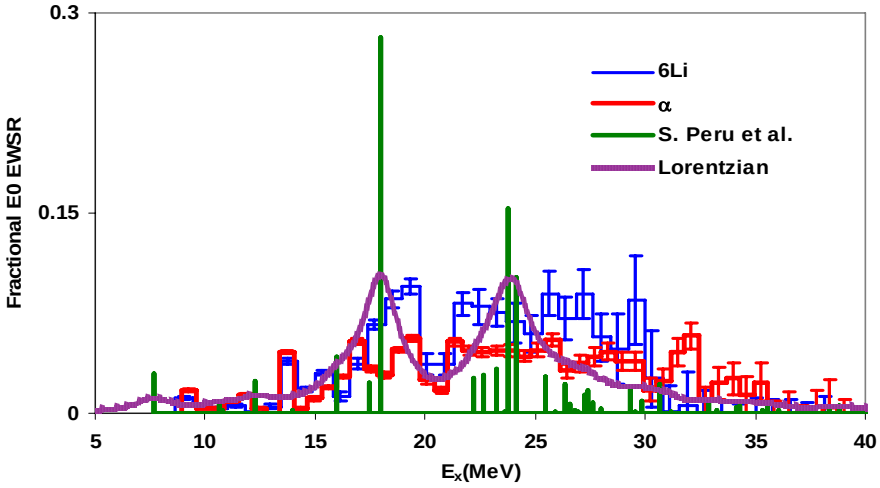

FIG. 4.34 E0 strength distribution of ^{24}Mg calculated by Peru *et al.* [140] with QRPA+HBF theory (shown as dark green line), compared to that obtained in this work (blue line) and that obtained with α scattering [50] (red line). The purple thick line represents the convolutions of calculated discrete spectra with 2 MeV width Lorentzian distributions.

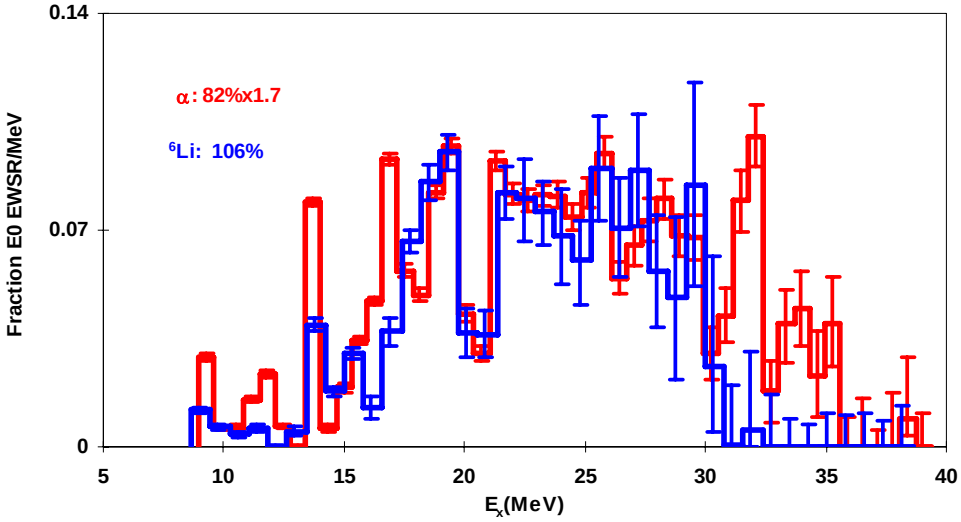

FIG. 4.35 E0 strength distribution obtained for ^{24}Mg in this work compared to that obtained from a new analysis of the α scattering data [50] multiplied with a factor of 1.7.

The E2 strength extracted for ^{24}Mg in this work corresponding to 76^{+14}_{-12} % of the E2 EWSR with a centroid energy of $20.23^{+0.25}_{-0.20}$ MeV and an rms width of $6.29^{+0.34}_{-0.25}$ MeV, is in agreement with that obtained with a new analysis of the α data which corresponds to 89±9% of the E2 EWSR with a centroid of 19.92±0.18 MeV and an rms width of $7.25^{+0.25}_{-0.20}$ MeV. The percentage of the E2 EWSR obtained also agrees with 72±10% of the E2 EWSR given in Ref. [39], however, the strength given in Ref. [39] has a lower centroid energy of 16.9±0.6 MeV and a much smaller rms width of 3.4±0.6 MeV. E2 strength in excitation range E_x = 10.2 - 20.6 MeV corresponds to 30±4% of the E2 EWSR with a centroid of 15.79±0.17 MeV and an rms width of 2.58±0.17, in agreement with that obtained in new analysis of α scattering data which corresponds to 36±4% of the E2 EWSR with a centroid of 15.56±0.17 MeV and an rms width of $2.93^{+0.25}_{-0.20}$ (see Table 4.13).

The total isoscalar E1 strength corresponds to 84^{+24}_{-21}% of the E1 EWSR, which is much higher than 27^{+26}_{-14}% given in Ref. [39] (note: the original value 81^{+26}_{-14}% in Table IV of Ref. [39] should be divided by 3 due to the transition density correction for ISGDR). In the new analysis of α scattering data, the E1 strength obtained corresponds to 65±8% of the E1 EWSR, which agrees with this work, but it has a lower centroid energy (see Table 4.13). E1 strength for excitation range $E_X = 10 - 20$ MeV corresponding to 10±3% of the E1 EWSR with a centroid energy $14.75^{+0.20}_{-0.17}$ MeV and rms width 2.29±0.17, is in agreement within error with the one given in Ref. [39] which corresponds to 12^{+11}_{-5}% of E1 EWSR with a centroid of 14.68±2.21 MeV and rms width 3.14±0.97 MeV.

E3 strength corresponding to only about 3% of the E3 EWSR was identified, compared to those observed in α scattering corresponding to 31% of the E3 EWSR given in Ref. [39] and 42% of the E3 EWSR given by the new analysis of α scattering.

5. SUMMARY, DISCUSSION AND CONCLUSIONS

Elastic and inelastic scattering of 240 MeV ^{6}Li ions from ^{116}Sn, ^{28}Si and ^{24}Mg was studied as a possible alternate tool for investigating giant resonances in nuclei. The distorted-wave Born approximation was used to calculate expected cross-sections and angular distributions using optical potentials obtained from fitting the elastic scattering data. Results obtained with Woods-Saxon phenomenological potentials and potentials obtained by folding the density distributions of the projectile and target with JLM and M3Y NN interactions were compared. It has been shown that it is necessary to use folding model calculations for hadronic scattering to get B(EL) values for low-lying excited states [118, 137] that consistently agree with those from electron scattering.

In previous giant resonance work at this laboratory using α scattering, single folding calculations had been used, so computer codes were obtained to carry out the double folding calculations and procedures had to be developed to make these calculations for ^{6}Li scattering. Optical and transition potentials were obtained by folding with the code **DFPD4** and DWBA calculations were carried out with **ECIS**. **DFPD4** was modified to calculate the transition density for monopole and isoscalar dipole giant resonances. A PYTHON code **df_ecis_avg.py** was written to control the folding calculations, DWBA calculations, angle averaging, etc.

To check consistency with previous data analyses and verify DFPD4 and ECIS operation, calculations were carried out for the 240 MeV α + ^{144}Sm scattering system (which had been previously studied [49] experimentally) using both **DOLFIN** (single folding model calculation) and **DFPD4** (double folding model calculation with M3Y-Paris NN effective interaction) to calculate potentials which were then read into **ECIS** to calculate cross sections. The results were compared to those obtained with **DOLFIN** and **PTOLEMY**. About 10% difference was found for maximum differential cross section for excitations with L=2, 3, 4 and about 4% difference was found for L=0 due to differences in single folding and double folding models, difference in numerical

interpolations in folding code and difference in Coulomb potential treatments. This suggests a minimum ~10% uncertainty in experimental giant resonance strengths due to the uncertainties in the DWBA calculations.

Experimental cross sections obtained for elastic scattering of ^{6}Li ions from ^{24}Mg, ^{28}Si and ^{116}Sn were fit with cross sections calculated with the optical model using Woods-Saxon phenomenological potentials and real potentials obtained from double folding models with and without density dependence. The folded potentials had to be renormalized by a substantial factor N_r (N_r~0.65 for ^{116}Sn ,~ 0.85 for ^{28}Si and ~0.9 for ^{24}Mg) to fit the elastic scattering data, consistent with earlier ^{6}Li scattering studies[69, 120]. Best fit B(EL) values were then obtained for the low-lying 2^+ and 3^- states by fitting the experimental cross sections for inelastic excitation of these states with those calculated by DWBA. For ^{116}Sn, the B(EL) values obtained using the deformed potential model as well as from density dependent folding calculations agree well with adopted values and with those from electron inelastic scattering and α inelastic scattering. Those obtained with the density independent folding model calculations do not reproduce the electromagnetic B(EL) values, which suggests that density dependent calculations may be required. The B(EL) values obtained for low lying states in ^{24}Mg and ^{28}Si using density dependent folding calculations agreed with those obtained from electron scattering whereas those obtained using deformed potential calculations did not, consistent with Beene *et al*.'s conclusion [137].

Multipole decompositions of the data for the giant resonance region of ^{24}Mg, ^{28}Si and ^{116}Sn were carried out with calculations using the density dependent double folding model. In addition a decomposition of the ^{116}Sn data was done with calculations using the deformed potential model.

The ISGMR and ISGQR strength distributions obtained for ^{116}Sn with both calculations are in agreement with those obtained by inelastic α scattering. The ISGDR strength obtained using the deformed potential model calculations corresponded to ~500% of the

E1 EWSR whereas strength corresponding to 118^{+20}_{-14} % was obtained using double folding calculations. Only 88±20% of the ISGDR EWSR was identified in α scattering. In α scattering studies it was found that the ISGDR cross section obtained with the deformed potential model was extremely sensitive to optical model parameters [130] and this suggests it is true in ^{6}Li scattering as well. As in the α scattering studies, the strength was split between two peaks qualitatively consistent with theoretical predictions [143-145]. The HEOR distribution obtained has about the same shape as that from α scattering, but the strength obtained (116±13%) is much greater than that obtained from α scattering and the ~75% [146] expected for the HEOR.

The E0 strength in ^{28}Si identified in this work is in good agreement with that identified with inelastic α scattering[40, 134]. The E2 strength identified below E_x = 22 MeV is in agreement with that reported in inelastic α scattering where a continuum was subtracted [40], but is smaller than that obtained when the strength in the continuum was included [134]. The E2 strength obtained in this work in the excitation range E_x ~ 22 – 40 MeV is considerably larger than that obtained in either α scattering analysis. The differences between the ^{6}Li and α scattering results (both of which within the errors identify strength corresponding to ~100% of the E2 EWSR) are an indication of the inherent uncertainties in identifying multipole strength when a significant continuum must also be accounted for. This is more apparent comparing the E1 strengths obtained from ^{6}Li (85% of the EWSR) and α scattering (15% of the EWSR). The E1 EWSR strength distribution given in Ref. [40], if multiplied by a factor of 5, overlaps nicely that obtained in this work in the range E_x ~ 15 – 30 MeV. In inelastic α scattering, it has been noted that ISGDR strength is very sensitive to assumptions about the continuum [10], as illustrated by the different distributions reported in Ref.'s [9] and [10].

In this work, strength corresponding to 106^{+24}_{-24} % of the E0 EWSR was identified in ^{24}Mg, compared to 72±10 % identified in α scattering Ref. [39, 53], however the distributions were very similar and the centroid energies are in agreement. The E0

strength obtained in this work for excitation range E_x= 10-22 MeV is in excellent agreement with the adjusted Dennert *et al*.'s result [53], but above ~ 22 MeV the E0 strength obtained by Dennert *et al*. rapidly went to 0, probably due to the lower bombarding energy (156 MeV). The E2 strength obtained in this work is in agreement with that obtained in a new analysis of the α data [50]. The E1 strength obtained is in agreement with that from α scattering below E_x~ 30 MeV, but considerably more E1 strength is seen in the ^{6}Li scattering between E_x = 30 and 40 MeV. Strength corresponding to only 3% of the E3 EWSR was identified in ^{6}Li scattering compared to 42% identified in α scattering .

It is useful to summarize the comparisons between the results from ^{6}Li scattering and those obtained from α scattering for the ISGMR, ISGDR and ISGQR respectively. Table 5.1 shows the comparisons for the ISGMR. The total strength and the centroids obtained by ^{6}Li scattering for ^{116}Sn, ^{28}Si and ^{24}Mg are all in agreement those obtained with α scattering. Table 5.2 shows the comparisons for the ISGQR. The total strengths and the centroids obtained for ^{116}Sn and ^{24}Mg are also in agreement with α scattering, while more strength is observed above E_x =22 MeV in ^{28}Si compared to α scattering.

Table 5.1 Comparisons of fractional energy weight sum rule (EWSR) and energy moments between this work and previous works for ISGMR. E_B represents bombarding energy.

	Scattering type	**E_B (MeV)**	**E_x interval (MeV)**	**$\sqrt{m_1/m_{-1}}$ (MeV)**	**m_1/m_0 (MeV)**	**$\sqrt{m_3/m_1}$ (MeV)**	**EWSR (%)**
^{24}Mg	α [39]	240	9.0-41.0		21.0±0.6		72±10
	α[50]	240	9.0-41.0	$20.83^{+0.28}_{-0.22}$	$21.93^{+0.33}_{-0.25}$	$24.65^{+0.53}_{-0.31}$	82±9
	^{6}Li[53]	156	10.0-23.16	17.6±0.5	18.3±0.5	18.6±0.5	97±15
	^{6}Li	240	8.6-38.6	$20.58^{+0.32}_{-0.25}$	$21.35^{+0.37}_{-0.26}$	$23.10^{+0.53}_{-0.30}$	106^{+34}_{-24}
^{28}Si	α[40]	240	8.0-40.0	20.13±0.38	21.25±0.38	23.7±0.70	81±10
	α [134]	240	8.0-40.0		20.89±0.38		74±7
	^{6}Li	240	8.0-40.0	$19.85^{+0.61}_{-0.29}$	$20.59^{+0.78}_{-0.33}$	$22.70^{+1.58}_{-0.35}$	80^{+35}_{-20}
^{116}Sn	α [49]	240	5.0-35.0	15.45±0.20	15.62±0.20	16.13±0.20	112±15
	^{6}Li	240	8.0-31.0	$15.17^{+0.30}_{-0.20}$	$15.39^{+0.35}_{-0.20}$	$16.12^{+0.59}_{-0.32}$	106^{+27}_{-11}

Table 5.2 Comparison of the strength and m_1/m_0 between this work and previous works for ISGQR.

	E_x range (MeV)	Scattering type	m_1/m_0 (MeV)	EWSR (%)	Ref.
^{116}Sn	~8-30	240 MeV α	14.0±0.50	103±10	[49]
		240 MeV α	13.50±0.35	108±12	[133]
		240 MeV ^{6}Li	$14.34^{+0.26}_{-0.20}$	94^{+14}_{-10}	This work
^{28}Si	~8-22	240 MeV α	16.59±0.35	47±5	[40]
		240 MeV ^{6}Li	17.25±0.17	47±5	This work
	~22-40	240 MeV α	27.21±0.25	18±2	[40]
		240 MeV ^{6}Li	$29.22^{+0.20}_{-0.19}$	64±6	This work
^{24}Mg	~10-20	240 MeV α	15.56±0.18	36±4	[50]
		240 MeV ^{6}Li	15.79±0.17	30±4	This work
	~9-40	240 MeV α	19.92±0.18	89±9	[50]
		240 MeV ^{6}Li	$20.23^{-0.25}_{-0.20}$	76^{+14}_{-12}	This work

The results obtained from ^{6}Li scattering do not agree with those obtained from α scattering for the ISGDR. We have known from previous analysis of α scattering that the ISGDR is sensitive to the potential parameters [130], and also very sensitive to the physical continuum choice [134]. The fact that ISGDR strength for ^{116}Sn, ^{28}Si and ^{24}Mg can not be reproduced well in the ^{6}Li scattering, strengthens the above conclusion. However, there are some common characteristics between the ISGDR strength obtained in ^{6}Li and α scattering, such as, the ISGDR strength for ^{116}Sn extracted in both ^{6}Li and α scattering is split into two peaks; the ISGDR strength for ^{28}Si obtained in α scattering has the same energy distribution as that extracted in ^{6}Li scattering below E_x= 30 MeV; the ISGDR strength for ^{24}Mg below E_x =25 MeV obtained with α scattering is in agreement with that extracted in ^{6}Li scattering.

As shown in Table 5.3, the predicted peak differential cross sections for E0 excitation in ^{28}Si with ^{6}Li scattering and with α scattering at E_x = 15 MeV are about the same, but the ^{6}Li cross section decreases much faster at higher excitation than does the α cross section. Also the peak cross sections for the excitation of the other multipoles is

considerably lower in α scattering than in ^{6}Li scattering, so that particularly at higher excitation, monopole strength is surpressed relative to the other multipoles in ^{6}Li scattering. Fig. 5.1 shows an excitation energy spectra obtained in ^{6}Li scattering at $\theta_{c.m.}$ = 1.3° compared to one obtained in alpha scattering at $\theta_{c.m.}$ = 1.2°. The differential cross section for ^{6}Li scattering goes below that for alpha scattering around 40 MeV, suggesting that the processes that make up the continuum are lower in ^{6}Li scattering. In the excitation energy range from 5 − 40 MeV, the continua chosen for ^{6}Li scattering (black curve) and α scattering (green curve) are more or less the same, the difference of the differential cross sections between α and ^{6}Li scattering is due to other L = 1 − 3 excitations rather than E0 excitation, which indicate that ^{6}Li scattering may not be a better way to study the ISGMR than α scattering for high excitation energy range (~30−40 MeV).

Table 5.3 The maximum differential cross section obtained with DWBA calculations for ^{28}Si with L = 0 − 3 excitation in α and ^{6}Li inelastic scattering.

	Max. dσ/dΩ in ^{6}Li inelastic scattering (mb/sr)				Max. dσ/dΩ in α inelastic scattering (mb/sr)			
E_x(MeV)	L=0	L=1	L=2	L=3	L=0	L=1	L=2	L=3
15	361	460	331	428	343	170	228	206
30	21.4	32.1	66.6	143	53.7	29.4	69.0	82.3
35	7.25	13.0	35.4	89.5	25.8	16.5	47.3	61.4
40	2.29	5.54	17.8	49.9	11.3	8.9	32.2	49.0

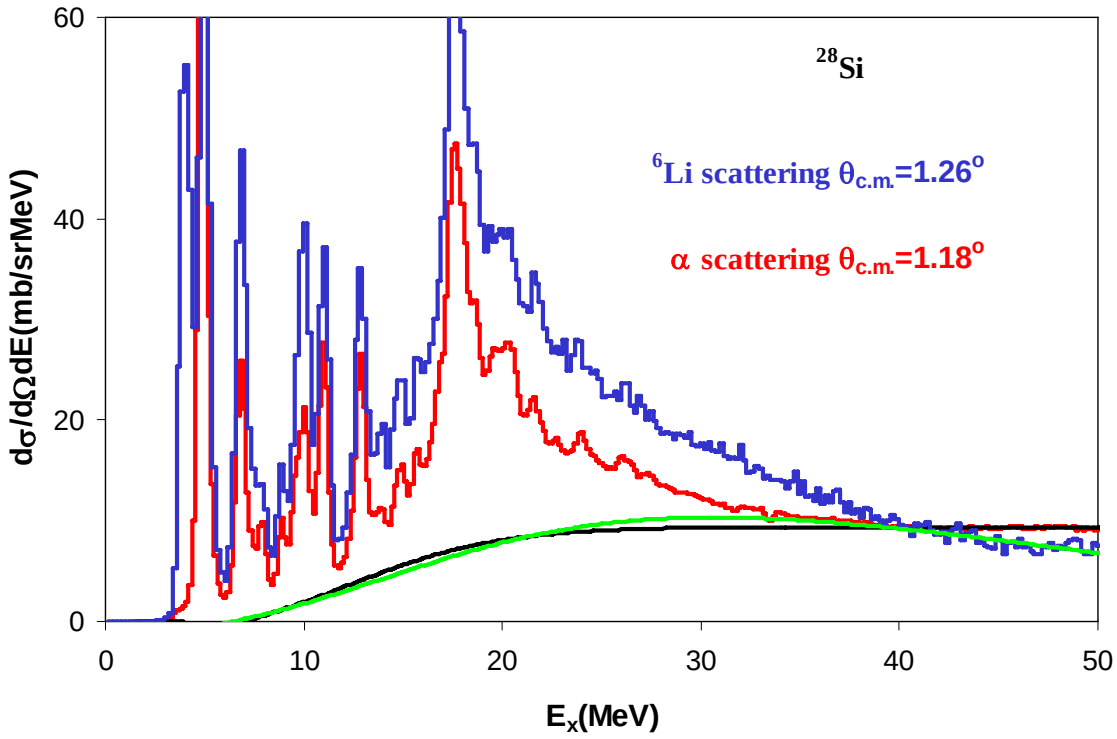

FIG. 5.1 The excitation energy spectra obtained in ^{6}Li scattering (blue curve) at $\theta_{c.m.}$ = 1.3° and in α scattering (red curve) at $\theta_{c.m.}$ = 1.2°. The black curve is the continuum for α scattering spectrum while the green one is for ^{6}Li scattering.

To summarize this research, data for elastic and inelastic scattering of 240 MeV ^{6}Li ions exciting low lying states and giant resonances was taken on ^{24}Mg, ^{28}Si, and ^{116}Sn. Parameters and techniques were developed for double folding calculations and multipole analyses were carried out for high lying isoscalar L = 0 - 3 strength. The results for the ISGMR and ISGQR are in agreement with those obtained by 240 MeV α scattering, however the agreement for the ISGDR and HEOR is not so good, indicating the uncertainty in extracting these strengths. This work has shown that 240 MeV ^{6}Li scattering is a viable way to study the ISGMR and ISGQR and can be particular useful in rare isotope studies where ^{6}Li can be used as the target.

REFERENCES

[1] S. Shlomo, Pramana J. Phys. **57**, 557 (2001).

[2] A. Bohr, and B. M. Mottleson, *Nuclear Structure II* (Benjamin, New York, 1975).

[3] N. K. Glendenning, Physical Review C **37**, 2733 (1988).

[4] D. H. Youngblood, C. M. Rozsa, J. M. Moss, D. R. Brown, and J. D. Bronson, Physical Review Letters **39**, 1188 (1977).

[5] D. H. Youngblood, H. L. Clark, and Y. W. Lui, Physical Review Letters **82**, 691 (1999).

[6] G. C. Baldwin, and G. S. Klaiber, Physical Review **71**, 3 (1947).

[7] J. Speth, in *Giant Multipole Resonance*, edited by F. E. Bertrand (Harwood Academic publisher, Oak Ridge, Tennessee, 1979).

[8] S. Fukuda, and Y. Torizuka, Physical Review Letters **29**, 1109 (1972).

[9] F. R. Buskirk, H. D. Graf, R. Pitthan, H. Theissen, O. Titze, and T. Walcher, Physics Letters B **42**, 194 (1972).

[10] M. B. Lewis, and F. E. Bertrand, Nucl. Phys. A **196**, 337 (1972).

[11] J. M. Moss, C. M. Rozsa, J. D. Bronson, and D. H. Youngblood, Physics Letters B **53**, 51 (1974).

[12] J. M. Moss, C. M. Rozsa, D. H. Youngblood, J. D. Bronson, and A. D. Bacher, Physical Review Letters **34**, 748 (1975).

[13] D. H. Youngblood, J. M. Moss, C. M. Rozsa, J. D. Bronson, A. D. Bacher, and D. R. Brown, Physical Review C **13**, 994 (1976).

[14] K. T. Knöpfle, G. J. Wagner, H. Breuer, M. Rogge, and C. Mayer-Böricke, Physical Review Letters **35**, 779 (1975).

[15] K. T. Knopfle, G. J. Wagner, A. Kiss, M. Rogge, C. Mayer-Boricke, and T. Bauer, Physics Letters B **64**, 263 (1976).

[16] D. H. Youngblood, P. Bogucki, J. D. Bronson, U. Garg, Y. W. Lui, and C. M. Rozsa, Physical Review C **23**, 1997 (1981).

[17] H. P. Morsch, and P. Decowski, Physics Letters B **95**, 160 (1980).

[18] S. S. Hanna, in *Proceedings of the Giant Multipole Resonance Topical Conference*, edited by F. E. Bertrand (Harwood Academic publisher, Oak Ridge, Tennessee, 1979).

[19] D. Ding, Y. Chen, and H. Zhang, *Progress in Nuclear Physics* (Shanghai Science and Technology Press, Shanghai, 1997).

[20] J. Speth, *Electric and Magnetic Giant Resonance in Nuclei* (World Scientific, 1991), Vol. 1.

[21] N. Marty, M. Morlet, A. Willis, V. Comparat, and R. Frascaria, Nucl. Phys. A **238**, 93 (1975).

[22] A. Willis, M. Morlet, N. Marty, R. Frascaria, C. Djalali, V. Comparat, and P. Kitching, Nucl. Phys. A **344**, 137 (1980).

[23] M. Buenerd, P. Martin, P. d. Saintignon, and J. M. Loiseaux, J.Phys.(Paris), Lett. **38**, L (1977).

[24] U. Garg, RIKEN Review **23**, 65 (1999).

[25] G. Bertsch, Suppl. Prog. Theor, Phys. **74** (1983).

[26] S. Stringari, Physics Letters B **108**, 232 (1982).

[27] J. M. Pearson, Physics Letters B **271**, 12 (1991).

[28] J. P. Blaizot, J. F. Berger, J. Decharge, and M. Girod, Nucl. Phys. A **591**, 435 (1995).

[29] S. Shlomo, and D. H. Youngblood, Physical Review C **47**, 529 (1993).

[30] S. Shlomo, and G. Bertsch, Nucl. Phys. A **243**, 507 (1975).

[31] K. F. Liu, and N. Van Giai, Physics Letters B **65**, 23 (1976).

[32] I. Hamamoto, H. Sagawa, and X. Z. Zhang, Physical Review C **56**, 3121 (1997).

[33] S. Shlomo, and A. I. Sanzhur, Physical Review C **65**, 044310 (2002).

[34] S. Shlomo, V. Kolomietz, and G. Colò, The European Physical Journal A - Hadrons and Nuclei **30** (2006).

[35] Z.-y. Ma, N. Van Giai, A. Wandelt, D. Vretenar, and P. Ring, Nucl. Phys. A **686**, 173 (2001).

[36] J. Piekarewicz, Physical Review C **66**, 034305 (2002).

[37] S. Shlomo, B. K. Agrawal, and A. V. Kim, Nucl. Phys. A **734**, 589 (2004).

[38] B. K. Agrawal, S. Shlomo, and V. Kim Au, Physical Review C **68**, 031304 (2003).

[39] D. H. Youngblood, Y. W. Lui, and H. L. Clark, Physical Review C **60**, 014304 (1999).

[40] D. H. Youngblood, Y. W. Lui, and H. L. Clark, Physical Review C **65**, 034302 (2002).

[41] B. John, Y. Tokimoto, Y. W. Lui, H. L. Clark, X. Chen, and D. H. Youngblood, Physical Review C **68**, 014305 (2003).

[42] Y. W. Lui, H. L. Clark, and D. H. Youngblood, Physical Review C **64**, 064308 (2001).

[43] D. H. Youngblood, Y. W. Lui, H. L. Clark, Y. Tokimoto, and B. John, Physical Review C **68**, 057303 (2003).

[44] Y. Tokimoto, Y. W. Lui, H. L. Clark, B. John, X. Chen, and D. H. Youngblood, Physical Review C (Nuclear Physics) **74**, 044308 (2006).

[45] Y. W. Lui, D. H. Youngblood, H. L. Clark, Y. Tokimoto, and B. John, Physical Review C (Nuclear Physics) **73**, 014314 (2006).

[46] D. H. Youngblood, Y. W. Lui, B. John, Y. Tokimoto, H. L. Clark, and X. Chen, Physical Review C (Nuclear Physics) **69**, 054312 (2004).

[47] Y. W. Lui, D. H. Youngblood, Y. Tokimoto, H. L. Clark, and B. John, Physical Review C **69**, 034611 (2004).

[48] Y. W. Lui, D. H. Youngblood, Y. Tokimoto, H. L. Clark, and B. John, Physical Review C (Nuclear Physics) **70**, 014307 (2004).

[49] D. H. Youngblood, Y. W. Lui, H. L. Clark, B. John, Y. Tokimoto, and X. Chen, Physical Review C (Nuclear Physics) **69**, 034315 (2004).

[50] D. H. Youngblood, private communication (2007).

[51] D. H. Youngblood, Private communication (2007).

[52] W. Eyrich, A. Hofmann, A. Lehmann, B. Mühldorfer, H. Schlösser, H. Wirth, H. J. Gils, H. Rebel, and S. Zagromski, Physical Review C **36**, 416 (1987).

[53] H. Dennert, E. Aschenauer, W. Eyrich, A. Lehmann, M. Moosburger, N. Scholz, H. Wirth, H. J. Gils, H. Rebel, and S. Zagromski, Physical Review C **52**, 3195 (1995).

[54] G. R. Satchler, *Direct Nuclear Reactions* (Oxford University Press, Oxford, 1983).

[55] H. Uberall, *Electron Scattering from Complex Nuclei* (Academic Press, New York, 1971).

[56] A. M. Lane, *Nuclear Theory* (Benjamin, New York, 1964).

[57] G. R. Satchler, Nucl. Phys. A **195**, 1 (1972).

[58] T. J. Deal, Nucl. Phys. A **217**, 210 (1973).

[59] M. N. Harakeh, and A. E. L. Dieperink, Physical Review C **23**, 2329 (1981).

[60] A. Bohr, Physica **22**, 959 (1956).

[61] B. L. Cohen, and A. G. Rubin, Physical Review **111**, 1568 (1958).

[62] A. M. Messiah, *Quantum Mechanics I and II* (North-Holland, Amsterdam, 1962).

[63] N. F. Mott, and H. J. W. Massey, *The Theory of Atomic Collisions* (Clarendon Press, Oxford, 1965).

[64] P. E. Hodgson, *The Optical Model of Elastic Scattering* (Oxford University Press, Oxford, 1963).

[65] I. Ulehla, L. Gomolcak, and Z. Pluhar, *Optical Model of the Atomic Nucleus* (Academic Press, New York, 1964).

[66] R. D. Woods, and D. S. Saxon, Physical Review **95**, 577 (1954).

[67] M. E. Brandan, and G. R. Satchler, Physics Reports **285**, 143 (1997).

[68] H. Feshbach, *Theoretical Nuclear Physics* (Wiley, New York, 1992).

[69] G. R. Satchler, and W. G. Love, Physics Reports **55**, 183 (1979).

[70] Y. Sakuragi, Physical Review C **35**, 2161 (1987).

[71] R. Reid, Annals of Physics **50** (1968).

[72] M. Lacombe, B. Loiseau, J. M. Richard, R. V. Mau, J. Côté, P. Pirès, and R. de Tourreil, Physical Review C **21**, 861 (1980).

[73] G. Bertsch, J. Borysowicz, H. McManus, and W. G. Love, Nucl. Phys. A **284**, 399 (1977).

[74] N. Anantaraman, H. Toki, and G. F. Bertsch, Nucl. Phys. A **398**, 269 (1983).

[75] W. G. Love, and L. W. Owen, Nucl. Phys. A **239**, 74 (1975).

[76] D. T. Khoa, and W. von Oertzen, Physics Letters B **304**, 8 (1993).

[77] D. T. Khoa, G. R. Satchler, and W. von Oertzen, Physical Review C **56**, 954 (1997).

[78] D. T. Khoa, and G. R. Satchler, Nucl. Phys. A **668**, 3 (2000).

[79] A. M. Kobos, B. A. Brown, R. Lindsay, and G. R. Satchler, Nucl. Phys. A **425**, 205 (1984).

[80] A. M. Kobos, B. A. Brown, P. E. Hodgson, G. R. Satchler, and A. Budzanowski, Nucl. Phys. A **384**, 65 (1982).

[81] D. T. Khoa, and W. von Oertzen, Physics Letters B **342**, 6 (1995).

[82] B. Sinha, Physics Reports **20**, 1 (1975).

[83] X. Campi, and A. Bouyssy, Physics Letters B **73**, 263 (1978).

[84] J. P. Jeukenne, A. Lejeune, and C. Mahaux, Physical Review C **16**, 80 (1977).

[85] L. Trache, A. Azhari, H. L. Clark, C. A. Gagliardi, Y. W. Lui, A. M. Mukhamedzhanov, R. E. Tribble, and F. Carstoiu, Physical Review C **61**, 024612 (2000).

[86] E. Bauge, J. P. Delaroche, and M. Girod, Physical Review C **58**, 1118 (1998).

[87] R. H. Bassel, G. R. Satchler, R. M. Drisko, and E. Rost, Physical Review **128**, 2693 (1962).

[88] G. R. Satchler, Nucl. Phys. A **472**, 215 (1987).

[89] G. R. Satchler, Particles and Nuclei **5** (1973).

[90] M. E.-A. Farid, and G. R. Satchler, Nucl. Phys. A **481**, 542 (1988).

[91] M. H. Macfarlane, and S. C. Pieper, in *Argonne National Laboratory Report* (Argonne National Laboratory, Argonne, 1978).

[92] L. D. Rickertsen, unpublished (1976).

[93] D. T. Khoa, unpublished (2000).

[94] F. Carstoiu, unpublished (1998).

[95] F. Carstoiu, unpublished.

[96] J. Raynal, unpublished.

[97] J. Raynal, in Proceedings of the Workshop on Applied Nuclear Theory and Nuclear Model Calculations for Nuclear Technology Application, Trieste, Italy, 1988).

[98] J. E. Poling, E. Norbeck, and R. R. Carlson, Physical Review C **13**, 648 (1976).

[99] F. Carstoiu, and R. J. Lombard, Annals of Physics **217** (1992).

[100] M. Beiner, and R. J. Lombard, Annals of Physics **86**, 262 (1974).

[101] D. T. Khoa, Private communication (2006).

[102] D. H. Youngblood, and J. D. Bronson, Nuclear Instruments and Methods in Physics Research Section A: Accelerators, Spectrometers, Detectors and Associated Equipment **361**, 37 (1995).

[103] D. M. Pringle, W. N. Catford, J. S. Winfield, D. G. Lewis, N. A. Jelley, K. W. Allen, and J. H. Coupland, Nuclear Instruments and Methods in Physics Research Section A: Accelerators, Spectrometers, Detectors and Associated Equipment **245**, 230 (1986).

[104] J. S. Winfield, D. M. Pringle, W. N. Catford, D. G. Lewis, N. A. Jelley, and K. W. Allen, Nuclear Instruments and Methods in Physics Research Section A: Accelerators, Spectrometers, Detectors and Associated Equipment **251**, 297 (1986).

[105] D. H. Youngblood, Y. W. Lui, H. L. Clark, P. Oliver, and G. Simler, Nuclear Instruments and Methods in Physics Research Section A: Accelerators, Spectrometers, Detectors and Associated Equipment **361**, 539 (1995).

[106] O. Bunemann, T. E. Cranshaw, and J. A. Harvey, Canadian Journal of Research **27, sec. A** (1949).

[107] O. R. Frisch, British Atom Energy Project (1949).

[108] H. L. Clark, unpublished.

[109] G. Charpak, and F. Sauli, Nuclear Instruments and Methods **162**, 405.

[110] D. Shapira, R. M. Devries, H. W. Fulbright, J. Toke, and M. R. Clover, Nuclear Instruments and Methods **129**, 123 (1975).

[111] J. R. Erskine, T. H. Braid, and J. C. Stoltzfus, Nuclear Instruments and Methods **135**, 67 (1976).

[112] A. Oed, P. Geltenbort, F. Gonnenwein, T. Manning, and D. Souque, Nuclear Instruments and Methods in Physics Research **205**, 455 (1983).

[113] H. L. Clark, unpublished.

[114] S. Kowalski, and H. A. Enge, unpublished.

[115] K. Van Der Borg, M. N. Harakeh, and A. Van Der Woude, Nucl. Phys. A **365**, 243 (1981).

[116] F. Ajzenberg-Selove, Nucl. Phys. A **506**, 1 (1990).

[117] D. H. Youngblood, Nucl. Phys. A **687**, 1 (2001).

[118] G. R. Satchler, and D. T. Khoa, Physical Review C **55**, 285 (1997).

[119] A. A. Korsheninnikov, E. Y. Nikolskii, C. A. Bertulani, S. Fukuda, T. Kobayashi, E. A. Kuzmin, S. Momota, B. G. Novatskii, A. A. Ogloblin, A. Ozawa, V. Pribora, I. Tanihata, and K. Yoshida, Nucl. Phys. A **617**, 45 (1997).

[120] M. El-Azab Farid, and M. A. Hassanain, Nucl. Phys. A **678**, 39 (2000).

[121] G. R. Satchler, Nucl. Phys. A **579**, 241 (1994).

[122] S. K. Gupta, and K. H. N. Murthy, Zeitschrift für Physik A Hadrons and Nuclei **307**, 187 (1982).

[123] A. Nadasen, M. McMaster, M. Fingal, J. Tavormina, P. Schwandt, J. S. Winfield, M. F. Mohar, F. D. Becchetti, J. W. Jänecke, and R. E. Warner, Physical Review C **39**, 536 (1989).

[124] J. W. Lightbody, S. Penner, S. P. Fivozinsky, P. L. Hallowell, and H. Crannell, Physical Review C **14**, 952 (1976).

[125] P. Barreau, and J. B. Bellicard, Physical Review Letters **19**, 1444 (1967).

[126] H. L. Clark, Y. W. Lui, and D. H. Youngblood, Physical Review C **57**, 2887 (1998).

[127] S. Raman, C. W. Nestor, and P. Tikkanen, Atomic Data and Nuclear Data Tables **78**, 1 (2001).

[128] T. Kibedi, and R. H. Spear, Atomic Data and Nuclear Data Tables **80**, 35 (2002).

[129] D. H. Youngblood, Y. W. Lui, and H. L. Clark, Physical Review C **55**, 2811 (1997).

[130] H. L. Clark, Y. W. Lui, and D. H. Youngblood, Nucl. Phys. A **687**, 80 (2001).

[131] D. H. Youngblood, Y. W. Lui, and H. L. Clark, Physical Review C **63**, 067301 (2001).

[132] S. S. Dietrich, and B. L. Berman, Atomic Data and Nuclear Data Tables **38**, 199 (1988).

[133] H. L. Clark, Y. W. Lui, and D. H. Youngblood, Physical Review C **63**, 031301 (2001).

[134] D. H. Youngblood, Y. W. Lui, and H. L. Clark, Physical Review C (Nuclear Physics) **76**, 027304 (2007).

[135] F. Carstoiu, L. Trache, R. E. Tribble, and C. A. Gagliardi, Physical Review C (Nuclear Physics) **70**, 054610 (2004).

[136] S. Yen, R. J. Sobie, T. E. Drake, H. Zarek, C. F. Williamson, S. Kowalski, and C. P. Sargent, Physical Review C **27**, 1939 (1983).

[137] J. R. Beene, D. J. Horen, and G. R. Satchler, Physical Review C **48**, 3128 (1993).

[138] S. W. Brain, A. Johnston, W. A. Gillespie, E. W. Lees, and R. P. Singhal, Journal of Physics G: Nuclear Physics **3**, 821 (1977).

[139] A. Johnston, and T. E. Drake, Journal of Physics A: Mathematical, Nuclear and General **7**, 898 (1974).

[140] S. Peru, H. Goutte, and J. F. Berger, Nucl. Phys. A **788**, 44 (2007).

[141] J. Dechargé, and D. Gogny, Physical Review C **21**, 1568 (1980).

[142] J. F. Berger, M. Girod, and D. Gogny, Computer Physics Communications **63**, 365 (1991).

[143] A. Kolomiets, O. Pochivalov, and S. Shlomo, in *Progress in research 1998-1999* (Cyclotron Institute, Texas A&M University, 1999).

[144] G. Colo, N. Van Giai, P. F. Bortignon, and M. R. Quaglia, Physics Letters B **485**, 362 (2000).

[145] D. Vretenar, A. Wandelt, and P. Ring, Physics Letters B **487**, 334 (2000).

[146] J. M. Moss, D. H. Youngblood, C. M. Rozsa, D. R. Brown, and J. D. Bronson, Physical Review Letters **37**, 816 (1976).

VITA

Name: Xinfeng Chen

Address: Cyclotron Institute, Texas A&M University

College Station, Texas 77843-3366

Email address: chenxinfeng@hotmail.com, xfchen@neo.tamu.edu

Education:

Ph.D., Physics, May 2008, at Texas A&M University.

Title of dissertation: Giant resonance study by ^{6}Li scattering

M.S., Physics, May 1995, at Institute of Modern Physics, CAS, China

Title of thesis: Nuclear lifetime measurement with RDDS method

B. S., Physics, Jun. 1992, at Tianjin University, China

Scientific research and teaching experience:

Research Assistant at Physics Dept, TAMU, May. 2001—Present

Measured ^{6}Li elastic and inelastic scattering from ^{116}Sn, ^{28}Si and ^{24}Mg and did data analysis with Fortran, Python and VB

Maintained wire detectors, ionization chamber and plastic scintillator detector

Lecturer at Physics Dept., Qindao University, Aug. 1995—Dec. 2000

Taught General Physics for undergraduate non-physics majors

Taught Classical Mechanics for undergraduate physics majors

Taught Fortran for undergraduates physics majors

Graduate student at Institute of Modern Physics, Sept. 1992--Jun. 1995

Used recoil distance Doppler shift (RDDS) method to measure the lifetime of nuclear energy levels.

Designed the plunger—the apparatus for lifetime measurement with RDDS method.